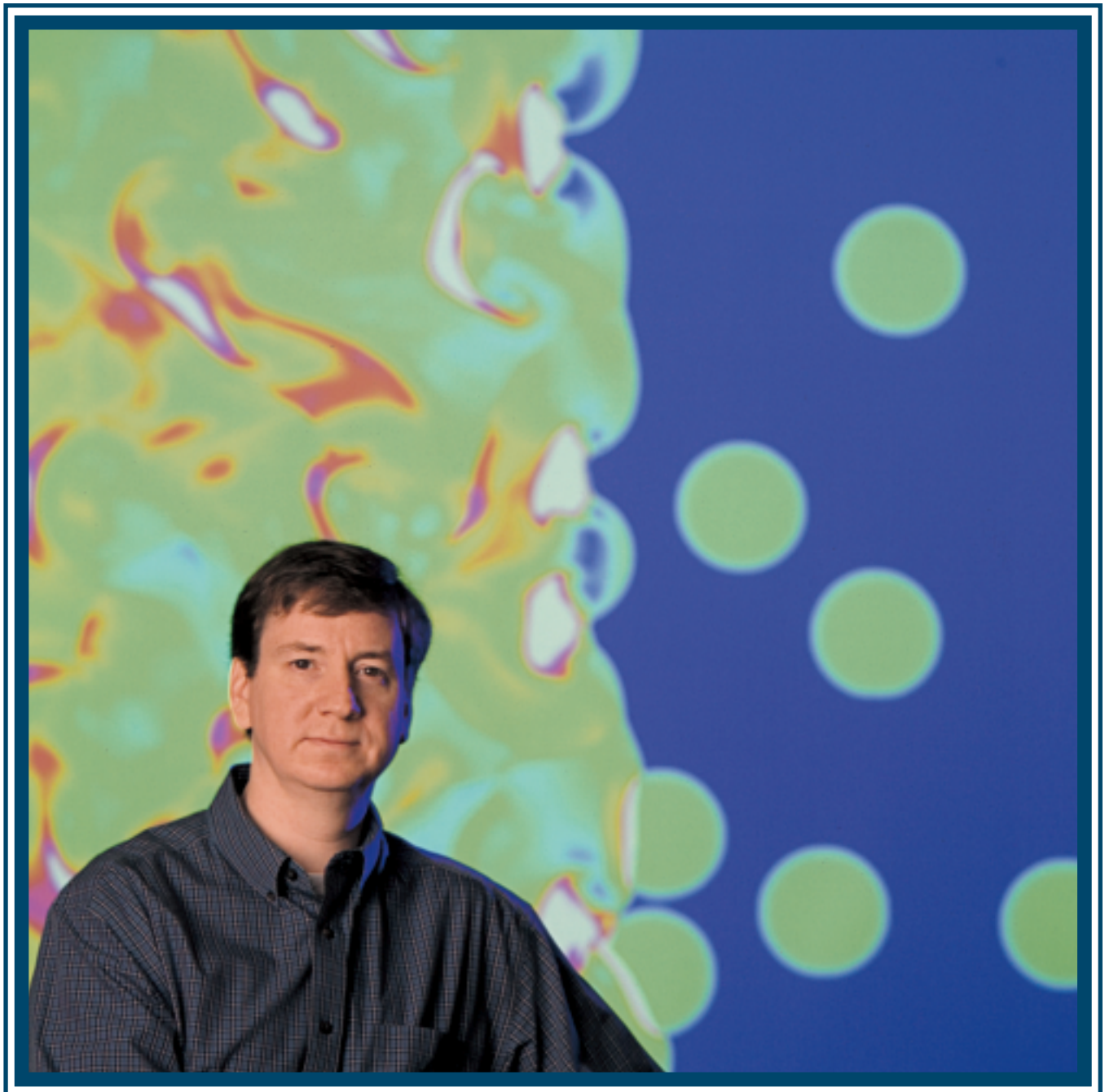


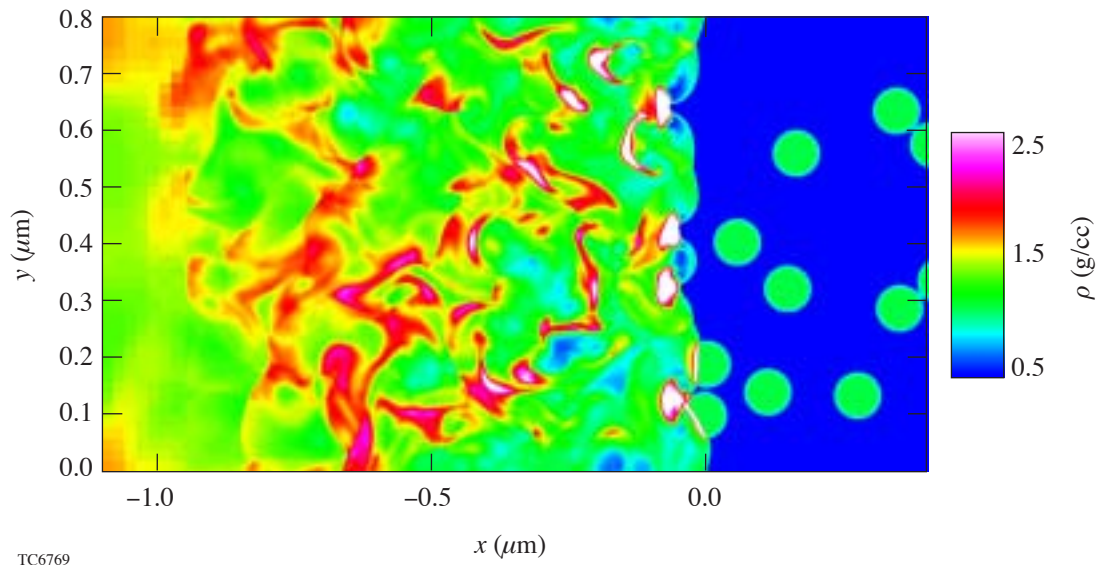
LLE Review

Quarterly Report



About the Cover:

Scientist Tim Collins is the lead author in a simulation of shock-driven mixing in a deuterium–tritium saturated fibrous foam. In the image below, the unshocked fibers and DT are seen on the right, while the shock proceeds from the left. Several microns after the shock front, the sharp density distinctions between fibers and DT are seen to become homogenized through effective mixing. Full-scale simulations of wetted-foam ICF target implosions may thus treat the foam layer as a homogeneous medium.



This report was prepared as an account of work conducted by the Laboratory for Laser Energetics and sponsored by New York State Energy Research and Development Authority, the University of Rochester, the U.S. Department of Energy, and other agencies. Neither the above named sponsors, nor any of their employees, makes any warranty, expressed or implied, or assumes any legal liability or responsibility for the accuracy, completeness, or usefulness of any information, apparatus, product, or process disclosed, or represents that its use would not infringe privately owned rights. Reference herein to any specific commercial product, process, or service by trade name, mark, manufacturer, or otherwise, does not necessarily constitute or imply its endorsement, recommendation, or favoring

by the United States Government or any agency thereof or any other sponsor. Results reported in the LLE Review should not be taken as necessarily final results as they represent active research. The views and opinions of authors expressed herein do not necessarily state or reflect those of any of the above sponsoring entities.

The work described in this volume includes current research at the Laboratory for Laser Energetics, which is supported by New York State Energy Research and Development Authority, the University of Rochester, the U.S. Department of Energy Office of Inertial Confinement Fusion under Cooperative Agreement No. DE-FC03-92SF19460, and other agencies.

Printed in the United States of America
Available from
National Technical Information Services
U.S. Department of Commerce
5285 Port Royal Road
Springfield, VA 22161

Price codes: Printed Copy A05
Microfiche A01

For questions or comments, contact Ansgar W. Schmid,
Editor, Laboratory for Laser Energetics, 250 East River Road,
Rochester, NY 14623-1299, (585) 275-3541.

Worldwide-Web Home Page: <http://www.lle.rochester.edu/>

In Brief

The key article in this volume of the LLE Review, covering July–September 2004, addresses “Shock Propagation in Deuterium–Tritium–Saturated Foam” by T. J. B. Collins (LLE) and A. Poludnenko, A. Cunningham, and A. Frank (UR, Department of Physics and Astronomy) (p. 227). Testing the assumption of homogeneous mixing in fibrous foams saturated with cryogenic deuterium and tritium, shock passage in wetted-foam mixtures was simulated by the adaptive-mesh, two-dimensional hydrodynamic code *AstroBEAR*. For foam fibers of diameter $\sim 1/10 \mu\text{m}$ and relevant foam densities, the mixing length behind the shock is found to be of the order of microns. Transverse motion dampens out sufficiently that, at the mixing region’s edge farthest from the shock, Rankine–Hugoniot jump conditions are obeyed to within a few percent and shock speeds are also within a few percent of their homogeneous values. In addition, questions of feedthrough and feedout are addressed, showing that the stability of the shock front, once it leaves the wetted-foam layer, minimizes the effect of feedthrough. As a result, simulations of whole-foam-pellet implosions may model the wetted foam as a homogeneous mixture.

Additional highlights of recent research presented in this issue include the following:

- J. Bunkenburg, T. J. Kessler, L. Iwan, C. Kellogg, and W. Skulski provide an update on the OMEGA EP tiled-grating-compressor technology (p. 242). For the first time, real-time, computer-controlled phasing of a grating triplet, using interferometric feedback via nanopositioners, has been demonstrated and a transform-limited far-field spot achieved.
- R. Forties and F. J. Marshall offer a method for accurately measuring beam position, shape, and relative intensity of the OMEGA system’s 60 beams from CID-recorded, focal-spot x-ray images from 4-mm, Au-coated pointing targets (p. 252). This method provides pivotal input into efforts to improve target-illumination uniformity by improving beam pointing and reducing variations in beam intensities from average.
- A. E. Marino, K. E. Spencer, J. E. DeGroote, K. L. Marshall, A. L. Rigatti, and S. D. Jacobs report on water-sensitive phosphate laser glass’s chemical durability in response to different polishing and cleaning conditions (p. 257). Among their many findings stands out the absence of an unambiguous correlation between initial finished surface quality of any glass type tested and quantifiable magnitude of humidity-driven degradation, whereas subsequent aqueous cleaning does increase haze: more so for pitch and pad-finished surfaces than for MRF-processed ones.
- N. Anderson, A. Hartschuh, and L. Novotny analyze single-walled carbon nanotubes at a spatial resolution of 10 to 20 nm by employing near-field Raman imaging and spectroscopy (p. 269). For individual, isolated carbon nanotubes, they find a nonuniform distribution of Raman bands along the tube axis.

LLE Review



Quarterly Report

Contents

In Brief	iii
Shock Propagation in Deuterium–Tritium– Saturated Foam	227
Demonstration of Real-Time, Phase-Locked Alignment of Tiled Gratings for Chirped-Pulse–Amplified Lasers	242
<i>In-Situ</i> Measurements of High-Intensity Laser Beams on OMEGA	252
Chemical Durability of Phosphate Laser Glasses Polished with Pitch, Pads, or MRF	257
Nanoscale Vibrational Analysis of Single-Walled Carbon Nanotubes	269
Polymer Cholesteric Liquid Crystal Flake Reorientation in an Alternating-Current Electric Field	274
LLE’s Summer High School Research Program	282
FY04 Laser Facility Report	284
National Laser Users’ Facility and External Users’ Programs	286
Publications and Conference Presentations	

- T. Z. Kosc, K. L. Marshall, S. D. Jacobs, and J. C. Lambropoulos describe the use of an ac stabilizing field in the controlled orientation and motion of polymer cholesteric-liquid-crystal flakes suspended in a host fluid (p. 274). With a display application in mind, the authors show that the field acts on an induced dipole moment on the flake surface due to interfacial Maxwell–Wagner polarization.
- This volume concludes with a summary of LLE’s Summer High School Research Program (p. 282), the FY04 Laser Facility Report (p. 284), and the National Laser Users’ Facility and External Users’ Programs (p. 286).

Ansgar W. Schmid
Editor

Shock Propagation in Deuterium–Tritium–Saturated Foam

Introduction

Over the past few years there has been considerable interest regarding the use of foam shells in inertial confinement fusion (ICF)¹ targets. The original proposed use of plastic foam shells was as a matrix for liquid deuterium–tritium (DT) fuel.² More recently, in the designs of Colombant *et al.*,³ foam has been proposed for use as an ablator material, in conjunction with an outer layer of a high-atomic-number material such as Pd. In these designs, the foam is preheated by radiation from the outer layer and has substantially higher ablation velocities, resulting in a more-stable outer surface. In other high-gain “wetted-foam” designs,⁴ the foam is used primarily because it has a higher atomic number than DT. This results in greater absorption and increased laser-energy coupling, which in turn allows more fuel to be used without reduction in stability, resulting in higher gain. Sophisticated target designs for inertial fusion energy (IFE) that build on these techniques and use wetted-foam layers have been designed and tested computationally (see, for instance, Ref. 5 and references therein). Foam has also been suggested to reduce laser imprint in direct-drive ICF.⁶

Direct-drive ICF target designs use a pulse that drives at least two main shocks into the target. Target performance depends in part on the timing of these shocks. The first shock propagating through a foam layer encounters an inhomogeneous medium. It is important to know whether this will have any effect on the shock speed and resulting shock timing. In addition, inhomogeneities in the foam can feed through to the shell’s inner surface,⁷ and again to the outer surface, where they may potentially contribute to seeds of hydrodynamic instability during the deceleration and acceleration phases of the implosion (respectively).

The length scale of the foam inhomogeneities is a fraction of a micron; for one of the foams discussed here, the foam is fibrous, with a fiber radius of about $1/20 \mu\text{m}$. A National Ignition Facility⁸ direct-drive target radius is much larger, at least 1.5 mm, with a shell thickness of hundreds of microns. This large range of length scales makes it prohibitive to model

foam inhomogeneities in a simulation of a target implosion. As a result, simulations of foam-target implosions must model the wetted foam as a homogeneous mixture.

To investigate the effects of foam microstructure, we have performed two-dimensional (2-D) hydrodynamic simulations of a shock propagating through a plastic foam saturated with DT ice. In these simulations, the microstructure of the foam filaments is resolved, allowing determination of its effects on shock behavior. ICF-relevant wetted-foam simulations modeling the foam microstructure have been performed previously by Phillips,⁹ Hazak *et al.*,¹⁰ Kotelnikov and Montgomery,¹¹ and Philippe *et al.*¹² Phillips considered an ICF-relevant case of a shock propagating through a random arrangement of plastic (CH) fibers filled with DT. He found that the shock-front perturbations were comparable in size to the fiber radius, and that the kinetic energy in the mixing region—the post-shock region in which the foam and DT are mixed and potentially homogenized—accounts for of the order of a few percent of the mean kinetic energy. Hazak *et al.* performed 2-D simulations of a shock propagating through a regular array of CH fibers, filled with liquid deuterium (D_2). They focused on the mix region behind the shock, deriving generalized jump conditions including fluctuations. Among other results, they found that the fluctuations result in an under-compression behind the shock, and that the jump to the under-compressed state cannot be modeled by a simple change in the ratio γ of specific heats. Kotelnikov and Montgomery also simulated a regular array of fibers, saturated with cryogenic DT. In their simulations they made use of a kinetic-theory–based computational model. Like Hazak *et al.*, they found that the inhomogeneities result in a post-shock mixing region in which energy is temporarily stored in turbulent motion. Finally, Philippe *et al.* performed simulations of DT-saturated foams using an adaptive-mesh-refinement code and allowing random fiber placement. They focused on the effects of inhomogeneities on the shock speed for a low- and high-density foam. They found that for the high-density foam, the deviation in shock speed from the homogeneous value was about 1% and less than 0.3% for the low-density foam.

This problem has also been addressed in astrophysical contexts, where the ratio of the material densities is much larger. The role of clumps in augmentation of the Rayleigh–Taylor instability in supernova remnants was studied using hydrodynamic simulations by Jun.¹³ More recently, Poludnenko *et al.*¹⁴ have simulated the interaction of a shock with a layer of circular obstructions, or clumps, determining the critical inter-clump distance required for the transition to a non-interacting regime in which the clouds are destroyed by the shock independently of one another. They also discussed mass loading as well as the effects of finite layer thicknesses for the collection of circular obstructions.

In our simulations the shock passage through a random array of CH fibers separated by DT is simulated, and the time-averaged level of fluctuations is determined as a function of distance behind the shock front for quantities of interest. We define the decay length for a quantity as the inverse of the logarithmic derivative of the quantity's perturbations [see Eq. (1)]. We will show that the decay lengths are comparable to a micron for a wide range of foam densities. For shock propagation distances characteristic of ICF targets, the average post-mixing region conditions approach those given by the Rankine–Hugoniot jump conditions. We also address questions of feedthrough and feedout, showing that the stability of the shock front once it leaves the wetted-foam layer minimizes the effect of feedthrough.

In the following sections (1) the hydrodynamic code used and the simulations that were performed are described; (2) the interaction of a shock with a single circular obstruction is discussed; (3) the results of multifiber simulations and their implications are presented; (4) the role of the pusher (i.e., the inflow boundary conditions) is discussed; and (5) our conclusions are presented.

Numerical Simulations

The code used for these simulations, *AstroBEAR*,¹⁵ is based on the adaptive-mesh-refinement (AMR) code *AMRCLAW*.¹⁶ In the AMR approach, subregions of the computational domain are provided with higher resolution according to a refinement criterion such as the magnitude of the truncation error or the local gradients of the hydrodynamic variables. Because the entire simulation region is not simulated at the highest resolution, the AMR scheme typically provides much-reduced execution times. In this implementation of AMR, the code attempts to optimally gather the refined cells into rectangular subgrids in order to minimize the overhead associated with refinement, and subsequently the hydrodynamic equations are advanced in

each grid and on every refinement level. The refinement criterion used in *AstroBEAR* is Richardson extrapolation, in which cells are flagged for refinement based on a local estimation of the integration error. *AstroBEAR* employs a fully nonlinear Riemann solver with the second-order-accurate Wave-Propagation Algorithm integration scheme of LeVeque.¹⁷ A polytropic equation of state is used with a ratio of specific heats $\gamma = 5/3$ gas. Thermal and radiative energy transport are not modeled in these simulations. We expect that in a real target implosion these mechanisms will dissipate fluctuations in the post-shock mix region. The results of our simulations will thus overestimate the size of the post-shock mix region and underestimate the fluctuation decay rate behind the shock. The effects of radiation could in principle be imitated by elevating the initial fiber pressure to model the absorption by the fibers of radiation emitted from the corona.

AstroBEAR tracks multiple materials by solving separate continuity equations for each of the materials—the fiber material and the DT—which provides a measure of the level of mixing after the shock (this is referred to as volume-fraction contouring).¹⁸ There is no interface construction at the boundary between the two materials. Instead, the mass of each material is maintained for a given cell. For instance, consider two adjacent cells, the left containing the first material at a higher pressure and the right the second material at a lower pressure. After one time step, the boundary between the two materials will have moved into the right cell, and at the end of that time step the right cell will be considered to contain a uniform mixture of both materials, with the appropriate fractions. Material interfaces experience some degree of smearing as a result. Shock-tube tests indicate that on the time scale of these simulations, the material interface is spread out over a distance approximately equal to the initial fiber radius. This method of material tracking is passive and in no way affects the hydrodynamics behind the shock, or the decay of perturbations in the mix region.

AstroBEAR solves the Euler equations, making no provision for turbulent motion. The Reynolds number is $Re = UL/\nu$, where U is a characteristic flow speed, L is a characteristic length scale, and ν is the viscosity coefficient. For a shock in wetted foam, we may take for the length scale L the fiber radius a ($\sim 1/20 \mu\text{m}$ for the foam density of interest), and for the characteristic flow speed U the post-shock flow speed u ($\sim 30 \text{ km/s}$ is a characteristic post-shock speed). Following Robey,¹⁹ we may estimate the kinetic viscosity using the model of Clerouin *et al.*²⁰ The initial shock strength and electron and ion conditions for the high-gain, direct-drive, NIF

wetted-foam design described in Ref. 4, determined by 1-D simulations using *LILAC*,²¹ give a Reynolds number of ~ 2800 . This is below the value of 7700 typically taken as the critical value for the onset of turbulence. In our simulations no artificial viscosity is used, although a similar effect is obtained by splitting the contact discontinuity according to the scheme of Robinet *et al.*²² This is done to prevent the growth of unphysical features (often referred to as “carbuncles”). Care has been taken to ensure that physical features are not damped.

As mentioned above, wetted-foam target designs, such as the one described in Ref. 4, take advantage of the higher laser absorption of plastic fiber than pure DT. In these designs a low-density plastic foam, which has a dry-foam density of ~ 140 mg/cc, is saturated with DT ice, e.g., CH(DT)₄, raising its density to 360 mg/cc. A typical direct-drive, NIF-scale target design consists of a shell of DT ice surrounded by a thin layer of plastic. In a wetted-foam design, an outer portion of the DT shell is replaced by wetted foam. The thickness of this layer is chosen so that the foam is entirely ablated by the laser pulse. In choosing the density of the foam, a balance must be struck between the increased absorption, which is greater for larger densities, and minimizing the radiative preheat of the inner-fuel layer of the DT ice, which is also greater for larger foam densities. As in many direct-drive target designs, the pulse consists of an initial intense picket, followed by a foot pulse, and then a drive pulse. The picket/foot combination launches the first shock into the shell, creating a greater adiabat in the ablator than in the inner-fuel layer. The second shock, launched by the more-intense drive pulse, is timed to meet the first shock inside the gas within the shell. The first shock is most relevant here since it is the only shock to encounter unshocked and unmixed wetted foam.

We have performed a number of simulations to investigate the effects of microstructure on shock propagation. The baseline simulation consists of an $8\text{-}\mu\text{m} \times 0.8\text{-}\mu\text{m}$ simulation region filled with a mixture of DT (with a density of 0.253 g/cc) and randomly placed polystyrene (CH) fibers (with a density of 1.044 g/cc). The foam being simulated, resorcinol formaldehyde (RF), is a fibrous foam with fiber spacing of ~ 0.1 to $0.2\ \mu\text{m}$. For RF, denser foams generally have the same average center-to-center fiber separation, but with thicker fibers. We simulate a foam that has a random array of fibers with the same average density as a rectangular array of fibers with a unit cell size of $R = 0.2\ \mu\text{m}$. This corresponds to an average nearest-neighbor distance of $d \sim 0.13\ \mu\text{m}$ (so the simulation size is $\sim 60\ d \times 6\ d$). The combination of fiber density and average density, for a given fiber spacing, determines the fiber radius:

for CH(DT)₄ the fiber radius is $a \sim 0.0428\ \mu\text{m}$. The dry-foam density ρ_{dry} and wetted-foam density ρ_{ave} are related by $\rho_{\text{ave}} = \rho_{\text{dry}} + \rho_{\text{DT}} - \rho_{\text{dry}}\rho_{\text{DT}}/\rho_{\text{CH}}$. The dry-foam density is given by $\rho_{\text{dry}} = \rho_{\text{ch}}\pi(a/R)^2$. In these simulations generally two levels of refinement, both $\times 4$ (so that a cell being refined is replaced by 16 cells in a 4×4 grid), were used in addition to the base level. The cells have an aspect ratio of unity, with a resolution at the highest level of 800 cells/ μm , and an equivalent simulation size at the highest resolution of 6400×640 . This corresponds to about 68 cells across a fiber. We find negligible differences between 34 and 136 cells per fiber radius. This convergence is supported by a resolution scan performed using *AstroBEAR* by Poludnenko *et al.* [Ref. 23; see their Fig. 3(a)], who also found only small differences between 32 and 64 cells per fiber radius.

In addition to this simulation size, we have also performed simulations with a size of $0.2\text{-}\mu\text{m}$ transverse to the shock propagation direction, but with a $16\text{-}\mu\text{m}$ -simulation region length in the direction of shock propagation, in order to extend the size of the mixed region. The upper and lower boundary conditions in these simulations are periodic, so the central difference between these simulations is that in the thinner one the lateral distance between the fibers is always $0.2\ \mu\text{m}$.

If we take the ablation-driven shock to travel to the right, then the right simulation boundary condition is outflow, or zero-order extrapolation, and the left is inflow. The inflow conditions are given by the Rankine–Hugoniot conditions for the average pre-shock density and pressure and for a post-shock pressure of 8 Mbar. We refer to this as an “impedance-matched” boundary condition [other inflow boundary conditions are discussed in the **Results for Different Pushers** section (p. 237)]. The CH and DT are initially in pressure equilibrium with a pressure of 0.01 Mbar. The flow, being governed by the Euler equations, is independent of Mach number when in the strong-shock limit,²⁴ so that the results are not sensitive to the initial pressure.

The Interaction of a Shock with a Single Fiber

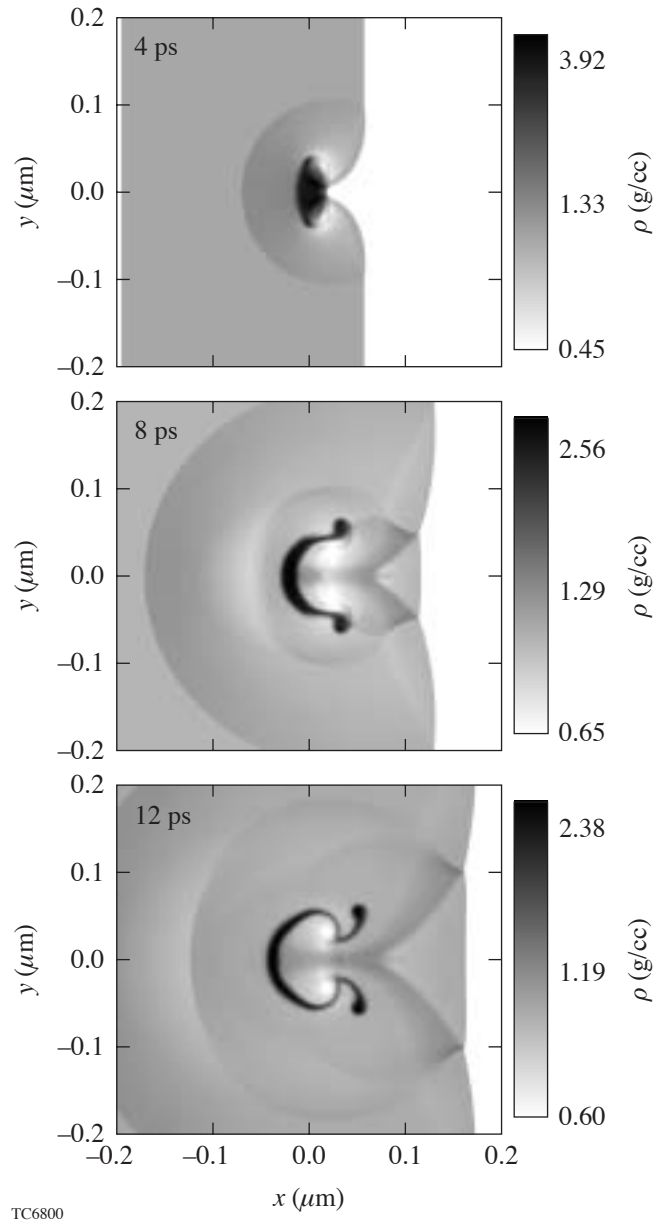
The interaction of a shock with a single fiber (or circular obstruction) has been studied extensively as a hydrodynamic problem.^{25,26} Additional physical elaborations have also been modeled, such as partial ionization²⁷ and magnetized obstructions (see, e.g., Ref. 28). Following Klein *et al.*,²⁴ the interaction of a shock with a fiber may be broken down into several distinct phases. If the flow were one-dimensional, a “forward” shock would propagate through the fiber, compressing and impulsively accelerating it, while a “reverse” bow shock would

be reflected back into the DT. Once the forward shock had crossed the fiber, a rarefaction wave would be sent back across the fiber, followed by a continuous period of acceleration that would continue until the fiber speed equaled that of the surrounding shocked DT.

Because the flow is two-dimensional, the fiber experiences several shocks: In addition to the main forward shock, other shocks are driven into the fiber from the sides as the shock in the DT moves around and past the fiber. Similarly, many rarefaction waves (RW's) are launched as each of these shocks breaks out of the fiber. These additional rarefaction waves result in expansion during this phase, both in the direction of and perpendicular to the direction of shock propagation. Finally, following the passage of these RW's, the fiber begins to accelerate. During this phase, the fiber is accelerated to the speed of the ambient (DT) fluid flow.

As described in Ref. 25, the passage of the shock generates, for a cylindrical fiber, two vortex lines behind the obstruction, and for a spherical obstruction a vortex ring is generated. These vortices and the vorticity generated by the shear flow as the fiber is accelerated mix the fiber and interfiber material. For a cylindrical obstruction and a normal shock (whose velocity vector is normal to its surface), the vortex lines are of equal magnitude and oppositely directed, so the total vorticity remains zero. If the shock is oblique, the symmetry is broken and net vorticity may be generated.

The fiber is subject to the Richtmyer–Meshkov instability as the shock first passes. As the fiber is accelerated to the speed of the post-shock DT, it is also subject to the Rayleigh–Taylor (RT) instability and, due to the shear at the fiber boundaries, the Kelvin–Helmholtz (KH) instability. In the case of a CH fiber and DT ambient fluid, the density ratio is $1.044 \text{ g cc}^{-1}/0.253 \text{ g cc}^{-1} \sim 4$. Both the RT and KH instabilities are more effective at mixing the fiber and ambient material when the ratio of fiber to ambient density is greater. Figure 100.1 shows the density at three times for a fiber of radius $0.0428 \mu\text{m}$ struck by a 3-Mbar shock, for a fiber-to-interfiber mass density ratio of 4:1. A measure of the fiber's mixing or destruction time may be made by determining the fraction of fiber material that lies outside the initial radius of the fiber from its center of mass (this is shown in Fig. 100.2). If we take the fiber destruction time as the time it takes for the flow to expel 75% of the fiber material from this region, we see that the fiber is destroyed in ~ 13 ps.



TC6800

Figure 100.1

Density profiles at 4, 8, and 12 ps for a Mach-24 shock interacting with a CH fiber. The density ratio is 4:1.

The Interaction of a Shock with Many Fibers

Consider now the case of a shock driven into a field of randomly placed fibers. Here the shocked fibers interact with one another, creating a “mix” region in which the post-shock vorticity mixes the CH and DT. The density $\rho(x, y)$ at 96 ps is shown in Fig. 100.3(a) for a $\text{CH}(\text{DT})_4$ wetted foam struck by an 8-Mbar shock with impedance-matched inflow boundary

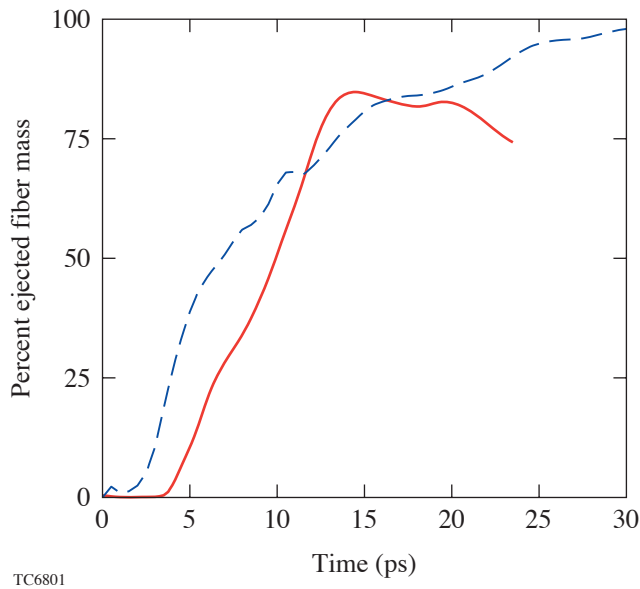


Figure 100.2

The fraction of fiber mass that lies outside the original fiber radius of the fiber's center of mass as a function of time. As the fiber material is mixed with the ambient material, it is flung outside of its original boundaries. The solid line is a single fiber with a 4:1 density ratio with the interfiber material (see Fig. 100.1). The dashed line is from a simulation of fiber destruction in the presence of other fibers. Taking the 75% mark as an arbitrary measure of fiber destruction, the fiber is destroyed after ~ 12.3 ps for a single fiber and ~ 13.5 ps in the presence of other fibers, although in this case the fiber destruction is much more thorough.

conditions. As was shown in Ref. 14, if the interfiber distance is sufficiently large, the fibers enter a noninteracting regime where the fibers are destroyed before they expand far enough to interact with one another. The parameters of interest here are in the interacting regime. The CH fiber density ρ_{CH} alone is shown in Fig. 100.3(b). The dual-vortex motion and the resulting mushroom-shaped features due to shock passage can be seen in Fig. 100.3(b). From this figure we see that CH and DT, which are clearly distinct at the shock front (the dotted line at $\sim 5.4 \mu\text{m}$), are well mixed by the end of the mix region (at $\sim 4 \mu\text{m}$). We also note from this figure that there is a thin region between the shock front at $\sim 5.4 \mu\text{m}$ and the shocked fibers ($\sim 5.3 \mu\text{m}$ at $y = 0.2 \mu\text{m}$). This gap between the shock and the entrained shocked CH is due to the finite time the post-shock flow takes to accelerate the fibers to the post-shock speed. In this region the average density, being primarily that of the shocked DT, is lower than in the rest of the mix region, contributing to an initial under-compression behind the shock.

Figure 100.2 shows that when a fiber is mixed in the presence of other fibers, the mixing proceeds more quickly initially and is more thorough (see also Ref. 14). For the simulation used here, the ejected fiber mass asymptotes near 100%. The degree of mixing may be demonstrated by designating one of the fibers as a third species identical physically to CH but maintained as a separate material numerically. Figure 100.4 shows contours of density for a particular fiber (solid lines), as well as the total density (grayscale). By 120 ps, the outermost contour, which represents 10% of the peak density, contains a volume of $0.063 \mu\text{m}^2$. This is comparable to the specific volume $0.04 \mu\text{m}^2$ of the fibers for this initial spacing.

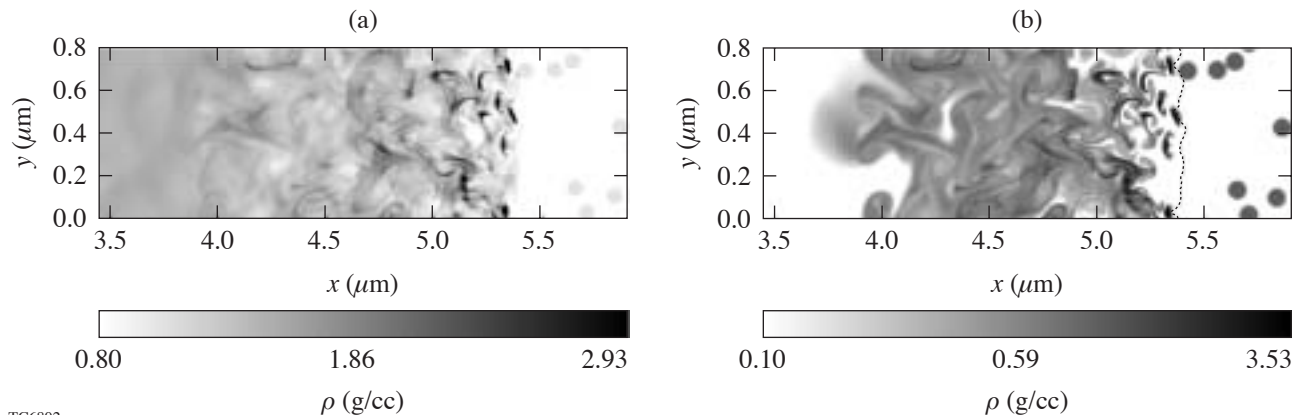
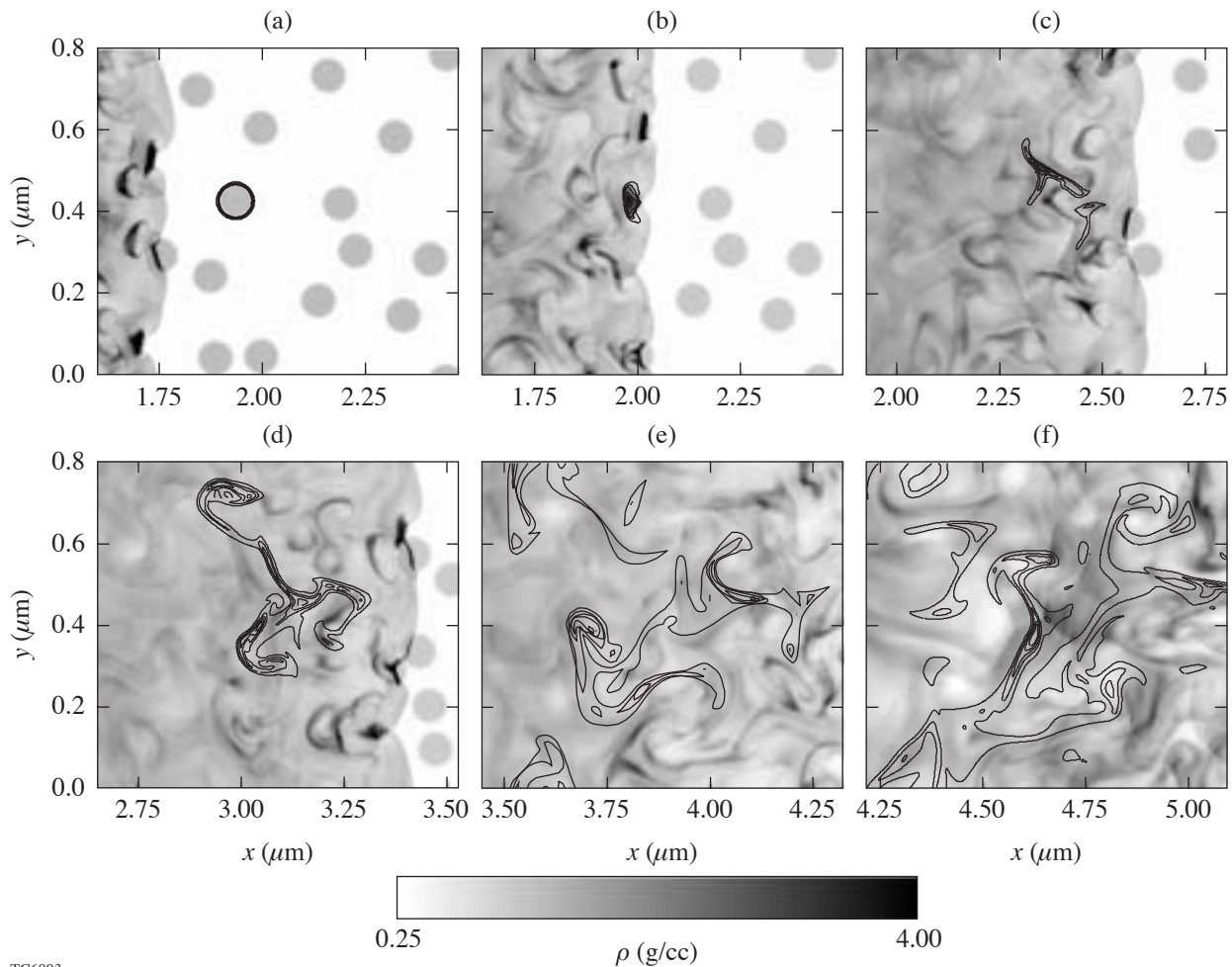


Figure 100.3

The total density (a) and CH density (b) at 96 ps for an 8-Mbar shock driven into wetted foam. The dotted line in (b) shows the location of the shock front.

The mix region is also the source of the bow shocks reflected when the main shock encounters the fibers. These shocks eventually propagate away from the main shock and out of the mix region. The fluctuations in density, pressure, and transverse velocity can be seen in their y averages — $\bar{\rho}$, \bar{p} , and \bar{u}_y — shown in Fig. 100.5 for the simulation of size $16 \mu\text{m} \times 0.2 \mu\text{m}$. (A horizontal bar is used to indicate an average over the y coordinate.) The mixing flow, due to the reflected shocks and the post-shock vorticity, is generally both horizontal — parallel to the shock motion — and vertical. The vertically moving shocks are unsupported since the flow supporting the shock is entirely horizontal. The vertical shocks, then, decay as the shocked fibers sink into the mix region. In addition, since on

average the upward-moving shocks will have the same strength as the downward-moving shocks, one might expect the net vertical speed once these have passed to be approximately zero. Because of the random fiber placement, though, some vertical motion remains behind the shock [Fig. 100.5(c)]. In the $0.2\text{-}\mu\text{m}$ -wide simulation, the periodic upper- and lower-boundary conditions, combined with the small vertical simulation size, mean that vertical motion as large as $10 \mu\text{m/ns}$ remains, even several microns behind the shock. In the $8\text{-}\mu\text{m} \times 0.8\text{-}\mu\text{m}$ simulation, \bar{u}_y in the mix region is smaller. This is because in the wider simulation there are fibers for a transverse shock to encounter other than the fiber that created it.



TC6803

Figure 100.4

The total mass density (grayscale) and the mass density (lines) of material from a “tagged” fiber initially at $x = 1.93 \mu\text{m}$ and $y = 0.42 \mu\text{m}$. The contour levels for the tagged fiber correspond to 10%, 32.5%, 55%, and 77.5% of the peak tagged-fiber density. The frames are from (a) 30 ps, (b) 35 ps, (c) 45 ps, (d) 60 ps, (e) 80 ps, and (f) 100 ps.

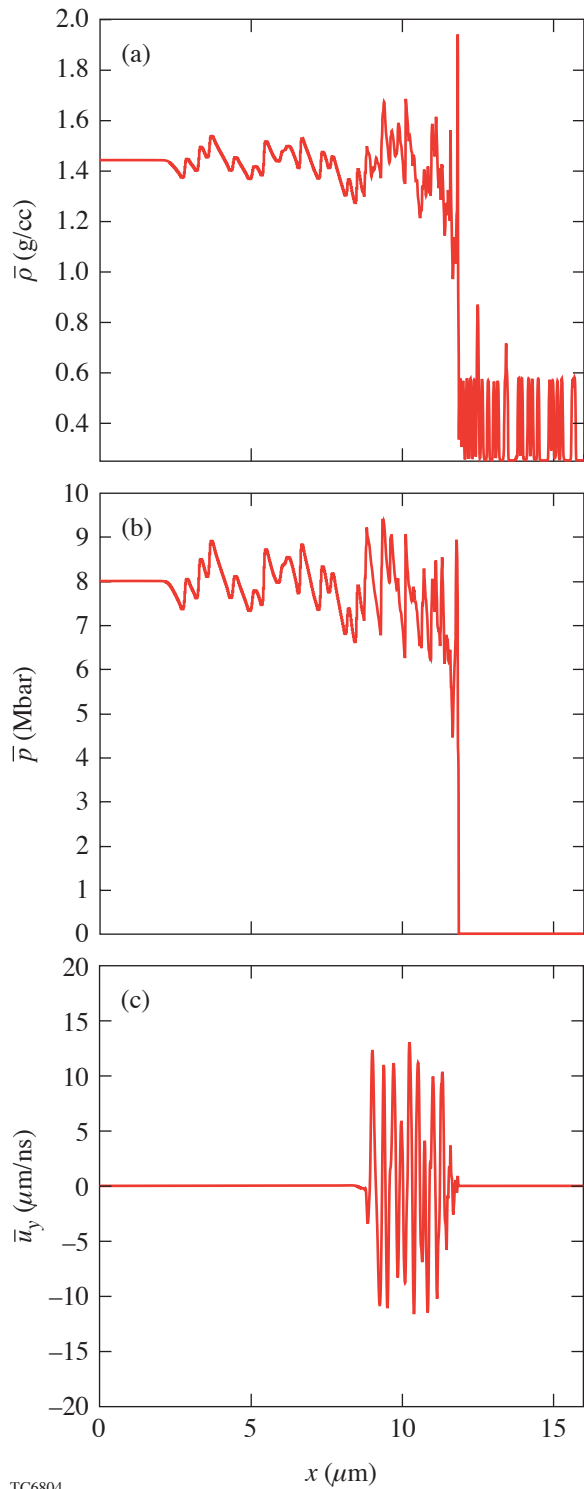


Figure 100.5
The y-averaged density (a), pressure (b), and y velocity (c) at 300 ps for a $16\text{-}\mu\text{m} \times 0.2\text{-}\mu\text{m}$ simulation.

To quantify this we have calculated average quantities related to the flow behind the shock. The mix region is given approximately by the region bounded on the right by the shock $x_s(y;t)$ (assuming the shock is a single-valued function of y) and on the left by the interface between the pusher (or inflowing material) and the shocked wetted foam, $x_i(y;t)$, as is shown in Fig. 100.6. If the wetted-foam layer is preceded by a CH layer, for instance, then there will be a contact discontinuity at the pusher/foam interface, where the density jumps but the pressure is constant. The location of the fiber material in the mix region is shown in Fig. 100.3(b), demonstrating that the vorticity quickly mixes the CH and the DT behind the shock front. For small fiber-to-DT density ratios the fluctuations in the shock-front position as a function of y are small enough to allow us to define an average shock position $\bar{x}_s(t)$. The average pusher location $\bar{x}_i(t)$ is given, for a strong shock with $\gamma = 5/3$, approximately by $\bar{x}_i \approx \bar{x}_s(t=0) + 3\bar{D}t/4$, where \bar{D} is the average shock speed. The interface position may be inverted to give the time $\bar{t}_i(x)$ when the interface is a distance x behind the shock. The time average of a flow variable q , from when it is

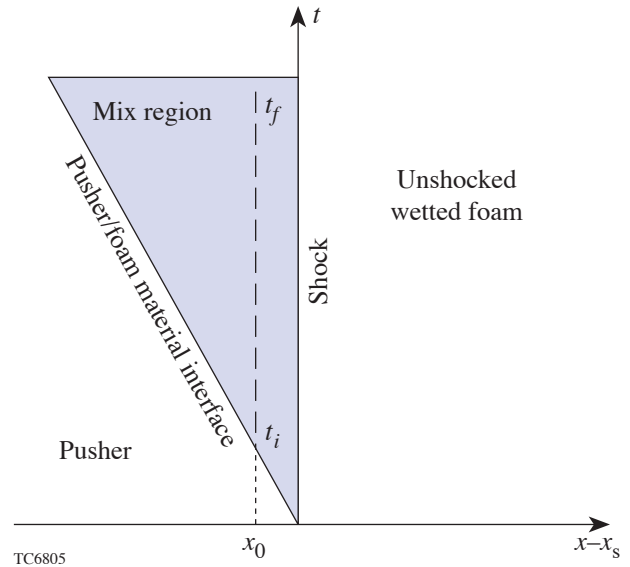


Figure 100.6
The mix region (shaded), pusher, and unshocked material are shown as a function of time, in the frame of the main shock. The time averages are computed of the flow variables in the mix region between the shock and the pusher as functions of the distance behind the shock. For instance, the time average at a distance x_0 behind the shock is found by averaging from time t_i to time t_f .

first shocked to some final time t_f , as a function of the distance x behind the shock, is then

$$\langle \bar{q} \rangle(x) = [t_f - t_i(x)]^{-1} \int_{t_i(x)}^{t_f} \bar{q}(x,t) dt,$$

where \bar{q} is the average of $q(x,y)$ over y and brackets are used to indicate this *mixing-depth average*. The distance x behind the main shock front may be thought of as a depth within the mix region. The mixing-depth average can also be taken of any quantity independent of y , such as q_n , the n th Fourier-mode amplitude of some variable q , in the y direction, or q_{rms} , the root-mean-square (rms) deviation of q as a function of y . This double average $\langle \bar{q} \rangle$ is meaningful when the flow reaches a steady state in which the average behavior of the fluctuations as a function of distance behind the shock is roughly constant in time. We have found this to be the case after the initial stages of our simulations. Note that the averaging time is inversely proportional to the distance from the shock front, so the statistical fluctuations tend to be larger for greater distances from the main shock front. The mix-depth averages of the root-mean-square variations in the y direction are shown for the pressure, the density, and the ratio of kinetic energy (in the pre-shock frame) to total energy $E_{\text{kinetic}}/E_{\text{total}}$, and u_y in Fig. 100.7, for

the $8\text{-}\mu\text{m} \times 0.8\text{-}\mu\text{m}$ and $16\text{-}\mu\text{m} \times 0.2\text{-}\mu\text{m}$ simulations discussed above. The decay scale length

$$L_q = dx/d \ln \langle q_{\text{rms}} \rangle \quad (1)$$

just behind the shock in the mixing region for these variables is comparable to $1\text{ }\mu\text{m}$ for this foam density. The relative Fourier-mode amplitudes of modes 1 to 6 of the pressure (not shown) remain roughly constant with mix-region depth, suggesting that the power is not moving to shorter or longer wavelengths, but decaying uniformly at a rate independent of mode number.

The rms amplitudes for a simulation of the same size but 50%-higher resolution are approximately equal to those in Fig. 100.7, indicating resolution convergence. Since the rate of decay of fluctuations is independent of resolution, the decay is not due to numerical losses, but to the mechanisms described above. When viscosity is negligible, the circulation in a given region is conserved according to Kelvin's circulation theorem (see, for instance, Ref. 29); in effect, vortices are "frozen" into the fluid and are advected with the flow. For the case of cylindrical fibers, as mentioned above, the vortices are created in opposing pairs with no net average vorticity generation. As

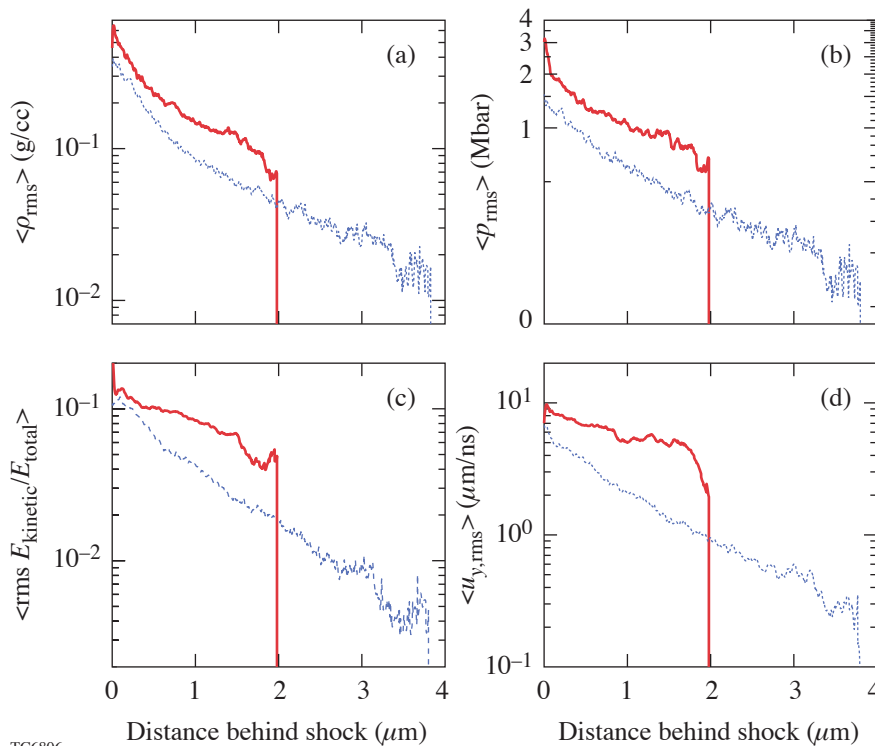


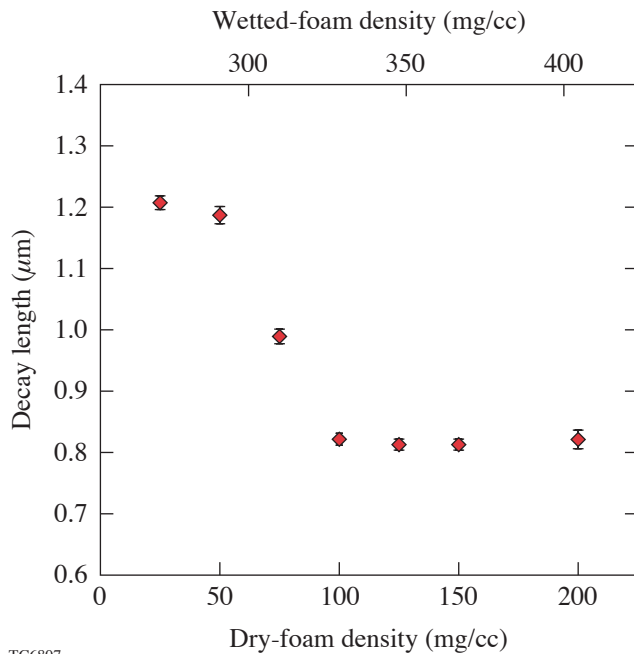
Figure 100.7

The rms variations of the time-averaged density (a), pressure (b), fraction of kinetic energy (in the pre-shock frame) (c), and vertical velocity (d) as functions of the distance behind the shock. These show a decay length comparable to $1\text{ }\mu\text{m}$ for this foam density.

TC6806

the vortices interact behind the shock, they are free in time to mix, but not decay, because of the absence of physical viscosity and the small size of the numerical viscosity. The level of mixing can again be gauged qualitatively by Fig. 100.4. In the 16- μm simulation the mixing is sufficient to reduce the time average of the rms variations to 1.2% for ρ , 1.8% for p , and 0.9% for $E_{\text{kinetic}}/E_{\text{total}}$, of the average values.

The pressure decay length [Eq. (1)] behind the shock as a function of foam density is shown in Fig. 100.8. These values are taken from simulations that have a simulation region of $8 \times 0.2 \mu\text{m}$ and an equivalent grid size of 6400×160 . The error bars in this plot are given by the linear regression used to calculate the mixing length. Poludnenko *et al.* found,¹⁴ for simulations with a larger ratio of fiber to interfiber density, that the mixing was more efficient when the average minimum interfiber distance was less than a critical distance. We find the same result: for dry-foam densities less than $\sim 75 \text{ mg/cc}$, for which the interfiber distance is ~ 6.6 times the fiber radius, the mixing length is about $1.2 \mu\text{m}$, as opposed to about $0.8 \mu\text{m}$ for higher densities. The difference between the interacting and noninteracting regimes is illustrated by considering the vor-

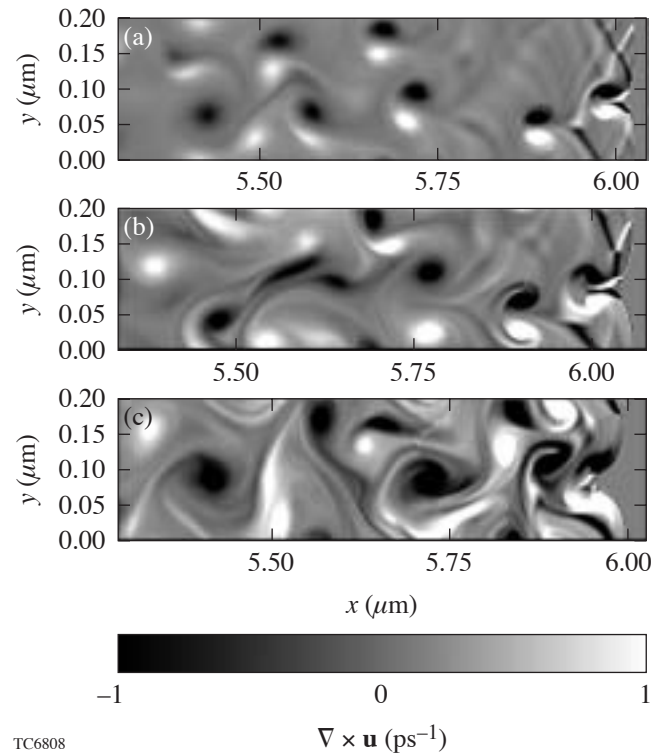


TC6807

Figure 100.8

The decay length behind the shock as a function of foam density. The decay length is approximated by the scale length of the time-averaged decay of pressure variations just behind the shock. The error bars are given by the uncertainty in the exponential fit.

ticity generated by the shock. This is shown in Fig. 100.9 for three foam densities—25, 75, and 150 mg/cc—for about the same shock position. For these three densities, as mentioned above, the average distance from fiber center to fiber center is the same, but the fibers are of different sizes. The fiber radius is given by $a = R[\rho_{\text{dry}}/(\pi\rho_{\text{CH}})]^{1/2}$, so these densities correspond to fiber radii of $0.0175 \mu\text{m}$, $0.0302 \mu\text{m}$, and $0.0428 \mu\text{m}$. For 25-mg/cc density, the vortex dipoles associated with each fiber remain paired and intact for much longer before interacting with other neighboring vortex dipoles. In contrast, for 150 mg/cc, the dipole length increases much more quickly, resulting in greater mixing.



TC6808

Figure 100.9

The vorticity is shown as the shock reaches $\sim 6 \mu\text{m}$ for three dry-foam densities: (a) 25, (b) 75, and (c) 125 mg/cc. The average interfiber distance is the same in all three cases, while the fiber radius is larger for higher foam densities.

The Rankine–Hugoniot conditions represent conservation of energy, momentum, and mass for a steady flow of polytropic gas in the absence of transverse motion. The RH jump conditions will be met over a region only to the degree that (1) the shock is steady; (2) the flow in and out of the region is steady; (3) the fluctuations at the left and right boundaries are uncorrelated (e.g., $\langle \overline{\rho u_x} \rangle = \langle \overline{\rho} \rangle \langle \overline{u_x} \rangle$; see Ref. 10); and (4) the turbulence and transverse motion have decayed at the down-

stream boundary. The shock steadiness is given by the error of the linear regression used to determine the shock speed; for the 16- μm simulation, the speed is $54.32 \mu\text{m/ns} \pm 0.033 \mu\text{m/ns}$ — an uncertainty of 0.12%. As mentioned above, the post-shock flow is approximately steady. The pre-shock flow is approximately steady when averaged over time scales much longer than the characteristic time scale for the inflowing density fluctuations, which is given by the time it takes the shock to move from one fiber to the next, $\sim d/D$. For an 8-Mbar shock and a dry-foam density of 150 mg/cc, the shock speed is $\sim 50 \mu\text{m/ns}$, and the averaging time must be longer than ~ 4 ps. The duration of the 16- μm simulation is, for instance, ~ 300 ps. The fluctuations in the mix region are correlated by up to $\sim 10\%$ just behind the shock, but these correlations decrease to a fraction of a percent beyond 1 μm from the shock. The transverse velocity is $\sim 1 \mu\text{m/ns}$ for most of the mix region, and the rms variations decay to $\sim 0.4 \mu\text{m/ns}$ by a mix-region depth of 4 μm (see Fig. 100.7). Post-shock turbulence leads to an average excess of kinetic energy in the mix region (as in Ref. 9) of 2%. Figure 100.10 shows the double averages of the density, pressure, the ratio of kinetic energy to total energy (in the pre-shock frame), and u_y , for the 16- μm simulation. Each of these quantities approaches the value predicted by the Rankine–Hugoniot (RH) jump conditions and by the end of the mix

region is within a few percent of those values. The pressure in the majority of the mix region is 7.86 ± 0.05 Mbar, 2.5% lower than that of a homogeneous simulation with the same boundary conditions. The density over the same region is 1.47 ± 0.01 g/cc, 1.7% higher than the RH value. Not surprisingly, the small deviation from the RH values results in a shock speed of $56.17 \pm 1.7 \mu\text{m/ns}$, which is near the RH shock speed (here it is within 0.1%). The post-shock adiabat $\alpha \sim p\rho^{-5/3}$ deviates from the RH value by a comparably small amount:

$$\delta \ln \alpha = \delta \ln p - \frac{5}{3} \delta \ln \rho \sim -4\%.$$

This deviation from the RH jump conditions is well within the tolerance of high-gain, direct-drive foam designs for the NIF. The main effect of variation in the speed of the first shock is mistiming of the shocks. If the shock is too slow, for instance, then the first two shocks will meet in the inner-fuel regions of the shell, preheating the fuel and compromising target performance. This effect can be simulated in 1-D by deliberately mistiming the first shock, by varying the length of the foot pulse. This is shown for a particular high-gain, wetted-foam NIF target design (see Fig. 100.11).⁴ Here a 10% change in shock speed corresponds to a shock mistiming of 300 ps, and

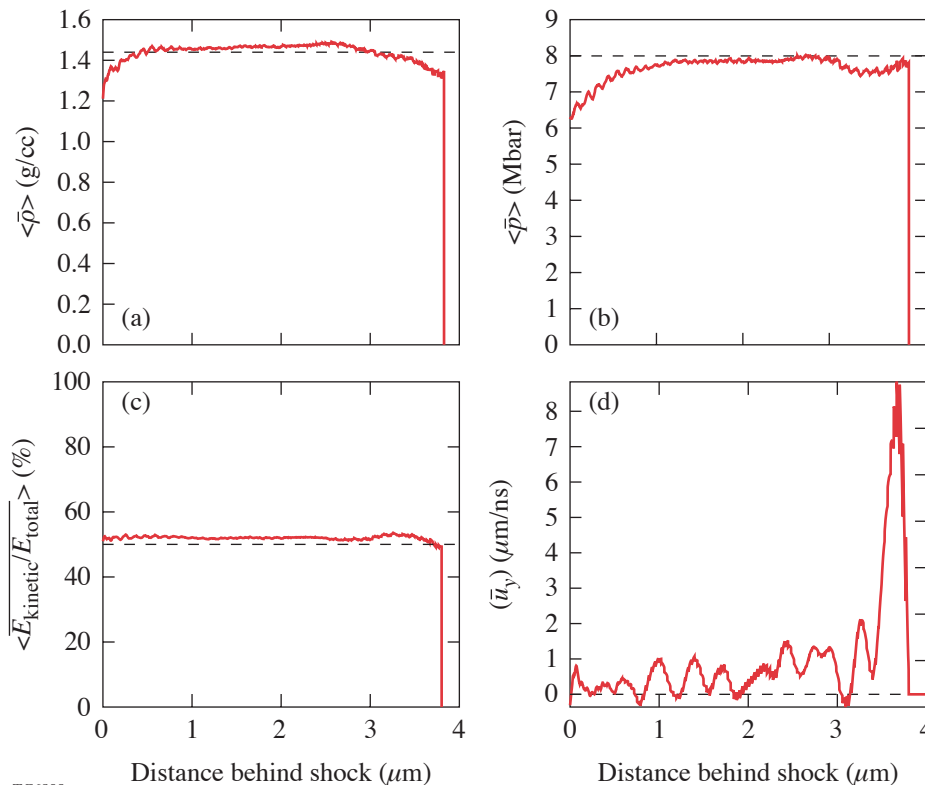
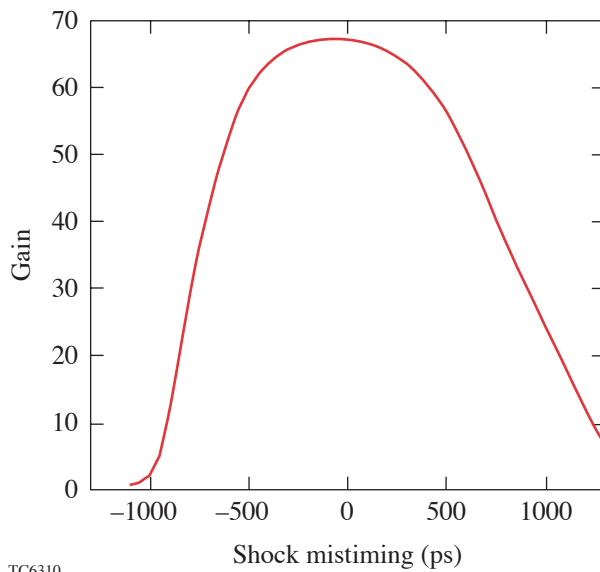


Figure 100.10

The time- and space-averaged density (a), pressure (b), ratio of kinetic to total energy (in the pre-shock frame) (c), and vertical velocity (d) as functions of the distance behind the shock front. The values given by the Rankine–Hugoniot jump conditions for a homogeneous mixture of the same density are also shown (dashed lines).

TC6809

the target shows little change in gain for a mistiming of >400 ps. For this design, at least, this suggests that any change in shock speed due to foam microstructure will have little effect on target performance. While the shock speeds for relevant pressures in DT-wetted plastic foams have yet to be measured experimentally, dry-foam shock speeds have been shown to agree to within experimental error with Rankine–Hugoniot values over a wide range of densities.³⁰



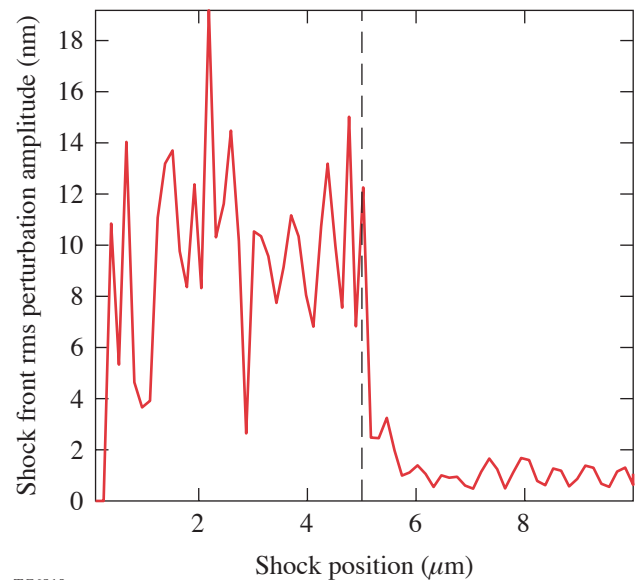
TC6310

Figure 100.11
The target gain as a function of first-shock mistiming for a high-gain, wetted-foam, direct-drive NIF target design.

As the shock propagates through the wetted-foam layer, the shock front acquires perturbations due to the different shock speeds in the DT and CH [see Fig. 100.3(a)]. Shock-front perturbations are potentially able to seed velocity and surface perturbations on the inner surface of the target shell—a process called *feedthrough*. When the shock reaches the inner shell surface, a rarefaction wave is launched toward the outer surface of the shell. These inner-surface perturbations are carried to the outer surface of the shell by this rarefaction wave—so-called *feedout* (see, e.g., Ref. 31 for a further description of these phenomena). During the acceleration phase as the laser ablation drives the implosion of the shell, the outer surface is subject to the Rayleigh–Taylor instability, which may magnify position and velocity perturbations at the outer shell surface. During the deceleration phase of an implosion, the inner surface is also subject to the Rayleigh–Taylor instability, causing fed-through perturbations to grow, potentially

reducing the core temperature and shell areal density and compromising target performance.

The rms variation in the amplitude of shock-front perturbations is shown in Fig. 100.12 for a simulation where the shock has propagated through $5\ \mu\text{m}$ of wetted foam, into $5\ \mu\text{m}$ of homogeneous DT (with a transverse simulation size of $0.2\ \mu\text{m}$). In the wetted foam, the shock-front perturbations are comparable to a few nanometers. Shock fronts are stable³² because a concave perturbation leads to a locally converging shock, higher pressure, and higher local shock speed, while a convex perturbation has the opposite effect (see Ref. 33 for further discussion of shock stability). The shock-front stability causes the shock-front perturbations to decay quickly after entering the DT layer, to a level of $\sim 0.1\ \text{nm}$. These levels of nonuniformity are well below the level of the inner-surface shell ice roughness required for direct drive on the NIF.³⁴



TC6810

Figure 100.12
The rms shock-front perturbation amplitude as a function of shock position for a simulation consisting of $5\ \mu\text{m}$ of wetted foam and $5\ \mu\text{m}$ of DT. The transverse simulation size is $0.2\ \mu\text{m}$.

Results for Different Pushers

We will now consider two different inflow boundary conditions, which correspond to different ablator materials, or “pushers.” If these boundary conditions are not the same as the average post-shock conditions in the wetted foam as in the “impedance-matched” conditions used above, then secondary shocks or rarefaction waves will reflect off the wetted foam. To illustrate the role of these reflected waves, we will first con-

sider simulations in which the pusher is post-shock DT. This simulates a wetted-foam shell for which the DT ice overfills the foam shell. This will be followed by a description of simulations of a CH pusher.

The fibers and the DT are in pressure equilibrium before the shock with a pre-shock pressure p_1 . As the shock, of Mach number M and strength z , moves through the DT pusher, it raises the pressure to $p_2 = p_1 (1 + z)$ and, since $z \gg 1$ and $\gamma = 5/3$, the density to $\sim 4\rho_{DT}$. When the shock reaches the wetted foam, it encounters a jump in the average density. The strong shock is transmitted into the wetted foam, while a weak shock is reflected back into the DT pusher. The reflected shock further increases the DT pressure to $p_2 + \delta p_2$, where δp_2 depends on the density ratio and here $\delta p_2 < p_2$. In simulations where the fibers are resolved, this weak reflected shock is made up of the shocks reflected off the individual CH fibers. These reverse shocks are shown in Fig. 100.13, which shows the density averaged over y (transverse to the shock propagation) at a particular time. In this case $p_2 = 3$ Mbar, and $\delta p_2 \sim 0.5$ Mbar. Since the post-shock DT and wetted foam are in pressure equilibrium, this is also the pressure in the post-shock wetted foam. Thus the post-shock pressure in the wetted foam is also higher than p_2 , the post-shock pressure in the DT pusher. The

resulting shock speed is given by $D_i = D_{DT}(1 + \delta p_2/p_2)^{1/2}$, where $D_{DT} = [4p_2/(3\rho_{DT})]^{1/2}$ is the shock speed in the DT.

For comparison, if a shock of the same Mach number (i.e., driven by the same pressure used to drive the DT above) is launched into a homogeneous wetted-foam mixture of CH and DT (rather than a DT pusher followed by a layer where the individual fibers are resolved), it will have a shock speed of $D_h = D_{DT}(\rho_{DT}/\rho_{ave})^{1/2}$, where ρ_{ave} is the average density of the wetted foam. For $\rho_{DT} < \rho_{ave}$, $\delta p_2 > 0$ and so $D_i > D_h$ —i.e., when the shock is driven by a pusher of the same pressure p_2 the shock speed in an inhomogeneous mixture exceeds that in a homogeneous mixture. This is seen in Fig. 100.13, which shows $\bar{\rho}(x)$ and $\bar{p}(x)$ for a particular time for homogeneous and inhomogeneous mixtures driven by shocks of the same pressure p_2 and the same starting point. The degree by which it exceeds the homogeneous shock speed depends on the average fiber density and, while essentially a 1-D effect, can also be related to the fiber radius.³⁵

For a laser-driven shock, this is not the steady-state solution. In this case, the reverse shock, when it reaches the ablation surface, is no longer supported at that pressure, and a rarefaction wave is launched into the target, lowering the

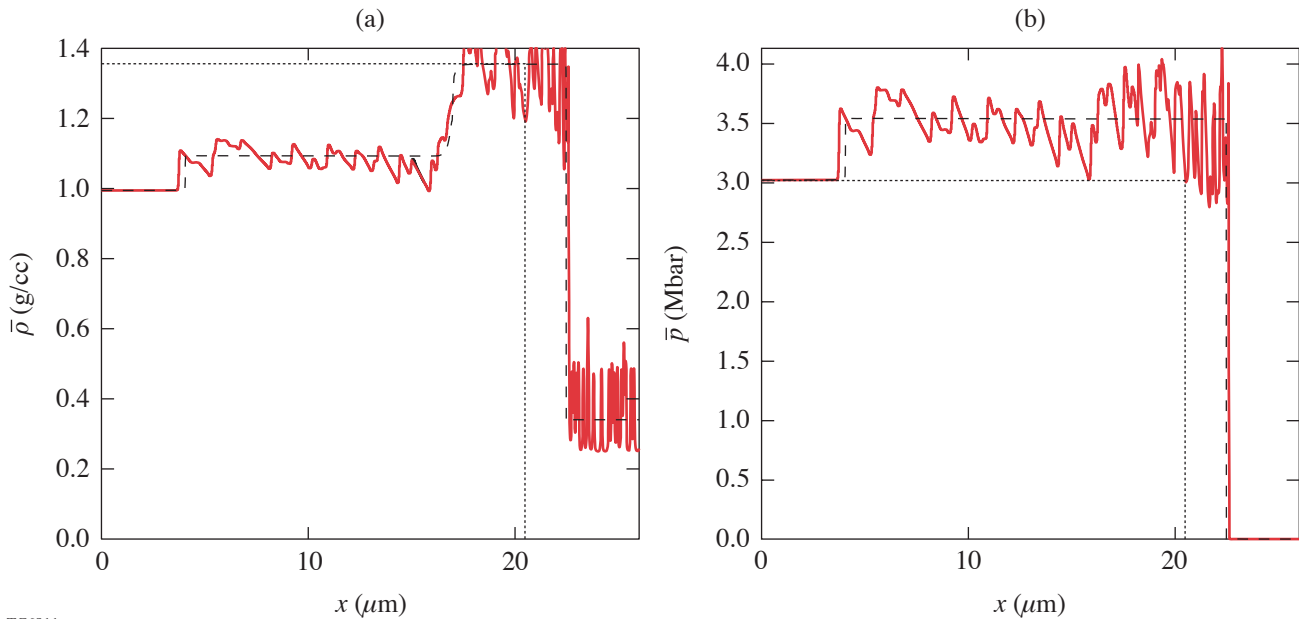
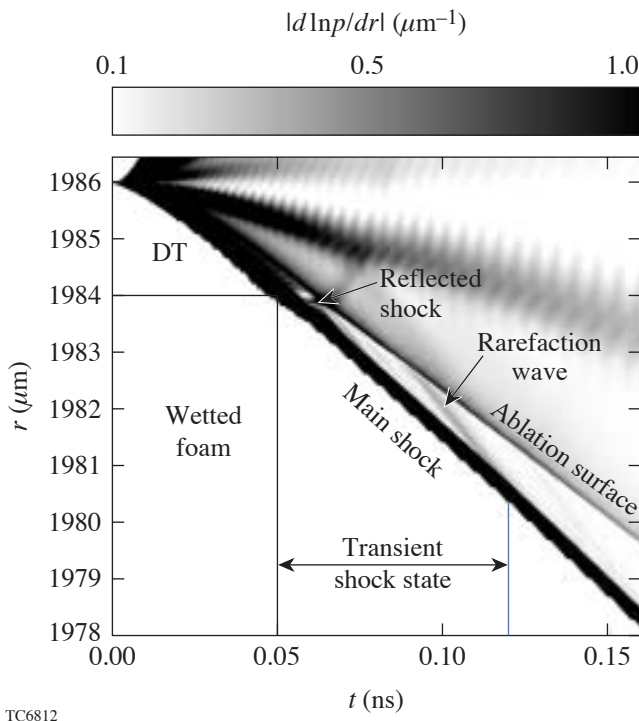


Figure 100.13

The density (a) and pressure (b) as functions of distance for a particular instance in time, for a simulation of a shock driven through wetted foam by a DT pusher. An equivalent homogeneous simulation is shown (dashed) as well as a simulation (dotted) in which pusher and foam are replaced by a homogeneous mixture with the same average density as the wetted foam.

pressure from $p_2 + \delta p_2$ to the ablation pressure, taken here to be p_2 . The trajectories of the main and reflected shocks are shown in Fig 100.14, in which the inverse of the pressure scale length is plotted for a 1-D simulation of a high-gain, NIF wetted-foam target design with a DT ablator. For this design, this transient shock state persists for 70 ps. The RH jump conditions, which must be obeyed in the case of a homogeneous mixture, are also approximately obeyed for the fiber-resolved simulation (see Fig. 100.13, where the density of the inhomogeneous case is compared to that of a homogeneous case driven with a post-shock pressure $p_2 + \delta p_2$).



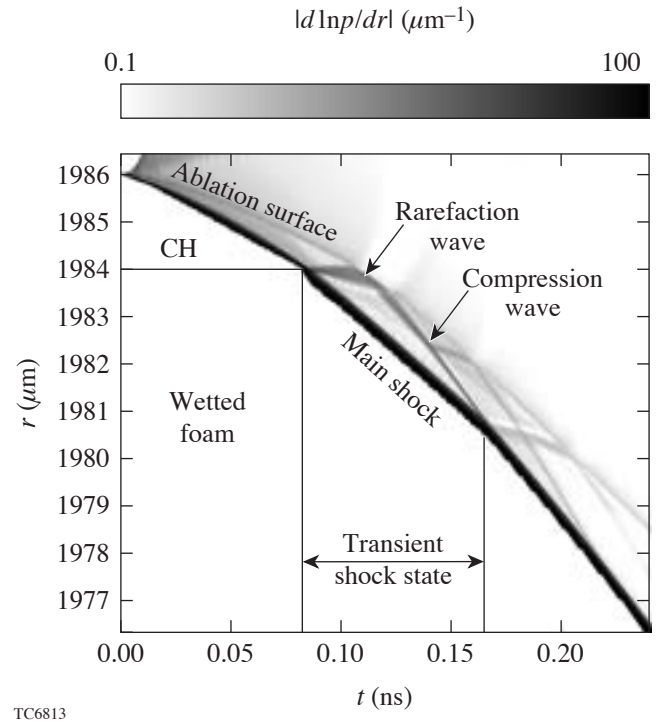
TC6812

Figure 100.14

The magnitude of the inverse of the pressure scale length for a wetted-foam ignition target design in which the wetted-foam layer is overfilled, forming an external 2- μm layer of DT. Shocks and rarefaction waves are labeled.

For target fabrication reasons, wetted-foam targets are likely to be constructed with a thin outer layer of CH, the second inflow boundary condition discussed in this section. In this case, the ablator is of higher density than the wetted foam. As a result, when the main shock moves from the CH to the wetted foam, it increases in speed. Because of this, a rarefaction wave is reflected off the interface, rather than a shock. When the RW reaches the ablation surface, where the ablation pressure is determined by the laser energy deposition rate, a weak shock or compression wave is launched back into the

target. These waves are shown in Fig. 100.15, which shows the inverse of the pressure scale length for a high-gain, NIF wetted-foam target with a $\sim 2\text{-}\mu\text{m}$ -CH ablator. In contrast to the case above of the DT pusher, the shock is undersupported until the compression wave reaches it. This transient state lasts for 100 ps in this design. Figure 100.16 shows the y -averaged pressure and density compared with a homogeneous simulation also using a CH pusher. This shows again that the RH jump conditions are obeyed, and the average shock speed is approximately the same in both cases.



TC6813

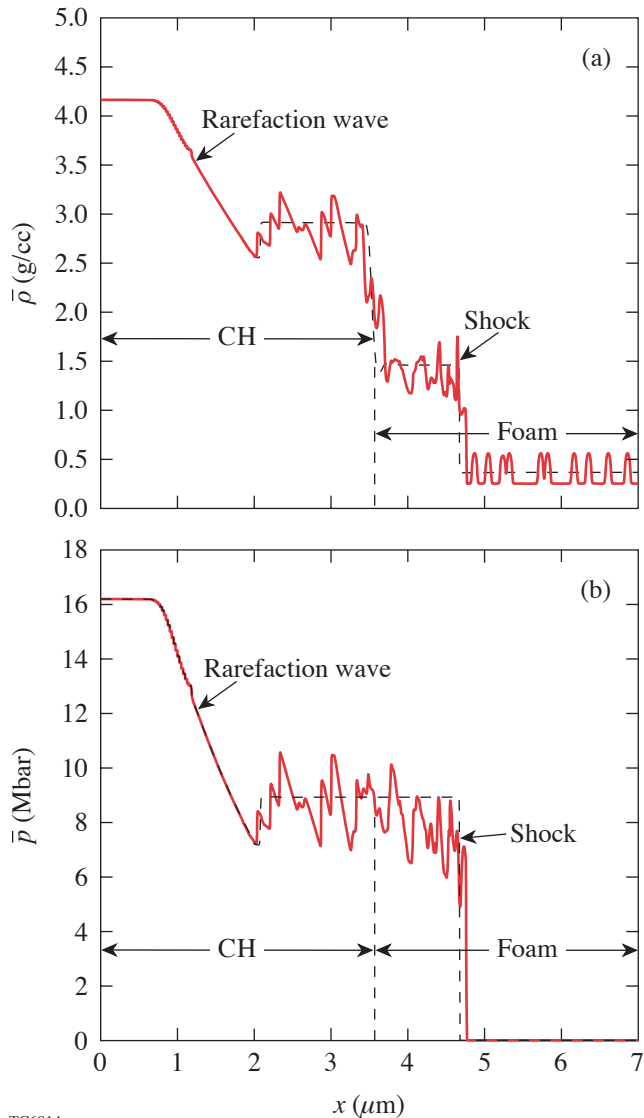
Figure 100.15

The magnitude of the inverse of the pressure scale length for a wetted-foam ignition target design with an external 2- μm layer of CH.

Conclusions

High-gain, direct-drive, wetted-foam ICF targets have been designed previously for use on the NIF and in IFE. Due to the prohibitively large range of length scales from the foam microstructure to the pellet size, simulations of these designs generally assume a homogeneous mixture for the wetted foam. We have simulated shock propagation in wetted-foam mixtures. We have found that the size of the decay length behind the shock is of the order of a micron for relevant foam densities. In the mix region, the transverse and turbulent motion decay sufficiently that the Rankine–Hugoniot jump conditions are obeyed to within a few percent. As a result, the average shock

speeds are also within a few percent of their homogeneous values. This implies that designs, which are less sensitive than this to shock timing, may be simulated using the approximation of homogeneous mixtures.



TC6814

Figure 100.16

The density (a) and pressure (b) as functions of distance are shown for a particular time, along with the values from a simulation of a corresponding homogeneous medium with the same average pre-shock density (dashed). The inflow boundary conditions correspond to a CH pusher.

We have also considered the “lifetime” of shock-front perturbations. As expected, because shock fronts are stable, perturbations seeded by the wetted-foam layer decay quickly after the shock enters the homogeneous DT-ice layer. Therefore we expect the wetted-foam microstructure to have a negligible effect on feedthrough and feedout.

Finally, we have examined the effects of using other “pushers”—DT and CH—to simulate the transient states that occur early in a target overfilled with DT ice and a target with an outer CH overcoat. The RH conditions are also met to within a few percent for these inflow conditions.

ACKNOWLEDGMENT

The author would like to thank I. Igumenshchev, P. B. Radha, and V. Goncharov for many useful discussions. This work was supported by the U.S. Department of Energy Office of Inertial Confinement Fusion under Cooperative Agreement No. DE-FC52-92SF19460, the University of Rochester, and the New York State Energy Research and Development Authority. The support of DOE does not constitute an endorsement by DOE of the views expressed in this article.

REFERENCES

1. J. Nuckolls *et al.*, *Nature* **239**, 139 (1972).
2. L. M. Hair *et al.*, *J. Vac. Sci. Technol. A* **6**, 2559 (1988).
3. D. G. Colombant *et al.*, *Phys. Plasmas* **7**, 2046 (2000).
4. S. Skupsky, R. Betti, T. J. B. Collins, V. N. Goncharov, D. R. Harding, R. L. McCrory, P. W. McKenty, D. D. Meyerhofer, and R. P. J. Town, in *Inertial Fusion Sciences and Applications 2001*, edited by K. Tanaka, D. D. Meyerhofer, and J. Meyer-ter-Vehn (Elsevier, Paris, 2002), pp. 240–245.
5. J. D. Sethian *et al.*, *Nucl. Fusion* **43**, 1693 (2003).
6. M. Desselberger *et al.*, *Phys. Rev. Lett.* **74**, 2961 (1995).
7. J. D. Lindl, *Phys. Plasmas* **2**, 3933 (1995).
8. E. M. Campbell and W. J. Hogan, *Plasma Phys. Control. Fusion* **41**, B39 (1999).
9. L. Phillips, in *Shock Compression of Condensed Matter—1995*, edited by S. C. Schmidt and W. C. Tao (AIP Press, Woodbury, NY, 1996), pp. 459–462.
10. G. Hazak *et al.*, *Phys. Plasmas* **5**, 4357 (1998).
11. A. D. Kotelnikov and D. C. Montgomery, *Phys. Fluids* **10**, 2037 (1998).
12. F. Philippe *et al.*, *Laser Part. Beams* **22**, 171 (2004).

13. B.-I. Jun, T. W. Jones, and M. L. Norman, *Astrophys. J.* **468**, L59 (1996).
14. A. Y. Poludnenko, A. Frank, and E. G. Blackman, *Astrophys. J.* **576**, 832 (2002).
15. A. Poludnenko *et al.*, “AstroBEAR: AMR for Astrophysical Applications—I: Methods,” to be published in *Adaptive Mesh Refinement—Theory and Applications*.
16. M. J. Berger and R. J. LeVeque, *SIAM J. Numer. Anal.* **35**, 2298 (1998).
17. R. J. LeVeque, *J. Comput. Phys.* **131**, 327 (1997).
18. M. Rudman, *Int. J. Numer. Methods Fluids* **24**, 671 (1998).
19. H. F. Robey, *Phys. Plasmas* **11**, 4123 (2004).
20. J. G. Clérouin, M. H. Cherfi, and G. Zérah, *Europhys. Lett.* **42**, 37 (1998).
21. M. C. Richardson, P. W. McKenty, F. J. Marshall, C. P. Verdon, J. M. Soures, R. L. McCrory, O. Barnouin, R. S. Craxton, J. Delettrez, R. L. Hutchison, P. A. Jaanimagi, R. Keck, T. Kessler, H. Kim, S. A. Letzring, D. M. Roback, W. Seka, S. Skupsky, B. Yaakobi, S. M. Lane, and S. Prussin, in *Laser Interaction and Related Plasma Phenomena*, edited by H. Hora and G. H. Miley (Plenum Publishing, New York, 1986), Vol. 7, pp. 421–448.
22. J.-Ch. Robinet *et al.*, *J. Fluid Mech.* **417**, 237 (2000).
23. A. Y. Poludnenko, K. K. Dannenberg, R. P. Drake, A. Frank, J. Knauer, D. D. Meyerhofer, M. Furnish, J. R. Asay, and S. Mitran, *Astrophys. J.* **604**, 213 (2004).
24. R. I. Klein, C. F. McKee, and P. Colella, *Astrophys. J.* **420**, 213 (1994).
25. J. M. Picone and J. P. Boris, *J. Fluid Mech.* **189**, 23 (1998).
26. N. Cowperthwaite, *Physica D* **37**, 264 (1989).
27. A. J. Lim and A. C. Raga, *Mon. Not. R. Astron. Soc.* **303**, 546 (1999).
28. M. M. Maclow *et al.*, *Astrophys. J.* **433**, 757 (1994).
29. L. D. Landau and E. M. Lifshitz, *Fluid Mechanics* (Pergamon Press, London, 1959).
30. M. Koenig *et al.*, *Phys. Plasmas* **6**, 3296 (1999).
31. R. Betti, V. Lobatchev, and R. L. McCrory, *Phys. Rev. Lett.* **81**, 5560 (1998).
32. A. E. Roberts, Los Alamos National Laboratory, Los Alamos, NM, Report LA-299 (1945).
33. G. B. Whitham, *Linear and Nonlinear Waves*, Pure and Applied Mathematics (Wiley, New York, 1974).
34. P. W. McKenty, V. N. Goncharov, R. P. J. Town, S. Skupsky, R. Betti, and R. L. McCrory, *Phys. Plasmas* **8**, 2315 (2001).
35. T. J. B. Collins, S. Skupsky, V. N. Goncharov, R. Betti, P. W. McKenty, P. B. Radha, R. Epstein, A. Poludnenko, A. Frank, and S. Mitran, in *Inertial Fusion Sciences and Applications 2003*, edited by B. A. Hammel, D. D. Meyerhofer, J. Meyer-ter-Vehn, and H. Azechi (American Nuclear Society, La Grange Park, IL, 2004), pp. 92–95.

Demonstration of Real-Time, Phase-Locked Alignment of Tiled Gratings for Chirped-Pulse–Amplified Lasers

Introduction

The OMEGA EP (extended performance) petawatt, multi-kilojoule, solid-state laser, presently under construction at LLE, includes compressors with four tiled-grating assemblies (TGA's), where each assembly contains three subaperture diffraction gratings, to compress the pulse before it is focused onto target.^{1,2} The tiled-grating compressor (TGC) was chosen to stay within the damage-threshold limitations of the largest currently available multilayer dielectric (MLD) gratings, together with the anticipated intensity modulation of the laser output beam. The four-grating compressor is shown schematically in Fig. 100.17. The holographically generated grating tiles^{3,4} have a line frequency of 1740 grooves/mm and a clear aperture of 400 × 470 mm. The individual BK-7 grating substrates have a thickness of nominally 100 mm and are approximately 50 kg in weight. For the TGC to deliver the compressed pulse with a near-diffraction-limited energy distribution on target, the individual tiles have to be aligned to each other with an optical-path difference (OPD) of less than 50 nm. An active control approach, similar to a three-actuator deformable mirror, has been chosen to maintain the correct alignment between grating tiles.

Between any two gratings there are six degrees of freedom that affect the optical performance of a tiled-grating system, as

shown in Fig. 100.18. A three-control-variables approach has been chosen to bring the gratings into the condition of coherent energy addition.⁵ This reduction in degrees of freedom is realized by grouping six variables into three pairs that mutually compensate. Differential tilt, caused by small differences in the average groove spacing, is removed by adjusting the individual grating tilt. Also, error in lateral placement of the gratings is compensated for by a small adjustment of piston. In addition, error in groove parallelism between gratings is compensated by a y-tip adjustment. Although each differential error must be kept small, compensation between pairs allows all six degrees of freedom to be nonzero while coherent addition is maintained. Using this pairing concept, a systematic alignment sequence provides convergence toward accurate coherent addition.

Several new alignment techniques have been demonstrated to achieve coherent addition of tiled gratings. The relative grating positions and all alignment measurements are made in real-time with an interferometer whose field of observation straddles the gap between the gratings. Any drift of the grating tiles from their optimal position is measured and compensated by a servo loop. The gratings are pre-aligned to have a differential piston of less than 10 μm, which is the capture range of the servo system. With the servo loop engaged, an alignment

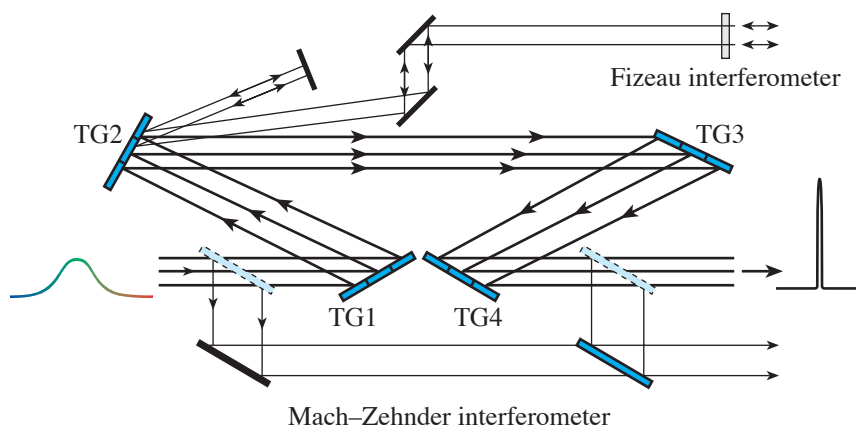


Figure 100.17

Each OMEGA EP compressor contains four tiled-grating assemblies (TGA's) per beamline, where each assembly contains three subaperture diffraction gratings. Each TGA interface requires three actuators to maintain the grating positioning needed for coherent addition of the three diffracting beams. The tiled-grating compressor (TGC) provides an aperture large enough to meet the energy requirements while operating below the laser-damage threshold of the final grating. Interferometers are deployed to maintain accurate alignment of the gratings within each TGA.

E13550

precision of ± 25 nm, or $\lambda/20$ p-v, is reproducibly achieved. In addition, as schematically illustrated in Fig. 100.17, a robust alignment system, intended for use on the OMEGA EP laser system, contains two interferometers. Individual TGA's are aligned with a Fizeau interferometer, while alignment of the entire TGC is verified with a Mach-Zehnder interferometer and a focal-spot diagnostic.

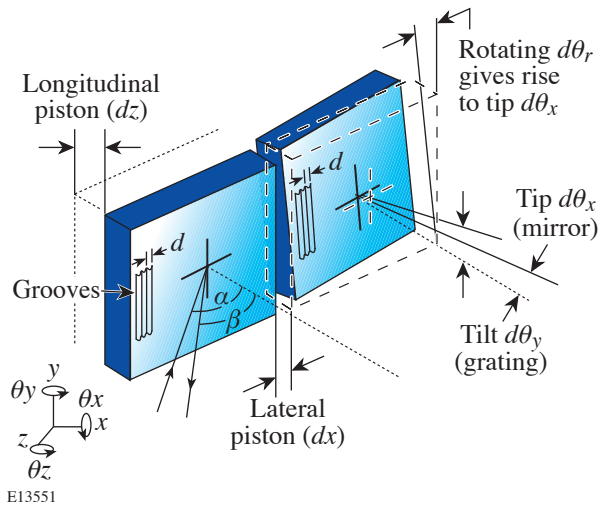


Figure 100.18

Between any two gratings there are six degrees of freedom that affect the optical performance of a tiled-grating system. These can be grouped into three compensating pairs of differential errors: longitudinal piston and lateral piston; in-plane rotation and angular tip; and average groove spacing and angular tilt. Although each differential error must be kept small, compensation between pairs removes the constraint that any particular error must be zero.

Modeling

A measure of the accuracy with which two gratings operate in the coherently additive mode is the Strehl ratio, which is defined as the ratio of the peak irradiance of an aberrated focal spot to that of an aberration-free focal spot.⁶ Computer simulations of one TGA interface show the effect of the differential grating misalignments as measured in the near field. Tip, tilt, or piston misalignment between the gratings affects the Strehl ratio to different degrees for the same magnitude of alignment error. This sensitivity is shown for piston, x tilt, y tip, and in-plane rotation in Fig. 100.19, which plots the Strehl ratio as a function of a misalignment error. Although the TGC in the OMEGA EP laser system will operate at a wavelength of 1054 nm, both modeling and prototype development were carried out at a wavelength of 633 nm because of the availability of an interferometer operating at this wavelength. To achieve accurate tiling at either wavelength, the misalignment

errors, taken individually or as compensation pairs, must be kept below $\lambda/20$ to maintain close to a diffraction-limited focal spot.

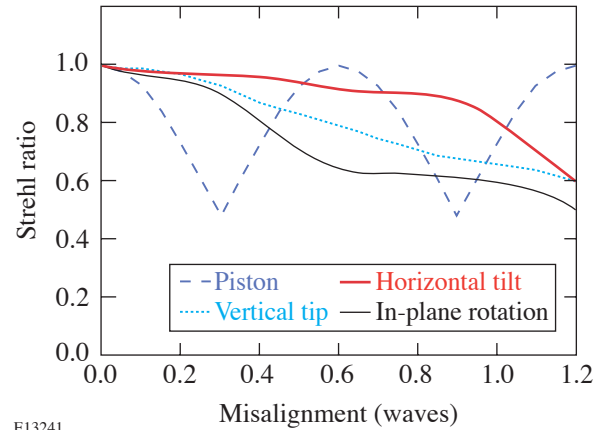


Figure 100.19

Computer simulations of one TGA interface show the effect of the differential grating misalignments as measured in the near field. The Strehl ratio is plotted as a function of individual misalignments for a wavelength of 633 nm and an incident angle of 33.4° . The misalignment errors, taken individually or as compensation pairs, must be kept below $\lambda/20$ to maintain close to a diffraction-limited focal spot.

These computer simulations show that piston is the most-sensitive drift parameter for two gratings and that the effects of piston error are cyclical with an OPD period of $\lambda/2$. Since the absolute piston error has to be less than one wavelength, any error must be corrected before it reaches $\lambda/2$; otherwise the absolute piston position can be lost due to a periodic π ambiguity. If the fringe system jumps by an error greater than $\lambda/2$, the piston must be reset independently and the tracking/correcting system restarted.

Three equations mathematically describe the paired relationship for the various degrees of freedom. Defining displacements as Δz (longitudinal piston shift), Δx (lateral piston shift), θ_x [rotation about x axis (tip)], θ_y [rotation about y axis (tilt)], θ_z [rotation about z axis (in-plane rotation)], and Δd (error in grating ruling spacing), the following three equations represent the resulting phase errors. Equation (1) represents the piston phase error while Eqs. (2) and (3) represent the phase gradients of tip and tilt, respectively, where $d\Phi/dy$ and $d\Phi/dx$ are the transverse phase gradients in the beam, α is the incident angle, and β is the diffraction angle. The objective for accurate tiling involves setting each equation to zero for the majority of spectral components of the laser pulse.

$$\Delta\Phi_z = 2\pi/\lambda[(\sin\alpha + \sin\beta)\Delta x - (\cos\alpha + \cos\beta)\Delta z] \quad (1)$$

$$d\Phi/dy = -2\pi/\lambda[(\cos\alpha + \cos\beta)\theta_x + (\sin\alpha + \sin\beta)\theta_z] \quad (2)$$

$$d\phi/dx = 2\pi/\lambda[(\cos\alpha + \cos\beta)\theta_y - (\sin\alpha + \sin\beta)\Delta d/d] \sec\beta. \quad (3)$$

Three independent actuators that produce displacements normal to the surface of the grating are used to control differential tilt, tip, and piston. The motion of a single actuator rotates the grating about an axis defined by the other two actuators. This rotation is resolved into tilt and tip components by projection of the axis onto the coordinate system axes. Piston displacement is simply the corresponding normal displacement of the grating surface at a reference point selected for piston measurement. It is convenient to combine the coefficients for tip, tilt, and piston motion due to actuator displacements into a 3×3 matrix M and to calculate its inverse M^{-1} , which is also a 3×3 matrix. Then the actuator motions required to produce a specified tilt, tip, and piston correction are described by $Z = M^{-1}C$, where Z is the row vector of required actuator displacements and C is the column vector of tilt, tip, and piston corrections.

Experimental Setup

Several different prototype assemblies were built to study error compensation, TGA-to-TGA compensation schemes, and various alignment techniques. The tiled-grating mounts are identical three-point, flexure suspensions that separate weight-bearing and adjustment functions, as shown in Fig. 100.20. The front view of a prototype TGA shows two gold-coated, 16×22 -cm gratings, manufactured by Jobin-Yvon, while the back view shows both the manual and motorized actuators. The entire TGA is mounted on a precision rotating stage to achieve rapid and repeatable angular adjustment when positioning to a normal, Littrow, or near-Littrow angle of incidence. The design emphasizes pre-loaded, easy motion in the direction of control while being very stiff in two orthogonal directions, thus minimizing parasitic motions.

The experimental test bed used to demonstrate closed-loop control of TGA's is configured on an optical table containing a Fizeau interferometer (Fig. 100.21), with an ADE Phase Shift Mini Fiz 100 front end, operating at 632.8 nm. The out-

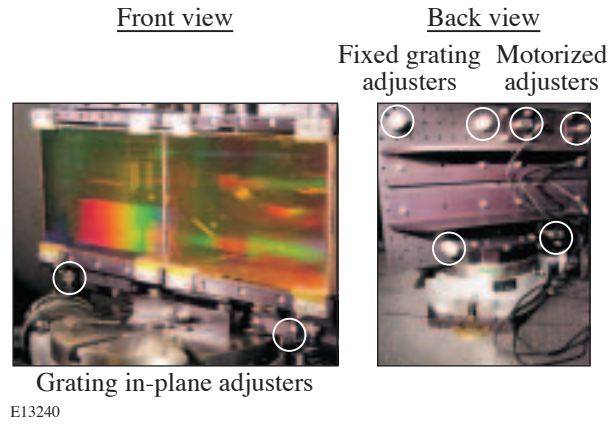


Figure 100.20

The front view of a prototype TGA shows two gold-coated, 16×22 -cm gratings, while the back view shows both the manual and motorized actuators. The TGA is mounted on a precision rotating stage to achieve rapid and repeatable angular adjustment when positioning to a normal, Littrow, or near-Littrow angle of incidence. Several different prototype assemblies were built to study error compensation, TGA-to-TGA compensation schemes, and various alignment techniques.

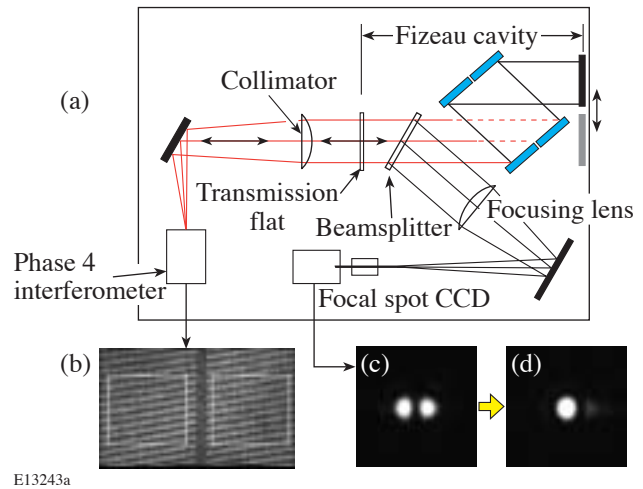


Figure 100.21

The experimental test bed used to demonstrate closed-loop control of tiled-grating assemblies (TGA's) is configured on an optical table containing a 10-in. Fizeau interferometer (a). The TGA's are positioned within the interferometer cavity for testing single- and double-pass alignment, using one TGA, or triple- and quadruple-pass alignment, using two TGA's. The fringe pattern (b) is a sample of a recorded interferogram, while (c) and (d) are examples of a piston phase error of $\lambda/2$ and a diffraction-limited focal spot, respectively.

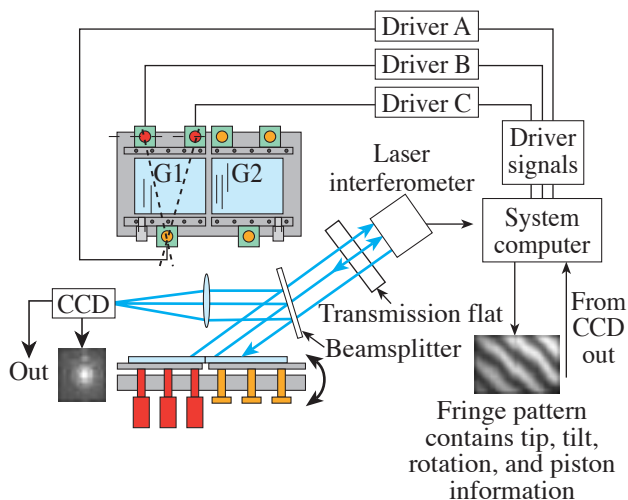
put beam was expanded to 250 mm, using a 1.8-m-focal-length lens for collimation, as shown in Fig. 100.21. A 12-in.-diam transmission flat, manufactured by Zygo, was inserted into the Fizeau cavity to send a portion of the return beam for far-field analysis, as described previously.⁷ The TGA's were positioned within the interferometer cavity for testing single- and double-pass alignment, using one TGA, or triple- and quadruple-pass alignment, using two TGA's. The fringe pattern [Fig. 100.21(b)] is a sample of a recorded interferogram, while Figs. 100.21(c) and 100.21(d) are examples of a piston phase error of $\lambda/2$ and a diffraction-limited focal spot, respectively.

One grating in the TGA was adjustable through remotely controlled piezo-type actuators (New Focus PicoMotors, model 8301)⁸, while the second grating was held steady after manual adjustment with Aerotech Differential micrometers. The suspension mounts for both gratings were mounted on a common backplate. The backplate assembly was mounted on a 250-mm-diam rotary table with a resolution of 4 arc sec (manufactured by Phase II). Parallelism of the gratings' grooves was obtained by pivoting one of the gratings about the grating normal, while the TGA was alternately positioned at normal incidence and Littrow position within the Fizeau interferometer. After several iterations, grating parallelism was adjusted to within 0.1 wave. The functional systems diagram is shown in Fig. 100.22. The prototype control system monitors grating alignment in both the near field and far field (focal spot). The cw laser light probes the gratings and is transmitted to electronic cameras to record both the fringe pattern and the corresponding focal spot. Analysis of the fringe pattern yields differential tip, tilt, and piston. From these measurements, the system computer generates signals to drive three actuators, for

each grating-to-grating interface, in a closed-loop cycle that minimizes the set of differential errors. The focal-spot diagnostic is used to verify successful convergence toward diffraction-limited performance.

Phase Measurement and Error-Signal Computation

Any drift between the two gratings is determined from a single interferogram according to a Fourier-transform (FT) method known as spatially synchronous phase detection (SSPD).⁹ Figure 100.23 shows the methodology by which this technique is used to analyze the high-frequency fringe patterns situated on either side of the TGA interface. The interferometer is adjusted with deliberate tilt between the reference and test wavefronts to produce an interferogram [Fig. 100.23(a)] that contains the surface information encoded onto a high-order spatial carrier frequency. A window function is applied to remove edge-ringing [Fig. 100.23(b)]. The FT of the interferogram [Fig. 100.23(c)] produces a dc component and two sidebands symmetrically displaced corresponding to the carrier frequency of the fringe pattern. Higher-order sidebands are present with nonsinusoidal fringe profiles. Each of the sidebands contains all of the desired phase information. The carrier frequency is chosen to place the side lobe to a position outside the noise spectrum of the interferometer system. One sideband is isolated by applying an appropriate filter in the Fourier plane and shifted to zero frequency before carrying out the inverse Fourier transform. Two-dimensional phase reconstruction of each side of the TGA interface is obtained with an inverse FT, followed by calculation of the phase from the real and imaginary components of the image. The complex phase of the inverse transform is unwrapped and represents the phase data of the surfaces [Fig. 100.23(d)]. Any remaining tip, tilt, or



E13242a

Figure 100.22

The control system monitors grating alignment in both the near field and far field (focal spot). The cw laser light probes the gratings and is transmitted to electronic cameras to record both the fringe pattern and the corresponding focal spot. Analysis of the fringe pattern yields differential tip, tilt, and piston. From these measurements, the system computer generates signals to drive three actuators in a closed-loop cycle that minimizes the set of differential errors. The focal-spot diagnostic is used to verify successful convergence toward diffraction-limited performance.

piston phase errors can be removed in the final stages of closed-loop operation. This technique is especially useful when operating in optically “noisy” environments since the single video frame measurement is fast compared to scanning interferometers and permits a high level of noise rejection, through averaging of multiple video frames in phase space.

The differential slope of the two elements represents the x tilt and y tip of the two tiles. The x tilt and y tip are determined unambiguously in the x - y coordinate system. “Piston” is the out-of-plane offset in the z direction. A linking of the left and right portions of the interferogram has to be applied across the gap to maintain phase continuity for the piston computation.

As previously described in this article, the three phase-error terms are the result of the joint effect of a pair of separate, independent grating misalignments. The piston term is the composite effect of both an actual z -direction tile offset and a lateral shift perpendicular to the grating rulings. The tip term

comprises the joint effect of actual differential tip and in-plane rotation of one of the gratings with respect to the other. The tilt term is due to differential tilt between the gratings, which can, in part, be caused by a difference in groove spacing. An error in one of the components of a two-component term may be perfectly compensated by adjusting the other component; therefore, it is necessary to provide only three adjustments per tile, provided that the grating array is designed to minimize errors in the nonadjustable offsets.

After an initial system alignment where most of the tip and tilt have been removed and the relative piston has been set within $2\pi N$, the value of N is checked by translating a high-resolution mechanical indicator across the gap on the grating surface outside of the clear aperture. The indicator is mounted on a slide that is parallel to the surface of the first grating and that places the indicator within a few millimeters, laterally, of the gap. Translating the indicator while in contact with gratings produces a step if there is an absolute piston error. The three

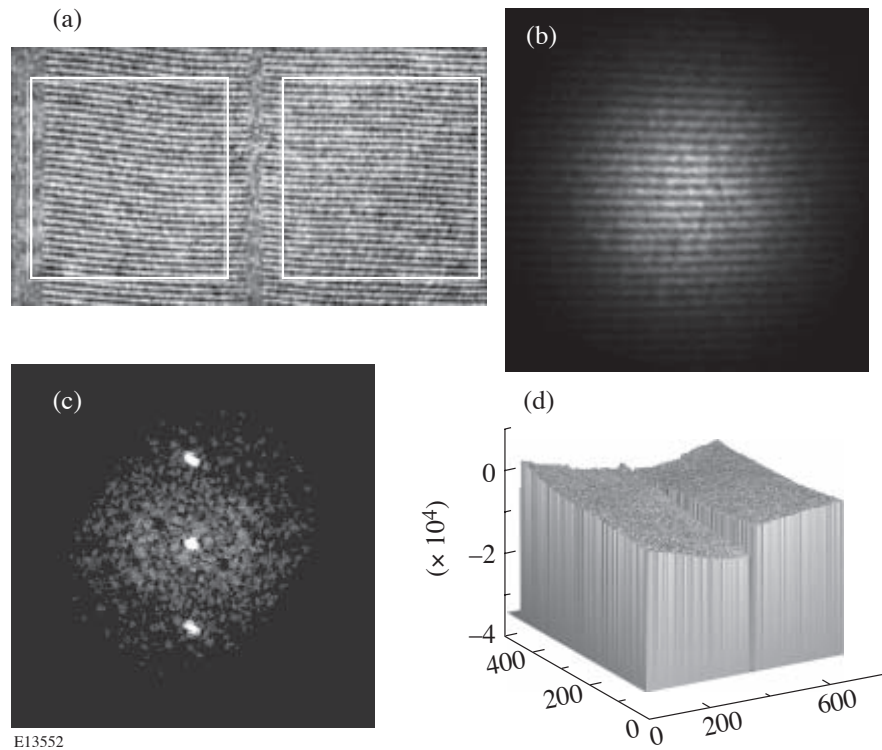


Figure 100.23

A Fourier-transform (FT)-based algorithm, referred to as spatial synchronous phase detection (SSPD), is used to analyze high-frequency fringe patterns (a) situated on either side of the TGA interface. A window function is applied to each fringe pattern (b) to reduce edge effects in the FT calculations. The carrier frequency is chosen to place the side lobe to a position outside the noise spectrum of the interferometer system (c). An inverse FT, followed by phase calculations, results in two-dimensional phase reconstruction of each side of the TGA interface. Any remaining tip, tilt, or piston phase errors (d) can be removed in the final stages of closed-loop operation.

actuators of the motorized gratings are now moved in concert by an appropriate amount to reduce the absolute piston to less than one wavelength.

Computer System and Software

The software integrates the image acquisition, image analysis, parameter derivation, and actuator control, as well as all data logging, in the same computer. The speed of the control loop is of the order of 1 s, even though the actual alignment may be corrected much less frequently. For the purpose of thorough testing, the measurement system was designed to be sensitive to both low- and high-frequency disturbances. For example, a change in room temperature induces thermal drifts typically requiring corrections of the order of minutes to hours. High-frequency disturbances that can be induced by acoustics or air turbulence are removed by averaging many individual measurements. Close to 100 measurements were typically averaged to achieve the required level of noise reduction.

A Windows-based desktop computer, with five extension slots, running at 2.5 GHz, was used to acquire interferometric data. The fringes were acquired with a monochrome CCD camera, internal to the ADE MiniFiz interferometer with RS-170 interface, and digitized with a four-channel, 8-bit data acquisition card from National Instruments, model 1409.¹⁰ Processing artificial fringe patterns showed the numerical resolution of the software to be better than $\lambda/1000$. One channel of that card was used to digitize the image of the fringe pattern, while another channel was used to acquire a far-field view used for the diagnostic of the alignment.

The control loop was completed with three Picomotor controllers (New Focus 8753) (Ref. 8) that were driven by a hardware and software package. The Picomotors are digital stepping devices that move in nominal increments of 20 nm. The data acquisition and control software was developed with a rapid prototyping environment called BlackBox Component Builder,¹¹ which is available free of charge, and compiled with a Component Pascal compiler. The Blackbox environment is very robust and stable and well suited to developing mission-critical software, which requires a low occurrence of failures. An engineering and scientific software library¹² was used to perform matrix calculations and also for data logging and display. The library, written by Robert Campbell for the Blackbox environment, is distributed in source code.

The start-up sequence involves manual grating adjustments in two different positions. The grating assembly is rotated to be

perpendicular to the interferometer axis, and both gratings, acting as mirrors, are co-aligned with respect to the Fizeau transmission flat to better than 1 μ rad. This technique is referred to as “fringe-nulling.” The grating assembly is then rotated to the Littrow position, where any measured differential vertical tilt is due to in-plane grating rotation. The fringe pattern is “nulled” with separate adjustments for both gratings to ensure that the grating grooves are parallel to one another. It may be necessary to reiterate these last two steps to make certain that the adjustments have settled and the adjusters are locked.

The reference transmission flat is now tilted to produce approximately 15 to 20 fringes across the field to enable the SSPD techniques to work with sufficient precision. Care must be taken to maintain wedge orientation within the interferometer and to maintain the same sign convention throughout the processing software. Once the manual setup steps are complete, the system is ready to perform open-loop stability measurements with the motors disabled. Alternatively, the control loop may be closed for precise grating control.

Experimental Results

The interferometric system was evaluated by measuring the differential phase between two regions of the same grating over an extended period of time. Each data point was acquired by averaging 16 sequential video frames. As shown in Fig. 100.24, an alignment variation of $\lambda/50$ rms was observed

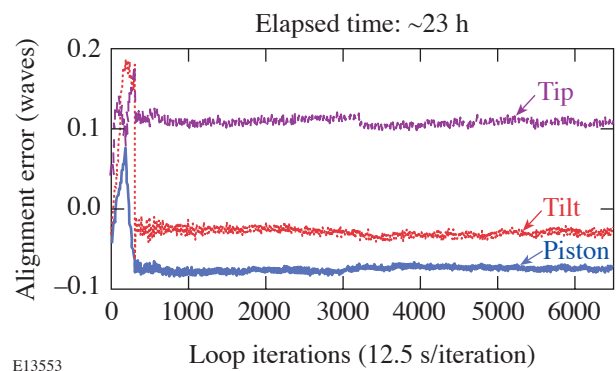


Figure 100.24

The stability of the phase sensor is evaluated by measuring the differential phase between two regions of a stable, monolithic grating. Long-term measurement of tip, tilt, and piston phase errors establishes the noise level of the system to be approximately $\lambda/50$. Statistical analysis, applied over time intervals of several minutes, reduces the measurement error to below $\lambda/100$. Extraneous fluctuations prior to sample 300 are reduced by applying temporal averaging in the SSPD routine.

over this period. Statistical analysis, applied over time intervals of several minutes, reduces the measurement error to below $\lambda/100$. Extraneous fluctuations prior to sample 300 were reduced by applying temporal averaging in the SSPD routine. After replacing the single grating with two gratings, phase measurements were made in open-loop mode over a 24-h period. As shown in Fig. 100.25, long-term monitoring of a TGA, with disabled actuators, indicates tip and tilt stability while the differential piston drifts by more than the wavelength of light. The system stability was found to vary by approximately five wavelengths of light per degree centigrade. The apparent phase jumps at $\pm\lambda/2$ are due to the $-\pi$ to π range of the arctangent calculation performed in phase reconstruction.

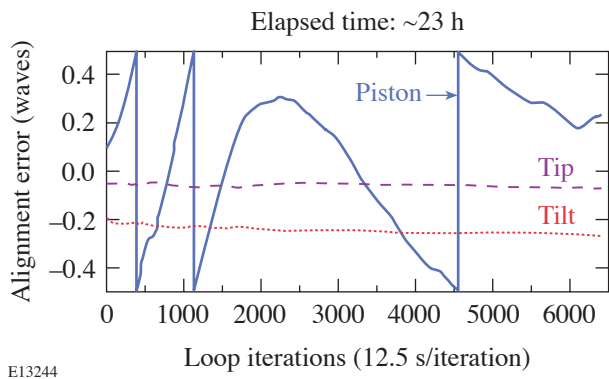


Figure 100.25

Long-term monitoring of a TGA, with disabled actuators, indicates tip and tilt stability while the differential piston drifts by more than the wavelength of light. The apparent phase jumps at $\pm\lambda/2$ are due to the $-\pi$ to π range of the arctangent calculation performed in phase reconstruction. The overall cyclical behavior of the piston term is caused by the difference in the coefficient of thermal expansion between the Pyrex™ substrate and aluminum mount in the presence of small temperature changes in the environment.

As a result of the phase-pair compensation strategy, any drift in either “y tip” or “in-plane grating rotation” is contained in the vertical “tilt signal,” and their sum can be corrected with the servo system. Similarly, any drift in longitudinal shift (piston) or lateral shift is contained in the “piston signal,” and their sum can be corrected by the servo system. A temperature recording, and subsequent analysis, showed that the cyclical behavior of the piston term is caused by the difference in the coefficient of thermal expansion between the Pyrex™ substrate and the aluminum mount in the presence of small temperature changes in the environment. The largest dimensions of the assembly are the widths of the gratings and the support structure. Since changes of these dimensions, due to temperature variation, are different for dissimilar materials, a

phase shift occurs between the sets of grooves from their respective grating.

Closed-loop control of a TGA is achieved by driving the actuators with signals derived from the phase sensor. Phase fluctuations (Fig. 100.26) were largely reduced when the actuators were activated at sample number 9, and $\lambda/10$ alignment was rapidly achieved at sample number 25. As marked by sudden shifts in the plots, differential piston occurred at sample numbers 52 and 142. Tip and tilt phase correction was not required over the same time period. At the end of closed-loop operation, piston corrections in one-step increments, or 20 nm, are observed. This is comparable to the operation with a single grating where the far-field signal approximates a steady Airy pattern, with a Strehl ratio of about 0.99. During operation of an OMEGA EP laser beam, closed-loop control of up to eight interfaces will be required.

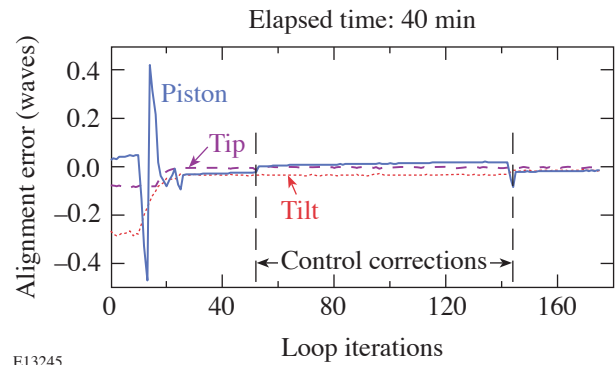


Figure 100.26

Closed-loop control of a TGA is achieved by enabling the actuators with signals derived from the phase sensor. Phase fluctuations were largely reduced when the actuators were enabled at sample number 9, and $\lambda/10$ alignment was achieved at sample number 25. As marked by sudden shifts in the plots, differential piston occurred at sample numbers 52 and 142. Tip and tilt phase correction was not required over the same time period.

An important demonstration of closed-loop control of the TGA involved obtaining convergence of all of the measured differential phase errors to zero following random offsets to the actuators [Fig. 100.27(a)]. Both the focal-spot irradiance and computed Strehl ratio tracked very well with the recorded differential piston. A focal spot splits into two lobes for a piston error of $(2N+1)\pi$ [Fig. 100.27(b)], while an Airy pattern [Fig. 100.27(c)] is recovered as the piston misalignment returns to near zero: For this experimental demonstration, the irradiance doubled after successful closed-loop alignment

[Figs. 100.27(d) and 100.27(e)]. A closed-loop run, requiring correction of initial tip, tilt, and piston errors, is completed in approximately 5 min. The settling time depends on the severity of the initial misalignments.

Operational ease can be achieved for closed-loop control of a tiled-grating compressor (TGC) through simultaneous alignment of all TGA's in a series configuration. Series align-

ment was demonstrated by positioning two TGA's in double-pass configuration using an auxiliary retroreflecting mirror. While one TGA was intentionally misaligned with a piston error of π radians [Fig. 100.28(a)], the second TGA was adjusted to remove all piston error from the series configuration [Fig. 100.28(b)]. Closed-loop alignment was successful despite an increase in diffraction losses due to the cumulative phase errors of the eight diffraction gratings. For comparison, a single TGA, in Littrow configuration, was alternately adjusted to form either a split focal spot [Fig. 100.28(c)] or a diffraction-limited focal spot [Fig. 100.28(d)].

Monochromatic laser light, operating at the center wavelength of a typical high-intensity laser, was used to simulate in-series alignment of the TGA units for the outer spectral components of broadband laser light. Figure 100.29(a) shows an experimentally generated phase map with the left and right regions of the beam accurately tiled, even though the individual TGA's are not properly tiled. Due to a spatial chirp that forms in part of the compressor, the extreme spectral components of the laser pulse cannot be fully compensated. The central, narrow region of the beam is not compensated and contained a differential tip of about three waves. The focal spot [Fig. 100.29(b)] shows a corresponding increase in diffraction

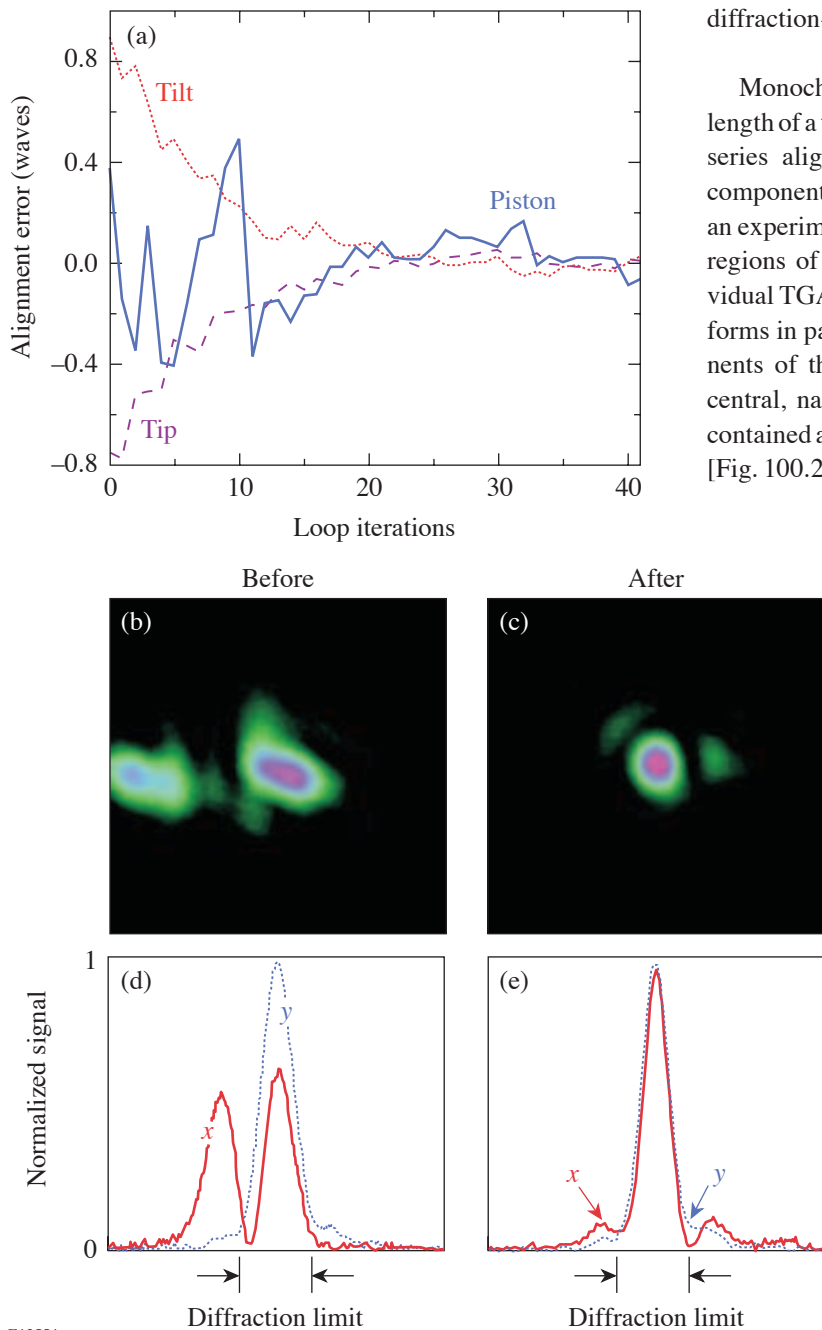


Figure 100.27
Closed-loop control of the TGA is achieved when all of the measured differential phase errors converge to zero following random offsets of the actuators (a). Corroboration between phase convergence and Strehl ratio indicates successful closed-loop control. A symmetrically split far-field pattern is observed for piston values of $(2N+1)\pi$ (b), while a single focal spot is observed for piston values of 0 and $2\pi n$ (c). The irradiance is doubled after successful alignment [(d) and (e)].

E13554

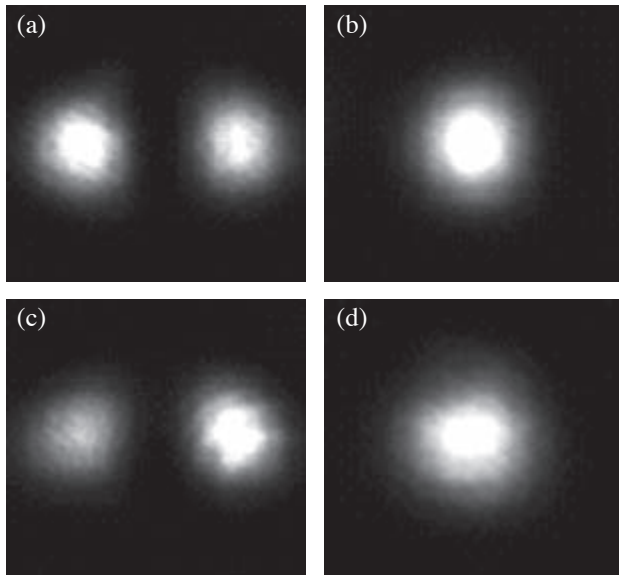
spreading in the horizontal plane due to the misregistration of the gaps. Diffraction spreading in the vertical plane is due to the differential tip of the central strip of light.

Theoretical calculations predict that integration over all spectral components of the laser pulse, carried through a TGC that is aligned with compensating TGA errors, yields negligible effects for pulses longer [Figs. 100.30(a) and 100.30(b)] than the Fourier-transform-limited ($\Delta\tau$) pulse [Fig. 100.30(c)]. Two-dimensional, space-time images clearly show that the effects from residual compensation error are pronounced only when maximum pulse compression is attempted. Further spatial integration of these images yields temporal pulses shapes [Fig. 100.30(d)] that show the small effect from a compen-

sated π piston error in a pair of TGA units. Further modeling will be carried out to explore the combined effects of differential tip, tilt, and piston differential errors when in-series alignment is deployed.

Conclusion

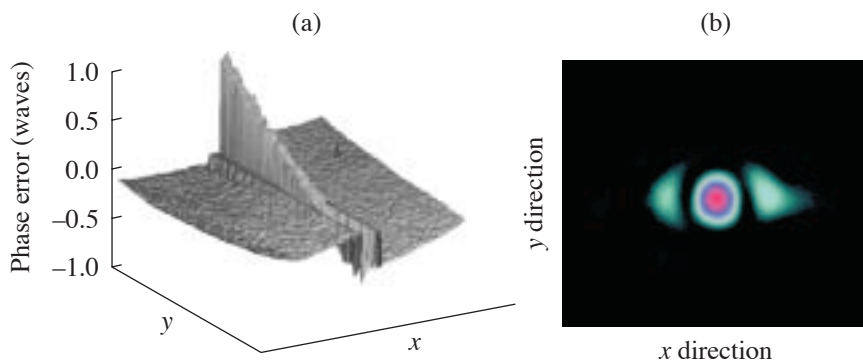
Accurate closed-loop control of a tiled-grating assembly has been achieved over extended periods of time. Together with previous demonstrations involving coherent addition and pulse compression, this result further supports the feasibility of the tiled-grating compressor as the means to obtain multi-kilojoule-energy capability for petawatt-class lasers. In addition, in-series TGA alignment was successfully demonstrated in a compressor configuration.



E13555

Figure 100.28

Operational ease can be achieved for closed-loop control of a tiled-grating compressor (TGC) through simultaneous alignment of all TGA's in series configuration. Series alignment was demonstrated by positioning two TGA's in double-pass configuration using an auxiliary retroreflecting mirror. While one TGA was intentionally misaligned with a piston error of π radians (a), the second TGA was adjusted to remove all piston error from the series configuration (b). Closed-loop alignment was successful despite an increase in diffraction losses due to the cumulative phase errors of the eight diffraction gratings. For comparison, a single TGA, in Littrow configuration, was alternately adjusted to form either a split focal spot (c) or a diffraction-limited focal spot (d).



E13556

Figure 100.29

Monochromatic laser light was used to simulate in-series alignment of the TGA's for the outer-spectral components of broadband laser light. An experimentally generated phase map is shown in (a) with the left and right regions of the beam accurately tiled, even though the individual TGA's are not properly tiled. The central, narrow region of the beam is not compensated and contains a differential tilt of about three waves. The focal spot (b) shows a corresponding increase in diffraction spreading.

Further developments of the tiled-grating compressor are required to support the OMEGA EP project. A TMA with three tiled gratings is being constructed and tested to demonstrate full-aperture mounting, positioning, and closed-loop control. In addition, this prototype test apparatus will be outfitted with three full-aperture, MLD gratings to demonstrate phase-pair compensation and closed-loop control. Major emphasis will be placed on determining the minimum beam size required to accurately align a TGA containing three gratings using both near-field phase and far-field irradiance diagnostics.

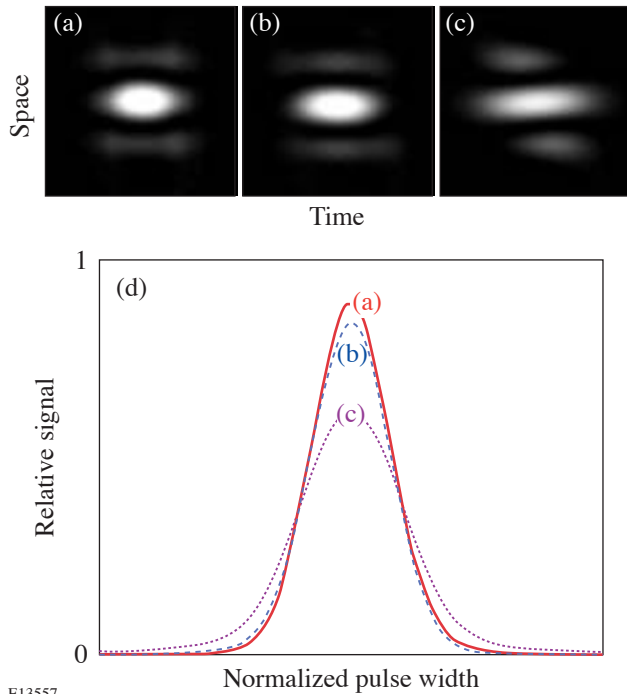


Figure 100.30
Theoretical calculations predict that integration over all spectral components of the laser pulse, carried through a TGC that is aligned with compensating TGA errors, yields negligible effects for pulses longer [(a) and (b)] than the Fourier-transform-limited ($\Delta\tau$) pulse (c). Two-dimensional, space-time images clearly show that the effects from residual compensation error are pronounced only when maximum pulse compression is attempted. Spatial integration of these images yields temporal pulse shapes (d) that show a relatively small effect.

ACKNOWLEDGMENT

This work was supported by the U.S. Department of Energy Office of Inertial Confinement Fusion under Cooperative Agreement No. DE-FC52-92SF19460, the University of Rochester, and the New York State Energy Research and Development Authority. The support of DOE does not constitute an endorsement by DOE of the views expressed in this article.

REFERENCES

1. T. J. Kessler, J. Bunkenburg, H. Huang, A. Kozlov, and D. D. Meyerhofer, *Opt. Lett.* **29**, 635 (2004).
2. Laboratory for Laser Energetics LLE Review **96**, 207, NTIS document No. DOE/SF/19460-509 (2003). Copies may be obtained from the National Technical Information Service, Springfield, VA 22161.
3. B. W. Shore *et al.*, *J. Opt. Soc. Am. A* **14**, 1124 (1997).
4. 2003 MLD Bulletin, Jobin Yvon, Inc., Gratings and OEM Division, Edison, NJ 08820-3012 (2003).
5. T. J. Kessler, J. Bunkenburg, and H. Huang, "Grating Array Systems for the Alignment and Control of the Spatial and Temporal Characteristics of Light," U.S. Patent Application (filed May 2003).
6. M. Born and E. Wolf, *Principles of Optics: Electromagnetic Theory of Propagation, Interference and Diffraction of Light*, 5th ed. (Pergamon Press, Oxford, 1975).
7. J. Bunkenburg, T. J. Kessler, H. Hu, C. Kellogg, and C. Kelly, presented at CLEO 2003, Baltimore, MD, 1–6 June 2003.
8. New Focus, Inc., a division of Brookham, <http://www.newfocus.com> (2004).
9. M. Takeda, H. Ina, and S. Kobayashi, *J. Opt. Soc. Am.* **72**, 156 (1982).
10. National Instruments, Austin, TX 78759-3504, <http://www.ni.com> (2004).
11. Oberon Microsystems, BlackBox Component Builder, available free of charge from <http://www.oberon.ch/blackbox.html> (2004).
12. R. Campbell, Engineering and Scientific Library for BlackBox Component Builder, available free of charge from <http://www.zinnamturm.de/#Chill> (2004).

In-Situ Measurements of High-Intensity Laser Beams on OMEGA

Introduction

Laser-driven, direct-drive inertial confinement fusion requires near-uniform illumination of the spherical fuel-bearing target;^{1,2} therefore, the target must be illuminated symmetrically since uneven illumination will result in uneven acceleration disrupting the implosion. For a laser-driven system with uniformly distributed beams, this dictates that all beams must have equal energies, must have the proper profile, and must be positioned accurately.

Currently, the primary method for determining the energies of beams on the OMEGA laser is based on a calorimeter system [harmonic energy diagnostic (HED)]. The beams must then be transported to the target chamber: they first pass through distributed polarization rotators (DPR's)³ and are then reflected off two mirrors and transmitted by a distributed phase plate (DPP),⁴ a focusing lens, and a vacuum window interface. Losses due to this transport are inferred from measurements made with a cw laser, but variations due to nonlinear effects at high power and variations of the beam shape are not otherwise measured. Likewise, the beam position is determined by a co-propagated cw laser, but with unknown positioning error (centroid determination of the reflected cw beam is accurate to 20 μm). With the method described here, relative beam fluence, shapes, and positions of the beams are determined from x-ray images of the emission from a 4-mm-diam, Au-coated spherical target illuminated by the beams of OMEGA.⁵ The UV light is converted to x rays in the Au coating with high efficiency,⁶ and the resultant x-ray flux is imaged with x-ray pinhole cameras (XPHC's) and recorded by charge-injection devices (CID's).⁷

This analysis takes into account projection effects, conversion from UV to x rays, and detection efficiency. This process is sufficiently automated to allow for analysis to be completed within the OMEGA minimum shot cycle (45 min). Mispositioned beams can be repointed to an accuracy of 9 μm (rms over 60 beams) again within a shot cycle. This method has also been used to determine and minimize beam-to-beam peak fluence

variations, thereby further improving on-target uniformity (enhanced fluence balance).⁸

On-Target Beam Measurements

The data present in XPHC images of pointing shots must be extracted and quantified. Ideally, the beams incident on the target are circularly symmetric and have a radial profile given by a "super-Gaussian" of the form

$$I_{\text{UV}}(r) = I_{\text{UV}}(0) \times e^{-(r/r_0)^\eta}, \quad (1)$$

where $I_{\text{UV}}(r)$ is the intensity of the beam as a function of radius, $I_{\text{UV}}(0)$ is the peak intensity, r is the distance from the beam center, r_0 is the beam-spot radius, and η is the power of the super-Gaussian.

The gold target converts the incident UV energy into x rays with a high efficiency.⁶ The result follows the proportionality⁸

$$I_x \propto I_{\text{UV}}^\gamma, \quad (2)$$

where I_x is the intensity of x rays produced by the target and γ is a constant. For the detectors used in this work,⁷ and a total filtration of 152 μm of Be, γ was estimated to be 3.7. X rays from the target are then imaged by XPHC's and recorded by CID cameras.

In general, the beams are not perfectly circular; therefore, they are fitted to an elliptical super-Gaussian. Combining Eqs. (1) and (2) and introducing an elliptical beam shape yields

$$I_x(r) = I_{\text{UV}}^\gamma(0) \times e^{-\gamma \left[(x'/a)^2 + (y'/b)^2 \right]^{\eta/2}}, \quad (3)$$

where a and b are the lengths of the major and minor axes of the ellipse, respectively. The values x' and y' are the coordinates

lying along the major and minor axes of the ellipse, given by

$$\begin{aligned} x' &= (x - x_c)\cos(\alpha) + (y - y_c)\sin(\alpha), \\ y' &= -(x - x_c)\sin(\alpha) + (y - y_c)\cos(\alpha), \end{aligned} \tag{4}$$

where x and y are the coordinates in the camera image, α is the phase angle of the ellipse, and x_c and y_c are the locations of the center of the beam in image coordinates.

The x-ray fluence measured by the CID cameras is then fit to Eq. (3), yielding values for the beam’s peak UV intensity, center position, super-Gaussian power, major and minor axes, and phase angle of the ellipse. Figure 100.31 shows a comparison of this fit to an actual XPHC image recorded by a CID

camera. The lineouts in Fig. 100.31(c) show an example comparison between measured and fit beam profiles.

1. Correction for Limb Brightening

As shown schematically in Fig. 100.32, x-ray emission from the Au plasma resulting from absorption of the UV beams is, in general, seen at an angle θ . If the emission comes from an optically thin medium, the increased path through the plasma will increase the observed x-ray fluence. It has been shown⁸ that when the plasma is uniform on the surface of the sphere, the intensity seen at an angle θ to the normal is given by

$$\begin{aligned} I_x(\theta) &= I_x(0)(r_{\text{emis}}/\Delta r) \\ &\times \left[\sqrt{1 + (\Delta r/r_{\text{emis}})^2 - \sin^2 \theta} - \cos \theta \right], \end{aligned} \tag{5}$$

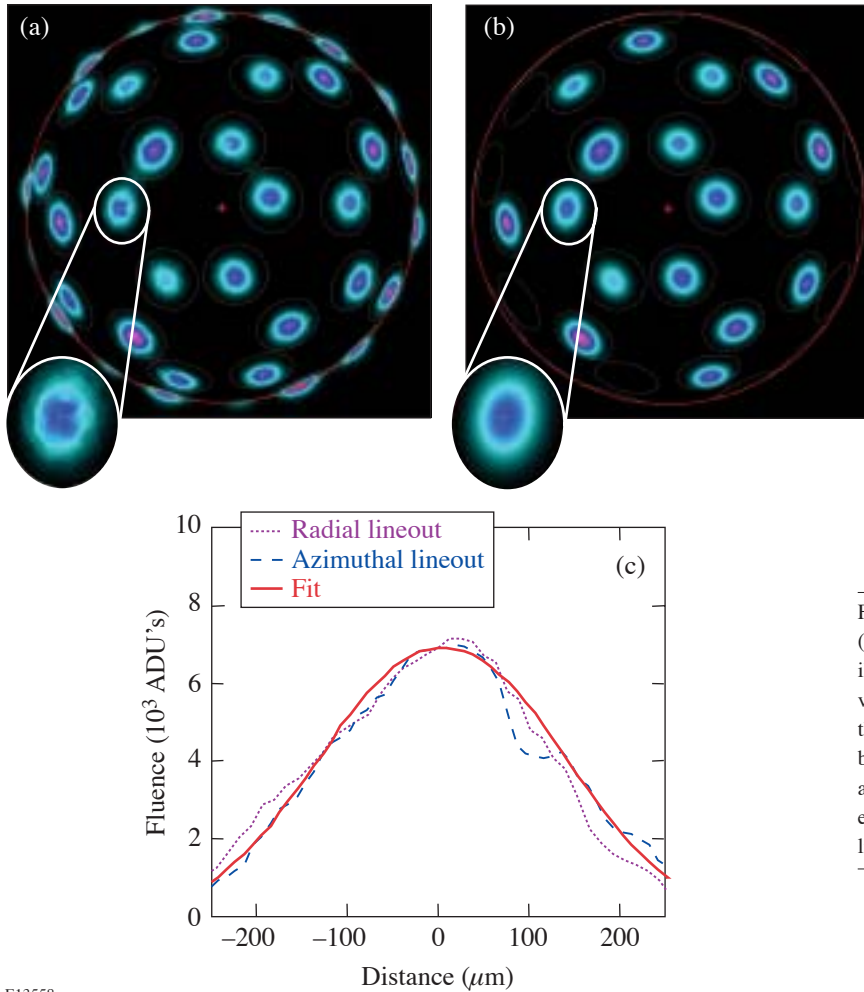


Figure 100.31
 (a) CID image of a 4-mm-diam, Au-coated pointing sphere illuminated by all 60 OMEGA beams with an enlarged view of beams 6 to 8. (b) The fit to this image created by the method described herein with an enlarged view of beams 6 to 8. Beams greater than 64° from the view center are not fit since they are greatly distorted by view-angle effects. (c) Radial and azimuthal lineouts compared to a lineout of the fit for beams 6 to 8.

E13558

where r_{emis} is the radius of the target and Δr is the thickness of the plasma. A typical value of $\Delta r = 113 \mu\text{m}$ was found on a uniformly irradiated, 1-mm-diam, Au-coated sphere with all other conditions the same as on a beam pointing shot (e.g., 1-ns square pulse at $\sim 10^{14} \text{W/cm}^2$). Correction for limb brightening on the pointing target is then accomplished by solving Eq. (5) for the value of $I_x(0)$, the intensity as seen from the normal to the target, using the values $\Delta r = 113 \mu\text{m}$ and $r_0 = 2 \text{mm}$. Since this correction is performed continuously for the entire x-ray image, the result is to approximately remove the effect of the curved surface on the measurements of beam fluence and beam position.

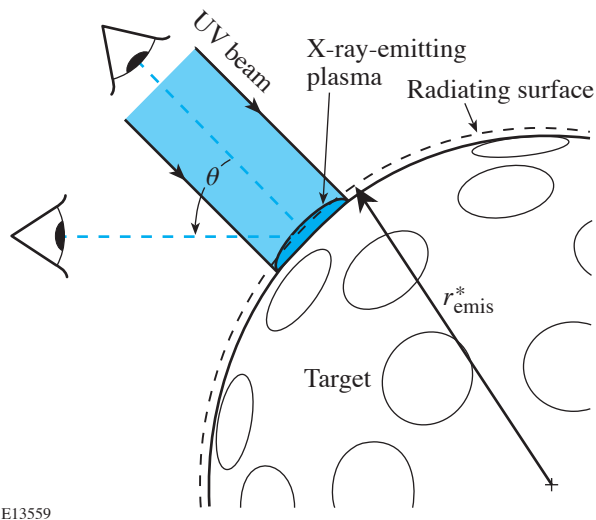


Figure 100.32

An OMEGA beam incident on a 4-mm-diam, Au-coated pointing target. The target will re-emit in the x-ray band with intensity and shape modified by conversion to x rays. However, since the beam is viewed by a camera off axis from the path of the beam, it appears to be distorted and to have a higher peak intensity than if it were viewed on axis, due to the limb-brightening effect. This also causes the apparent position of the beam on the radiating surface to be shifted from its actual position.

2. Determination of Beam Parameters

First, the images are fitted to a template of ideal beam positions (orthographic projections of beam-arrival directions), assuming the emission comes from the surface of a sphere [effective emission radius r_{emis}^* ; see Fig. (100.32)]. The best fit of this template to the observed beam positions then determines r_{emis}^* the target position and the orientation of the image with respect to target chamber coordinates (rotation angle).

After initial determination of the target position, radius, and image rotation angle, corrections for view angle are applied,

contributions from surrounding beams are removed, and the beam shape and position are recomputed. Typically this procedure is applied to images from a set of eight XPHC's located at the positions shown in Fig. 100.33. For each image, beams within 64° of the center position are analyzed. Therefore, all beams are viewed by two or more cameras, and error on beam position may be calculated by comparing determinations from multiple views. Application of the procedure described above gives improved results, as evidenced by a reduction of this error.

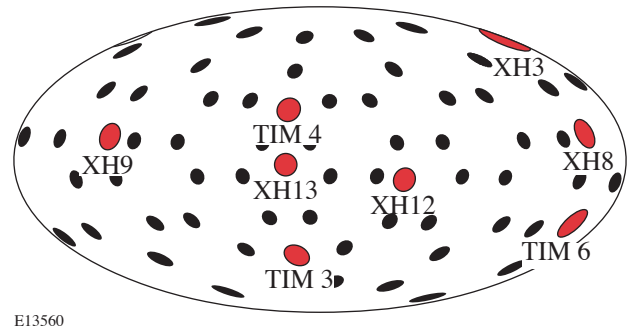


Figure 100.33

Aitoff projection plot of XPHC positions. The black circles represent beam positions. The red circles show the center position of each XPHC view, labeled with the viewport name.

After correction for projection effects, beam parameters may be measured with a high degree of accuracy. For any single SG3 beam on OMEGA, the radius may be determined to within 4%, ellipticity to within 4%, super-Gaussian power to within 4%, and peak fluence to within 4%. For a single SG4 beam, the radius may be determined to within 3%, ellipticity to within 2%, super-Gaussian power to within 6%, and peak fluence to within 4%. Differences between measurement accuracies for SG3 and SG4 beams are due to departures from the ideal beam shape.

This method has been used to determine the beam size, peak fluence variations, and pointing accuracy for the full 60 OMEGA beams when the beams are smoothed by 1-THz smoothing by spectral dispersion (SSD) with polarization smoothing (PS),⁹ both with the original DPP's (SG3) and with an expanded, flatter beam shape resulting from a new set of DPP's (SG4).¹⁰ The average beam shapes found from this analysis are $\eta = 2.27 \pm 0.02$ and $r_0 = 308 \pm 1 \mu\text{m}$ with ellipticity of 1.072 ± 0.005 for the SG3 beams, and $\eta = 3.66 \pm 0.03$ and $r_0 = 380 \pm 1 \mu\text{m}$ with ellipticity of 1.066 ± 0.003 for the SG4 beams. These

correspond to beam diameters of approximately $930\ \mu\text{m}$ and $865\ \mu\text{m}$ (diameter containing 95% of the energy) for the SG3 and SG4 DPP's, respectively.

3. Beam Repointing

Beam-position deviations from the desired template are determined from the final fits. The measured beam offsets are used to compute movements of the final turning mirrors, thereby correcting the pointing. Figure 100.34 shows the results of beam offset determinations before and after repointing (second pointing shot). The root-mean-square position error has been reduced from $23\ \mu\text{m}$ to $11\ \mu\text{m}$. This beam-repointing method has been applied many times, and the minimum rms position error achieved is $9\ \mu\text{m}$.

Conclusions

A method has been developed to accurately measure beam position, shape, and relative intensity from CID-recorded x-ray images of 4-mm-diam, Au-coated pointing targets irradiated with focused beams from the OMEGA laser. By taking into account projection effects, conversion from UV to x rays, and detection efficiency, this method is able to determine beam

position to within $7\ \mu\text{m}$, beam radius to within 3%, ellipticity to within 2%, and relative intensity to within 4%.

Accurate characterization of beams is necessary to optimize the uniformity of target illumination since displacements from ideal beam positions and variations in beam shape and intensity cannot be minimized unless they are first measured. This analysis is currently being used on OMEGA to improve the uniformity of target illumination by improving beam pointing.

ACKNOWLEDGMENT

This work was supported by the U.S. Department of Energy Office of Inertial Confinement Fusion under Cooperative Agreement No. DE-FC52-92SF19460, the University of Rochester, and the New York State Energy Research and Development Authority. The support of DOE does not constitute an endorsement by DOE of the views expressed in this article.

REFERENCES

1. J. Nuckolls *et al.*, *Nature* **239**, 139 (1972).
2. J. J. Duderstadt and G. A. Moses, *Inertial Confinement Fusion* (Wiley, New York, 1982), Chap. 1, pp. 7–8.

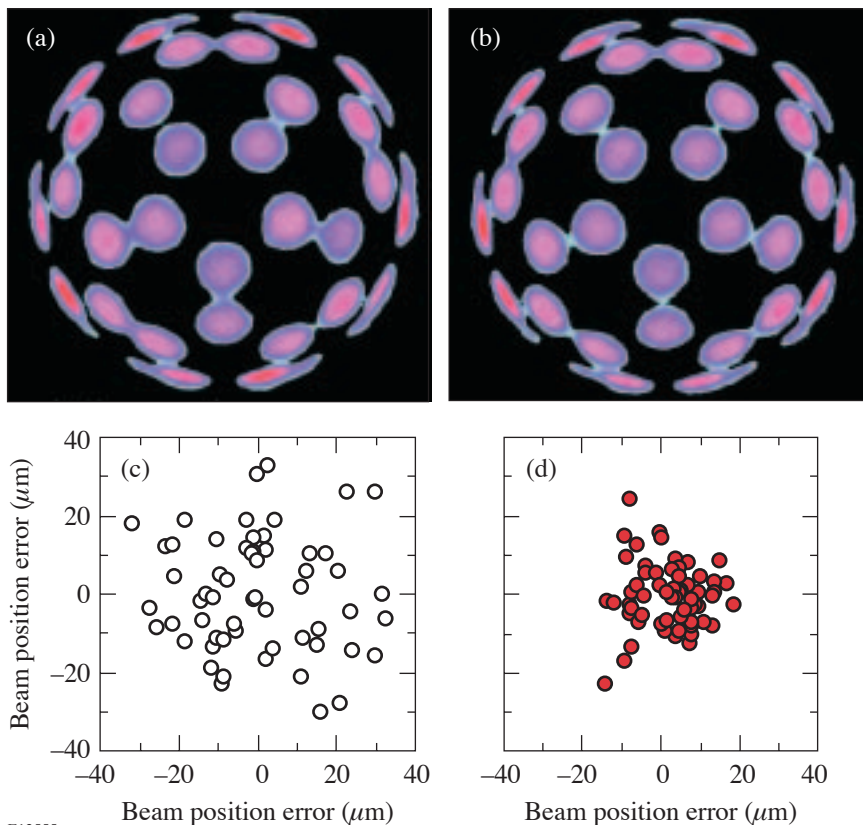


Figure 100.34

Result of repointing the OMEGA beams using the method described in this article. (a) XPHC image from the TIM 6 view showing beams before repointing. (b) XPHC image from the same view showing beams after repointing. Beam positions are visibly improved. (c) A plot of beam offsets from their ideal position before repointing. The root-mean-square offset is $23\ \mu\text{m}$. (d) A plot of beam offsets after repointing. The root-mean-square offset is reduced to $11\ \mu\text{m}$.

E12555

3. Laboratory for Laser Energetics LLE Review **45**, 1, NTIS document No. DOE/DP40200-149 (1990). Copies may be obtained from the National Technical Information Service, Springfield, VA 22161.
4. T. J. Kessler, Y. Lin, L. S. Iwan, W. P. Castle, C. Kellogg, J. Barone, E. Kowaluk, A. W. Schmid, K. L. Marshall, D. J. Smith, A. L. Rigatti, J. Warner, and A. R. Staley, in *Second Annual International Conference on Solid State Lasers for Application to Inertial Confinement Fusion*, edited by M. L. André (SPIE, Bellingham, WA, 1997), Vol. 3047, pp. 272–281.
5. J. M. Soures, R. L. McCrory, C. P. Verdon, A. Babushkin, R. E. Bahr, T. R. Boehly, R. Boni, D. K. Bradley, D. L. Brown, R. S. Craxton, J. A. Delettrez, W. R. Donaldson, R. Epstein, P. A. Jaanimagi, S. D. Jacobs, K. Kearney, R. L. Keck, J. H. Kelly, T. J. Kessler, R. L. Kremens, J. P. Knauer, S. A. Kumpan, S. A. Letzring, D. J. Lonobile, S. J. Loucks, L. D. Lund, F. J. Marshall, P. W. McKenty, D. D. Meyerhofer, S. F. B. Morse, A. Okishev, S. Papernov, G. Pien, W. Seka, R. Short, M. J. Shoup III, M. Skeldon, S. Skupsky, A. W. Schmid, D. J. Smith, S. Swales, M. Wittman, and B. Yaakobi, *Phys. Plasmas* **3**, 2108 (1996).
6. P. D. Goldstone, J. A. Cobble, A. Hauer, G. Stradling, W. C. Mead, S. R. Goldman, S. Coggeshall, M. C. Richardson, P. A. Jaanimagi, O. Barnouin, R. Marjoribanks, B. Yaakobi, F. J. Marshall, P. Audebert, and J. Knauer, in *X Rays from Laser Plasmas*, edited by M. C. Richardson (SPIE, Bellingham, WA, 1987), Vol. 831, pp. 54–61.
7. F. J. Marshall, T. Ohki, D. McInnis, Z. Ninkov, and J. Carbone, *Rev. Sci. Instrum.* **72**, 713 (2001).
8. F. J. Marshall, J. A. Delettrez, R. Epstein, R. Forties, R. L. Keck, J. H. Kelly, P. W. McKenty, S. P. Regan, and L. J. Waxer, *Phys. Plasmas* **11**, 251 (2004).
9. D. D. Meyerhofer, J. A. Delettrez, R. Epstein, V. Yu. Glebov, V. N. Goncharov, R. L. Keck, R. L. McCrory, P. W. McKenty, F. J. Marshall, P. B. Radha, S. P. Regan, S. Roberts, W. Seka, S. Skupsky, V. A. Smalyuk, C. Sorce, C. Stoeckl, J. M. Soures, R. P. J. Town, B. Yaakobi, J. D. Zuegel, J. Frenje, C. K. Li, R. D. Petrasso, D. G. Hicks, F. H. Séguin, K. Fletcher, S. Padalino, M. R. Freeman, N. Izumi, R. Lerche, T. W. Phillips, and T. C. Sangster, *Phys. Plasmas* **8**, 2251 (2001).
10. F. J. Marshall, J. A. Delettrez, R. Epstein, R. Forties, V. Yu. Glebov, J. H. Kelly, T. J. Kessler, J. P. Knauer, P. W. McKenty, S. P. Regan, V. A. Smalyuk, C. Stoeckl, J. A. Frenje, C. K. Li, R. D. Petrasso, and F. H. Séguin, *Bull. Am. Phys. Soc.* **48**, 56 (2003).

Chemical Durability of Phosphate Laser Glasses Polished with Pitch, Pads, or MRF

Introduction

Large, high-power laser systems are currently under construction; such systems include the National Ignition Facility (NIF) at Lawrence Livermore National Laboratory (LLNL),¹ the LMJ laser at CEA in France, and the OMEGA EP at LLE.² These new lasers will require large amounts of neodymium phosphate laser glass, which is known to be sensitive to water.³ When improperly handled or exposed to too much humidity, phosphate glass surfaces may cloud—a result of increased surface roughness due to chemical reactions. Smooth surfaces are required for such lasers (for example, a 2- to 10-Å-rms roughness level is specified for the NIF¹); rougher surfaces cause scatter, which can result in intensity modulation in the laser beam, leading to damage to downstream optics and “(increased) fluence on the spatial-filter pinholes.”¹ Transmission loss also causes output energy loss, significantly reducing performance. Thus the chemical durability of the laser glass used is of great importance to its fabrication, storage, cleaning, and handling.

Cast Hoya LHG8 phosphate glass, which is made in small individual batches, has been handled and used for over 25 years at LLE in the OMEGA laser system. It was found that a 50/50 glycol and water mixture was required to cool the fine-ground barrels of laser rods without erosion of the LHG8 composition,^{3,4} but no other chemical durability problems with the polished faces of cast LHG8 rods and disks were encountered. The new lasers will use phosphate glass manufactured by a continuous melting process⁵ developed by LLNL for the NIF laser. In addition to the LHG8 composition used in OMEGA, a new phosphate glass composition, Schott LG770, will be used in the NIF. Changes in manufacturing technique and composition may affect chemical durability.

Previous work at LLNL⁶ has shown the continuously melted LG770 to be less resistant to attack by water than the continuously melted LHG8. The quality of the surface finish (between grinding, inspection polishing, and optical finishing) was found to affect dramatically the rate at which the glasses weathered. Both compositions were shown to be sensitive to

residual abrasives when they were allowed to dry on the surface after polishing,⁶ which is a known effect on surfaces of low-durability glass.⁷ The limited use of scrubbing with aqueous detergent solutions was specified for removing protective coating residues from phosphate glass surfaces after storage.⁸

After finishing, three practical issues for preserving the surface quality of phosphate glass are handling, storage, and sensitivity to cleaning. This work focused on determining how resistant each composition was to various levels of humidity; whether or not the manufacturing method (casting versus continuous melting) affected humidity resistance; what effect the surface-finishing process had on resistance to humidity or response to cleaning; the effect of periodic, gentle wiping during storage; and the effect of aggressive aqueous cleaning (of the sort typically used before installing optics into laser systems) on both “good” surfaces and degraded ones.

Experimental Design

The following subsections summarize our general experimental design. Samples of each glass type were processed using three different finishing techniques: pitch polishing, pad polishing, or magnetorheological finishing (MRF). Samples were stored in chambers at four different controlled humidities at 22°C for 14 weeks. Half of the samples underwent a gentle weekly wiping during storage. A total of 48 samples with 80 prepared surfaces were monitored. The distribution of the samples is given in Fig. 100.35, where sample ID's are listed in bold and sides prepared with different polishing protocols are labeled as S1 and S2. For example, sample 13C denotes a continuously melted LG770 part intended for storage at 38% RH (relative humidity) that has undergone the gentle weekly wiping. Surface S1 of the part had been pitch polished, while surface S2 had been pad polished. Samples used to illustrate trends discussed extensively in this article are highlighted in Fig. 100.35 in gray. Surface microroughness analyses and power spectral density analyses were performed, and the visual appearance of each sample was monitored. After 14 weeks, samples stored in high humidity underwent a thorough visual and microscopic inspection before undergoing two aqueous

cleanings by technicians in the optics manufacturing facility at LLE. Some of these high-humidity samples were cleaned with water alone, and some with water and detergent. After each cleaning, these samples were measured and inspected again.

1. Sample Preparation

Testing was performed on identically processed, handled, and stored samples of cast LHG8 (designated C-LHG8), continuously melted LHG8 (designated CM-LHG8), and continuously melted LG770 (designated CM-LG770). Samples were nominally 25 mm × 25 mm × 5 mm. The samples of C-LHG8 came from in-house stock, and the samples of CM-LHG8 and CM-LG770 came from LLNL. Samples of C-LHG8 and CM-LHG8 underwent pitch polishing, rotational magneto-rheological finishing (MRF), and raster MRF. MRF is a finishing method that involves polishing a surface by moving it through a ribbon of a magnetic fluid that contains abrasives.⁹ Samples of CM-LG770 underwent pitch polishing, pad pol-

ishing, rotational MRF, and raster MRF. Pitch polishing was done in-house on a 36-in. continuous polishing (CP) machine, with Gugolz #82 pitch, using an aqueous slurry containing Cerox 1663 cerium oxide. Samples were cleaned with acetone after pitch polishing. Pad polishing (on CM-LG770 only) was done by an outside vendor in a double-sided process using cerium oxide and pads. These parts were used “as-received.” MRF using both rotational and raster modes of processing was done in-house on a QED Technologies Q22-Y machine using an experimental ZrO₂-based MR fluid.¹⁰ For rotational MRF, samples were polished by rotating the surfaces of the spindle-mounted parts as they were moved through the magnetic ribbon. For raster MRF, the parts were translated without rotation through the ribbon in a raster fashion. MRF was performed on previously pitch- or pad-polished surfaces, with at least 0.2 μm of material uniformly removed. After MRF, samples were wiped with water, followed by acetone.

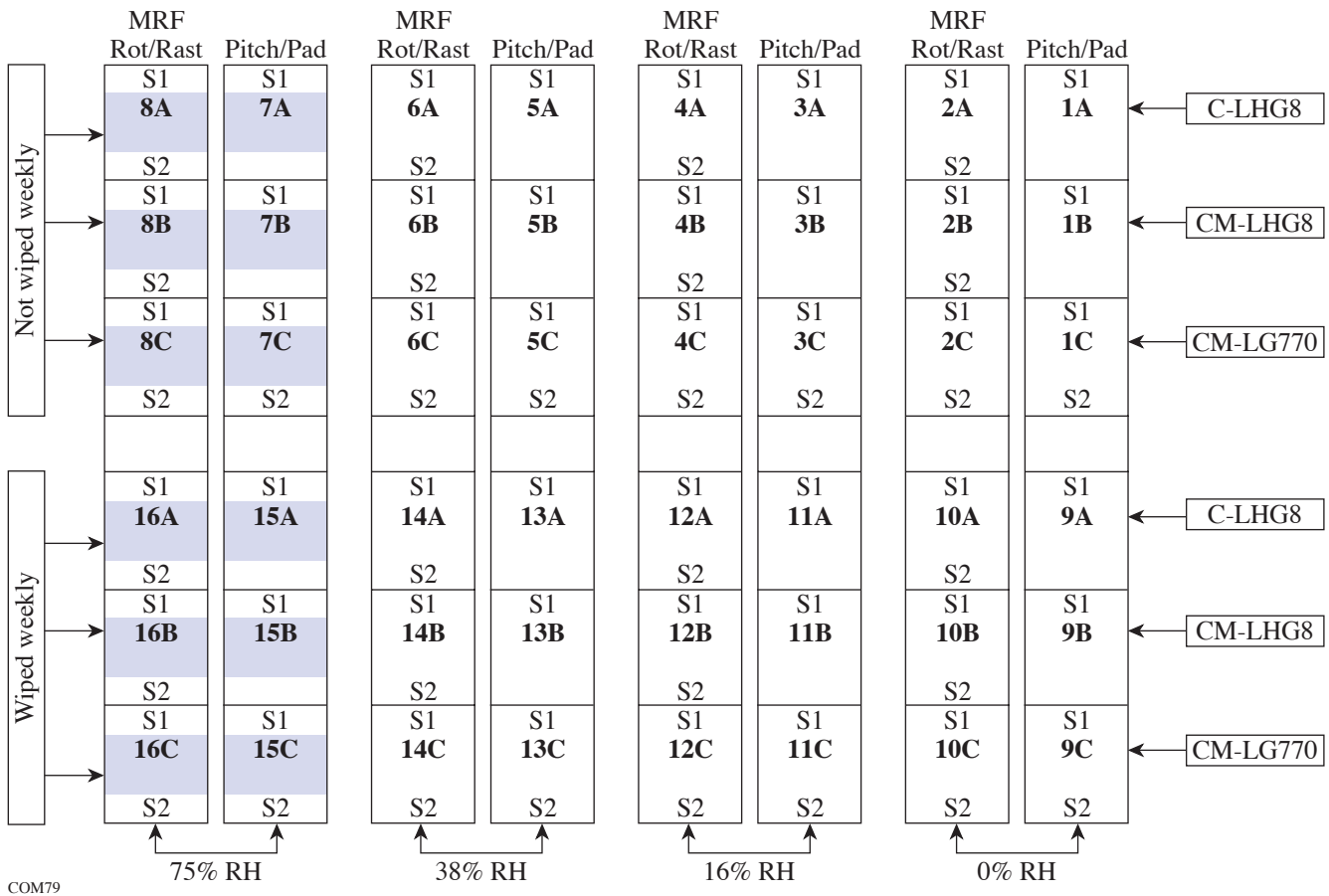


Figure 100.35
Distribution of 48 phosphate glass samples for chemical durability tests (see text).

2. Sample Handling and Storage

Four chambers were set up for the humidity testing. Each chamber maintained a static noncirculating air environment and was kept sealed except during removal and replacement of samples. Temperature in the chambers remained between 21°C and 22°C. Humidities of 0%, 16%, 38%, and 75% ($\pm 1\%$) RH were maintained in the chambers using desiccant (0% RH) and saturated aqueous solutions of LiCl, NaI, and NaCl, respectively. Temperature and humidity were monitored daily using hygrometer/thermometer pens,¹¹ which remained in the sealed chambers.

Samples were mounted upright in these humidity chambers in foam holders with the prepared surfaces exposed. They remained in the chambers for 14 weeks and were removed only for cleaning, measurement, and inspection. Samples were transported to and from the metrology lab in closed plastic boxes and were handled with nitrile gloves. During cleaning, measurement, and inspection, samples were exposed briefly to lab humidity conditions of between 20% and 60% RH, with an average of 32% RH, and temperatures between 21°C and 22°C.

3. Sample Cleaning

A gentle drag-wipe method with HPLC-grade methanol and lens tissue (Lens SX90 tissue from Berkshire) was chosen as an initial “cleaning” protocol for all surfaces. Although not a rigorous “cleaning” process, wiping was selected as being most likely to preserve the quality of initial surfaces for the ensuing humidity tests. Sample wiping consisted of a pair of orthogonally oriented drag wipes per side. Half of the samples underwent this procedure only once before being placed in the humidity chambers; these samples were designated “not weekly wiped” (NWW). The other half of the samples were wiped in this way prior to being placed in the humidity chambers and then wiped again every week for 13 weeks; these samples were designated “weekly wiped” (WW).

A true aqueous cleaning method involving gentle hand scrubbing was chosen as a more aggressive protocol, which was performed at the conclusion of testing, but only on the samples that had been stored in 75% RH. This protocol was chosen after reviewing existing procedures for cleaning laser glass surfaces.⁸ After 14 weeks of storage, half of the samples from the 75%-RH chamber were cleaned with 18-Mohm deionized (DI) water alone, and half were cleaned with DI water and detergent (Micro-90 Microsoap). Each sample was held under running DI water while being scrubbed with synthetic nylon wipes (Miracle Wipes). Detergent was added to the surfaces of some of the samples during this process. After

scrubbing, samples were rinsed in a DI water spray for 2 min and then set upright in a laminar flow hood¹² to dry. After evaluation, the samples were stored in 0% RH. After 5 additional weeks, the aqueous cleaning procedure was repeated. These cleaning methods are typical of what would be used on optics going into laser systems.

4. Surface-Evaluation Protocols

Although scatter is the main concern for laser systems, no simple, direct way to measure it on these samples was found in this facility. Four easily performed methods for surface evaluation were chosen: measurement of areal microroughness with and without electronic filtering, power spectral density (PSD) analysis, visual inspection, and microscopic inspection.

Areal microroughness measurements were made using a Zygo NewView 100 white-light interferometer, with a 5 \times Michelson objective.¹³ Areal peak-to-valley (p-v) and root-mean-square (rms) values were obtained over areas of 1.41 mm \times 1.05 mm. Measurements were made weekly on samples in the 38%- and 75%-RH chambers, and bi-weekly on samples in the 16%- and 0%-RH chambers for the first 10 weeks. Additional measurements were made on samples in the 75%-RH chamber at 13 weeks and after each aqueous cleaning with and without detergent. An average of measurements from five random sites in characteristic areas of the samples was recorded. Uncharacteristic areas, the center, and the edges of the substrates were avoided. Filtering was used on selected data to observe features in specific spatial-frequency ranges suggested by PSD analysis.

PSD analysis provided more-detailed information about what kinds of structures were contributing to the surface roughness. PSD data were gathered for selected surfaces from the New View 100¹³ and plotted using in-house MATLAB codes¹⁴ as power density (nm³) as a function of spatial frequency (1/nm). With the 5 \times Michelson objective, information was obtained for structures contributing to roughness at spatial frequencies between $\sim 1 \times 10^{-4}$ 1/nm and $\sim 4 \times 10^{-7}$ 1/nm (corresponding to periodicities between ~ 10 μ m and ~ 2.5 mm). Plotted data were compared to a typical specification for NIF laser disks.¹⁵ Various types of visual inspection were employed. General observations were routinely made with the naked eye in fluorescent room light. Inspections with a fiber-optic light source in a dark room were made after 4 and 11 weeks of storage. At 14 weeks, surfaces were inspected, mapped, and described in writing before and after the first aqueous cleaning with and without detergent. Digital photos of the samples were taken in a darkened room with a flash before

and after the first (14 weeks) and second (19 weeks) aqueous cleanings. Microscopic inspection was carried out using a Nikon research-grade, white-light optical microscope before and after the first aqueous cleaning. Surfaces were observed in reflection using both bright-field and dark-field modes with 5×, 10×, 20×, and 50× objectives.

Results of Humidity Study

Very little change was seen on the majority of the surfaces monitored. After 10 weeks of storage, *no degradation* was seen on any of the samples stored at 38% RH, 16% RH, or 0% RH. The experiment was ended for these samples. Within the 75%-RH chamber, *no degradation was seen on any of the samples that underwent the gentle weekly wiping protocol, and no degradation was seen on any of the samples of CM-LHG8 with or without wiping* throughout the 14 weeks they were stored at elevated humidity. The samples of NWW C-LHG8 in the 75%-RH chamber (samples 7A and 8A; refer to Fig. 100.35) showed minor visible degradation, accompanied by increased rms microroughness and elevated levels of PSD, which was worse on the pitch-polished surface (surface S1 of 7A) than on the MRF-polished ones (surfaces S1 of 8A and S2 of 8A). Both of the samples of NWW CM-LG770 (samples 7C and 8C) in the 75%-RH chamber showed severe degradation, confirming the high degree of humidity sensitivity for this composition.

Degradation on samples of NWW CM-LG770 (samples 7C and 8C) first appeared in the form of large structures at low spatial frequencies, increased rms microroughness, and elevated PSD levels. By 13 weeks of storage, structures had developed at higher spatial frequencies, resulting in increased rms and p-v microroughness and elevated PSD levels at high spatial frequencies. The surfaces had also developed a grainy, highly scattering appearance. Although the quality of the initial surface finish did not affect the rate of degradation in samples of NWW CM-LG770 at 75% RH, the various surface-finishing processes appeared to influence how the degradation formed, with different types of structures appearing on surfaces that had been polished differently.

The following four subsections concentrate exclusively on the results observed for selected samples of all glass compositions *stored at 75% RH and not wiped weekly*.

1. Changes in Areal Microroughness

The *initial* rms surface areal microroughness of the phosphate glass samples varied from 0.6 nm to 2.2 nm as a result of the different surface-finishing protocols. In general,

for all samples, the pad-polished surfaces were roughest, the pitch-polished surfaces were smoothest, and the MRF-processed surfaces fell somewhere in between. This did not depend on glass type. Variations in microroughness were not indicative of polishing process efficiency but were simply the result of polishing conditions available at the time. An example showing *good* environmental stability is given in Fig. 100.36 [(a) rms, (b) p-v] for NWW CM-LHG8 (samples 7B and 8B) stored at 75% RH. All initial surface microroughness values were below 1-nm rms, though differences in rms surface microroughness were seen between surfaces polished with either pitch (surface S1 of 7B) or MRF (surfaces S1 of 8B and S2 of 8B), with the pitch-polished surfaces being the smoothest. Peak-to-valley values generally overlapped and fell in a range between 10 nm and 30 nm. Microroughness levels remained unchanged after 13 weeks of storage.

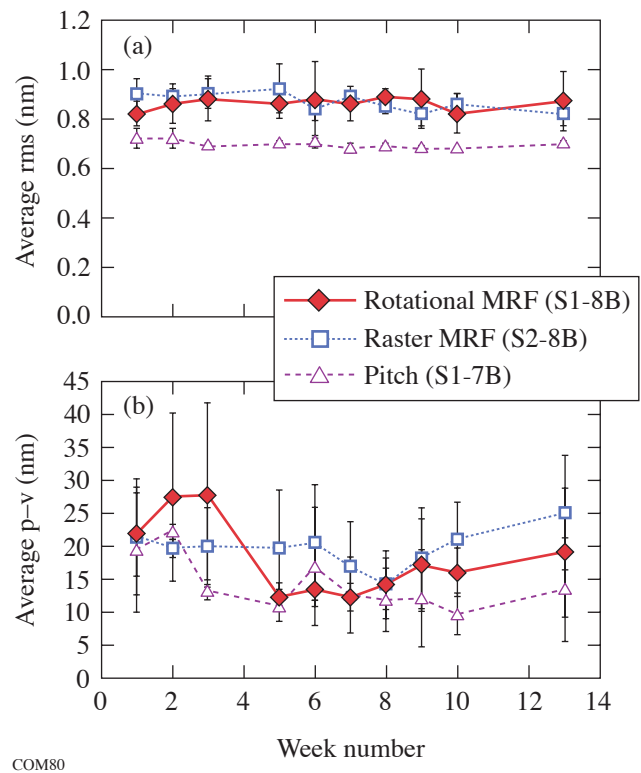


Figure 100.36

Areal microroughness of NWW CM-LHG8 (samples 7B and 8B) surfaces over 13 weeks of storage in 75% RH (lines to guide the eye). (a) Areal rms; (b) areal p-v.

An example showing *moderate* environmental stability is given in Fig. 100.37. No significant changes in either rms or p-v roughness were observed on samples of NWW C-LHG8 (samples 7A and 8A) throughout the first 8 weeks of storage at

75% RH. These samples showed increasing rms and p-v microroughness beginning at week 9 and week 10, respectively. Increases in microroughness continued through 13 weeks of storage [see Figs. 100.37(a) and 100.37(b)]. The increases were much more dramatic for the pitch-polished surface of sample 7A (rms: 3.9 nm±2.5 nm; p-v: 450 nm±370 nm) than for the two MRF-polished surfaces of sample 8A.

An example of *significant environmental instability* is given in Fig. 100.38. Both the rms and p-v roughness values of the two samples of NWW CM-LG770 (samples 7C and 8C) remained stable throughout the first 4 weeks of storage. Measurable increases in rms microroughness on all four surfaces of these samples were detected after 5 to 7 weeks of storage [see Fig. 100.38(a)]. The rms roughness continued to increase on all four surfaces of both samples of NWW CM-LG770 through

10 weeks. These increases in rms roughness were *not* accompanied by increases in p-v roughness [see Fig. 100.38(b)]. By week 13, however, both rms and p-v roughness values had increased dramatically (rms: 8 nm to 24 nm; p-v: 480 nm to 1090 nm). The standard deviations on the week-13 measurements were very large (rms: ±>4.3 nm; p-v: ±>200 nm). There was no direct correlation between the initial surface rms roughness level and rate of degradation. In fact, the pad-polished surface (surface 7C of S2), which was initially the roughest, showed the *smallest* increase in rms roughness values after 13 weeks. The raster MRF-processed surface (surface 8C of S2) showed the greatest increase in rms roughness. The magnitudes of all of the changes on the NWW CM-LG770 surfaces were much greater than those detected on surfaces of any of the LHG8 samples.

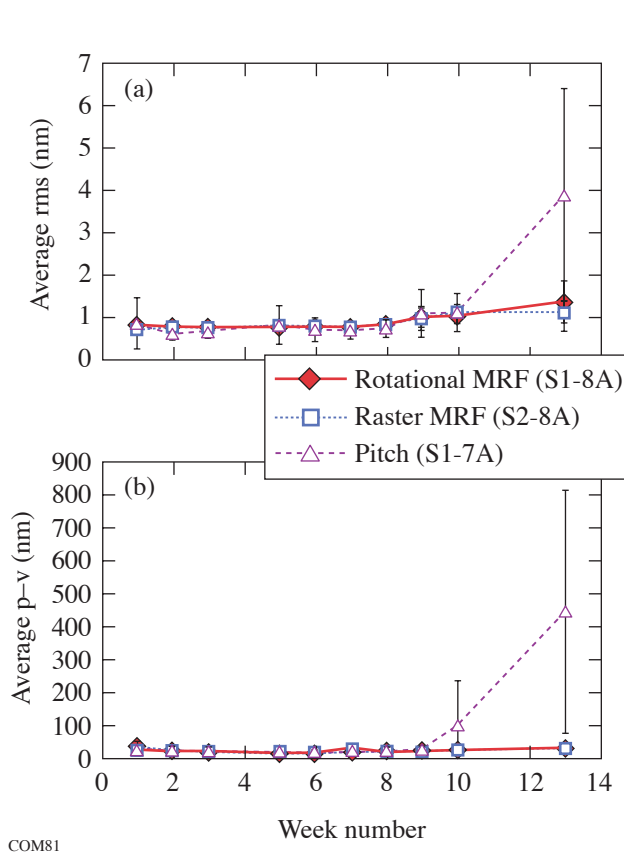


Figure 100.37
Areal microroughness of NWW C-LHG8 (samples 7A and 8A) surfaces over 13 weeks of storage in 75% RH (lines to guide the eye). (a) Areal rms; (b) areal p-v.

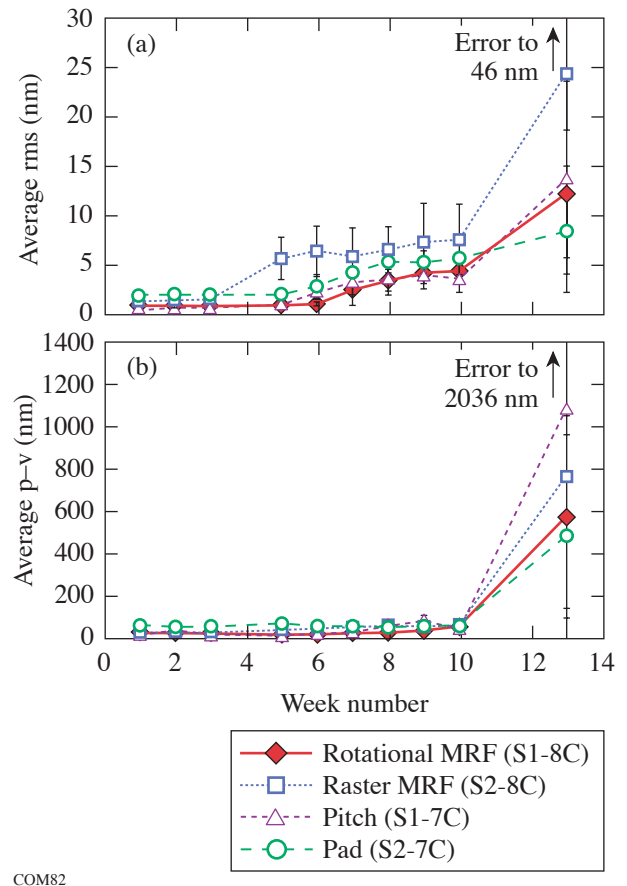


Figure 100.38
Areal microroughness of NWW CM-LG770 surfaces (samples 7C and 8C) over 13 weeks of storage in 75% RH. (a) Areal rms; (b) areal p-v.

2. Analyses of Power Spectral Density

As expected, since the area under a power spectral density (PSD) curve is proportional to the square of the rms,¹⁶ initial surface-rms-roughness differences were also reflected in PSD data. Figure 100.39 gives PSD plots for initial surfaces of NWW CM-LHG8 and NWW CM-LG770 (surfaces S1 of 7B, S2 of 7C, S1 of 8B, and S2 of 8B). The pad-polished surface of 7C had the highest power-density levels (pad-polished surfaces were the only surfaces with power-density levels above the NIF specification for laser disks¹⁵), while the pitch-polished surface of 7B had the lowest. The power-density levels of the two MRF-polished surfaces of 8B were comparable to the pitch-polished surface at high spatial frequencies and rose to levels between the pitch-polished and pad-polished surfaces at low spatial frequencies.

Figure 100.40 shows selected PSD plots for the pitch-polished surface S1 of sample 7A of NWW C-LHG8 stored in the 75%-RH chamber, which was initially well polished and below the NIF reference level. The plot shows that power density increased by two orders of magnitude over all spatial frequencies after 13 weeks of storage. The other two surfaces of NWW C-LHG8 (the rotationally MRF-processed surface S1 of 8A and the raster MRF-processed surface S2 of 8A) showed small increases in power density over 13 weeks. Figure 100.41 shows results for the rotationally MRF-processed surface only. Increases by less than 10x were observed at spatial frequencies between 10⁻⁴ 1/nm and 10⁻⁵ 1/nm (periodicities between 10 μm and 100 μm), with no changes

observed at lower spatial frequencies (longer periods). (Note: PSD data in Figs. 100.40–100.42 after aggressive aqueous cleaning are discussed in the **Aqueous Cleaning Results...** section, p. 265.)

All four surfaces of the two samples of NWW CM-LG770 (7C and 8C) showed significant increases in levels of power density between 5 weeks and 7 weeks. Figure 100.42 shows selected PSD plots for the rotationally MRF-processed surface S1 of 8C. At week 10 (not shown), power density at low spatial

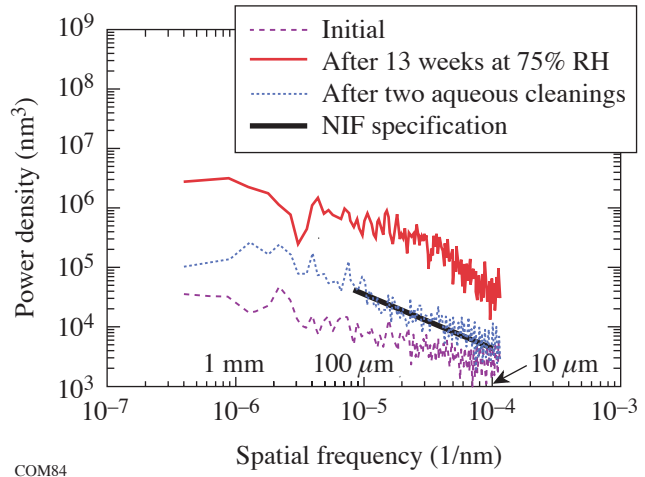


Figure 100.40 Selected PSD data for a pitch-polished surface of NWW C-LHG8 (S1 of 7A) stored in 75% RH for 13 weeks.

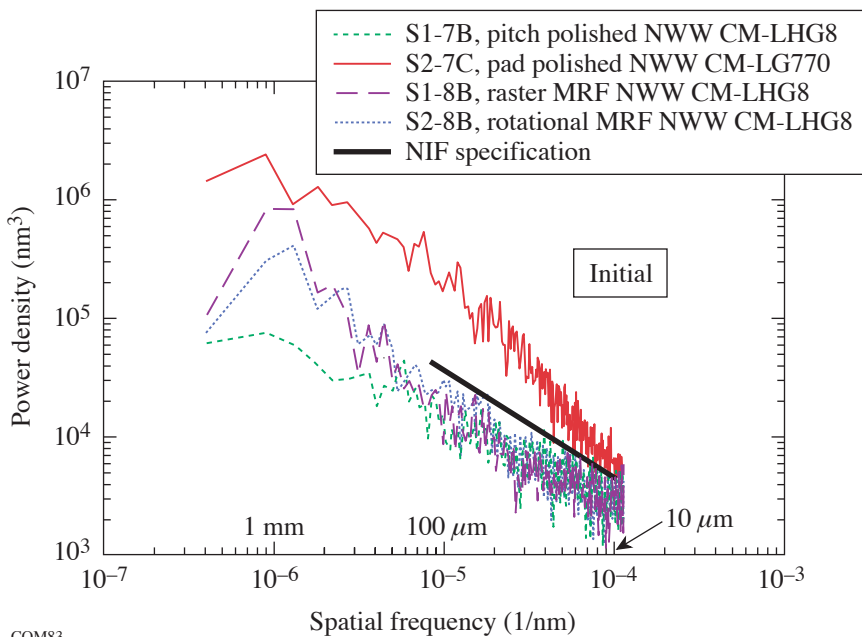


Figure 100.39 PSD plot of different initial surface finishes of NWW CM-LHG8 and NWW CM-LG770 before storage in 75% RH.

frequencies (2×10^{-6} 1/nm to 4×10^{-7} 1/nm) had increased by $\sim 15\times$, while at higher spatial frequencies the departure from the initial condition was less. By week 13, power-density levels at middle-to-high spatial frequencies had also increased significantly, with a “bump” in the data around a spatial frequency of 5×10^{-5} 1/nm (corresponding to a periodicity of $20 \mu\text{m}$; see Fig. 100.42).

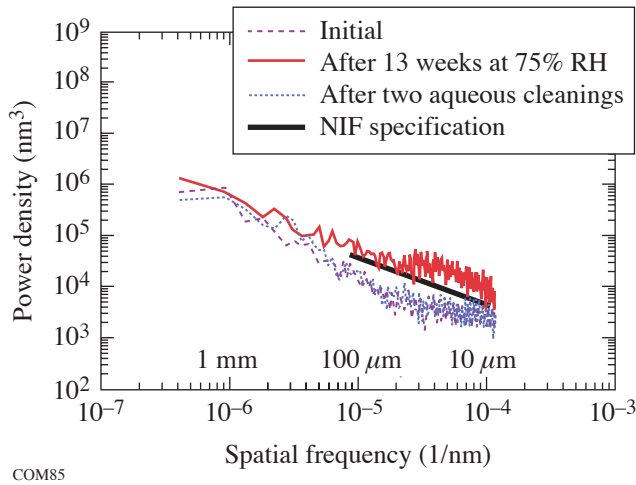


Figure 100.41 Selected PSD data for a rotationally MRF-processed surface of NWW C-LHG8 (S1 of 8A) stored in 75% RH for 13 weeks.

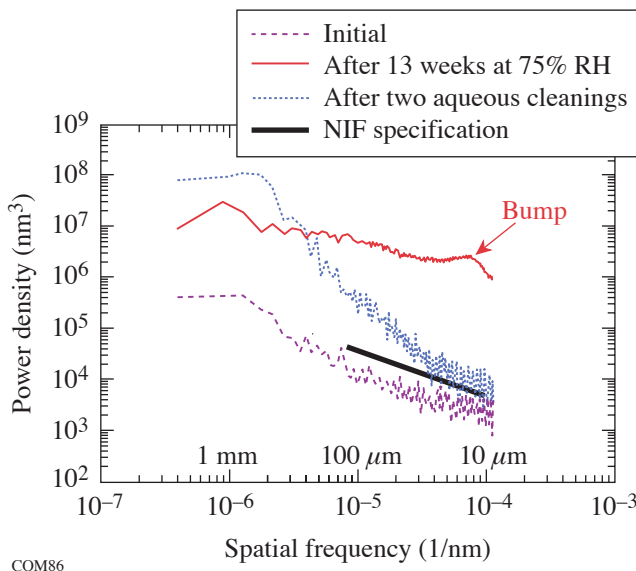


Figure 100.42 Selected PSD data for a rotationally MRF-processed surface of NWW CM-LG770 (S1 of 8C) stored in 75% RH for 13 weeks.

Rising PSD levels on S1 of 8C (see Fig. 100.42) corresponded to surface features observed with white-light interferometry. Increased power density at lower spatial frequencies correlated with large surface features that are best described as “mottling.” Figure 100.43 shows this mottling as viewed with the NewView 100 using a low-pass filter ($333 \mu\text{m}$). By week 13, small structures varying in size from $4 \mu\text{m}$ to $50 \mu\text{m}$ in diameter, as measured by optical microscopy, had also developed on the surface. The size of the larger of these structures ($>10 \mu\text{m}$) corresponds to the “bump” in the PSD plot for week 13. Structures with sizes in the middle spatial frequencies (1×10^{-5} 1/nm to 4×10^{-6} 1/nm) also appeared by week 13. Figure 100.44 shows these structures viewed on the white-light interferometer using a bandpass

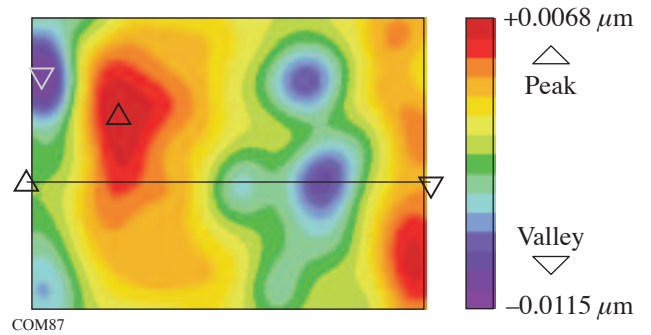


Figure 100.43 NewView 100 grayscale image of structures at low spatial frequencies on rotationally MRF-processed NWW CM-LG770 (S1 of 8C), stored in 75% RH for 13 weeks, viewed with a $333\text{-}\mu\text{m}$, low-pass filter. $1.41\text{-mm} \times 1.05\text{-mm}$ areal view. p-v: 18.4 nm ; rms: 3.44 nm .

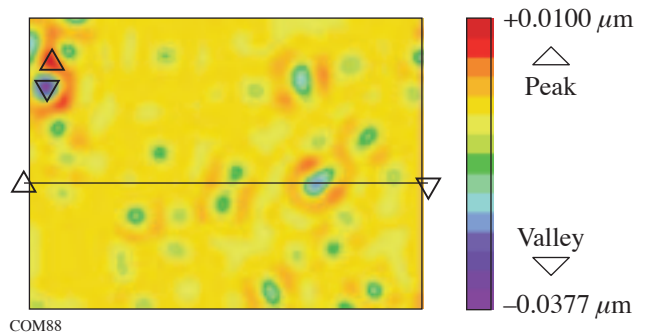


Figure 100.44 NewView 100 grayscale image of structures at middle-range spatial frequencies on rotationally MRF-processed NWW CM-LG770 (S1 of 8C), stored in 75% RH for 13 weeks, viewed with a $100\text{-to } 250\text{-}\mu\text{m}$ bandpass filter. $1.41\text{-mm} \times 1.05\text{-mm}$ areal view. p-v: 55.6 nm ; rms: 3.51 nm .

filter (100 μm to 250 μm). The increased power-density levels at middle-range spatial frequencies for week 13 (see Fig. 100.42) show that they make a significant contribution to increased rms roughness.

3. Visual Inspection

Visual inspection at 11 weeks and beyond agreed in general with more quantitative optical measurements. The presence of films, haziness, and graininess could be correlated to samples that had shown increases in microroughness and PSD levels. In some cases, visual inspection revealed differences among parts that were not measurable with metrology instrumentation, presumably because the human eye is more sensitive to scatter than the metrology instruments we used. Surfaces of some of the MRF-processed parts looked better than those of the pitch-polished and pad-polished ones, and surfaces on the samples of CM-LHG8 looked better than surfaces on the samples of C-LHG8. At the conclusion of 14 weeks of exposure, there was considerable particulate contamination and a “busy” appearance on many surfaces.

4. Microscopic Inspection

Microscopic inspection after 14 weeks of storage was useful for evaluating significantly degraded surfaces prior to aggressive cleaning and for observing structures with high spatial frequencies that developed on the surfaces. These structures varied in both size (4 μm to 50 μm in diameter) and appearance from surface to surface. We attribute these variations to the different initial finishing processes used and any residual contaminants unique to each finishing process that may have been left on each surface. The pitch-polished surface of NWW C-LHG8 (S1 of 7A) was covered in randomly distributed, nominally round features that were 8 μm to 12 μm in diameter, as seen in bright field mode using a 20 \times objective. These features are shown in Fig. 100.45(a). The pitch-polished surface of NWW CM-LG770 (S1 of 7C) was also covered in

nominally round features that were smaller (about 4 μm in diameter) than those on the NWW C-LHG8 surface. The pad-polished surface of NWW CM-LG770 (S2 of 7C) showed oblong and elevated features that were ~ 4 μm wide and 8 μm to 16 μm long. The MRF-processed surfaces of NWW CM-LG770 (S1 of 8C and S2 of 8C) had asymmetrical, elevated features between 10 μm and 40 μm in diameter that resembled snowflakes. On the rotationally MRF-processed surface (S1 of 8C), these features were isolated from other defects, as shown in Fig. 100.46. On the raster-polished surface (S2 of 8C), the snowflake-like features appeared to surround some of the numerous dark, round artifacts that covered the surface (see Fig. 100.47). This finding suggests that the dark, round artifacts are defects (possibly residual contaminant from the polishing process) that act as initiation sites for degradation, as reported in previous work.¹

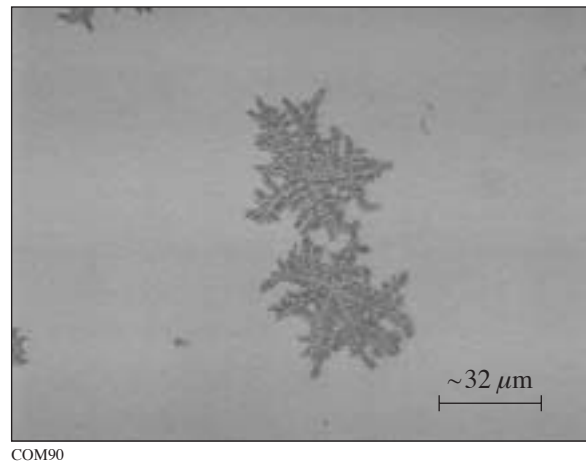


Figure 100.46
Optical microscope image of rotationally MRF-processed NWW CM-LG770 (S1 of 8C) after 14 weeks of storage at 75% RH, before cleaning, viewed in bright field at 50 \times .

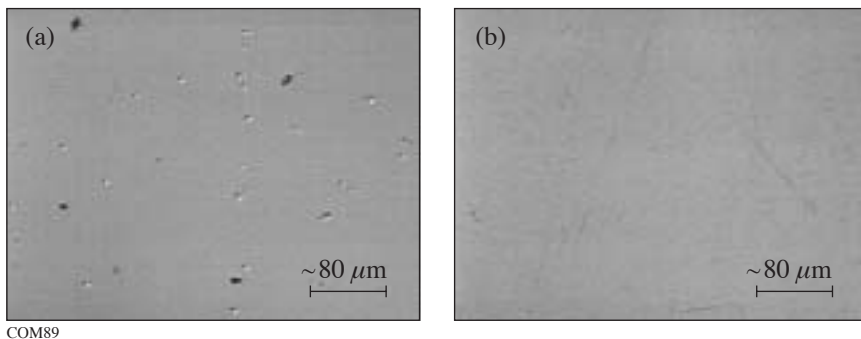


Figure 100.45
Optical microscope images of pitch-polished NWW C-LHG8 (S1 of 7A) at 14 weeks, before (a) and after (b) aqueous cleaning, viewed in bright field at 20 \times .

Aqueous Cleaning Results for All Samples Stored at 75% RH

More-aggressive cleaning protocols were employed at the conclusion of the 14-week humidity test to determine how readily degraded surfaces could be restored, to evaluate the permanence of degradation observed, and to evaluate the effects of aqueous cleaning on “good” surfaces. Because no differences were observed between the results for samples cleaned with DI water alone and those cleaned with DI water and detergent, in the following discussion we do not differentiate between the two aqueous cleaning protocols.

Initial aqueous cleaning visibly improved the appearance of all WW and NWW surfaces by removing films and particulates. All of the 4- μm to 50- μm structures observed microscopically [see Figs. 100.45(a), 100.46, and 100.47] were removed by a single cleaning. For NWW surfaces that exhibited degradation, this single cleaning removed surface structures that developed at high spatial frequencies, and it reduced the number density of surface structures that developed at middle-range spatial frequencies. It did not remove any of the low-spatial-frequency structures that developed on some surfaces.

A second aqueous cleaning did not further improve, and in some cases damaged, the surfaces. Both first and second cleanings generated hazing (that was visible to the naked eye) due to scratching (that was visible microscopically) on pitch-polished and pad-polished surfaces of NWW and WW samples of all glass types [as shown for surface S1 of 7A in

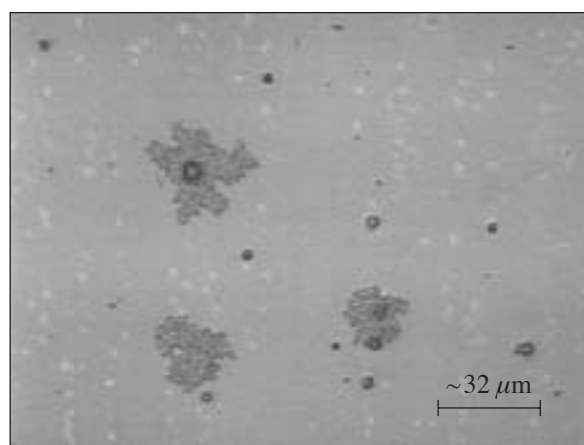


Figure 100.47

Optical microscope image of raster MRF-processed NWW-LG770 (S2 of 8C) after 14 weeks of storage at 75% RH, before cleaning, viewed in bright field at 50 \times .

Fig. 100.45(b)]. The microscopic scratches are believed to be caused by subsurface damage from finishing and not by cleaning. During cleaning, these scratches become enlarged (along with other defects) by water-induced corrosion of the glass surface.^{7,17} Considerably less hazing and scratching were observed on the MRF-processed surfaces. We attribute this improved quality to the ability of MRF to both polish without creating subsurface damage and to remove subsurface damage from previous processing.¹⁸ These obvious visible changes were only modestly supported by measured changes in areal rms roughness and power-density levels, as discussed below.

Areal *p-v microroughness* was reduced to below initial levels on *WW surfaces of all glass types* after one aqueous cleaning. This finding indicates that the drag-wiping protocols performed on the samples before the experiment began were insufficient to rid the surfaces of debris remaining from the various finishing processes. One application of the more-aggressive aqueous cleaning process was sufficient to remove most of this debris. After a second aqueous cleaning, areal *p-v* values remained unchanged. *NWW surfaces of C-LHG8 and CM-LHG8* behaved similarly, exhibiting areal *p-v* levels reduced to below initial values after one aqueous cleaning, and these remained unchanged after a second aqueous cleaning. Cleaning was not as effective on *NWW surfaces of CM-LG770*. After one aqueous cleaning, these surfaces exhibited *p-v* values below those at 13 weeks, but still higher than initial. After a second aqueous cleaning, areal *p-v* generally increased on these surfaces.

Changes in *rms microroughness* for all NWW parts stored at 75% RH are given in Table 100.I. After the first aqueous cleaning, surfaces of CM-LHG8 were unchanged from what they were at the beginning of the experiment. Most surfaces of C-LHG8 and CM-LG770 samples showed significant improvement from their degraded (week 13) states. Areal roughness was reduced by 18% to 74%. All CM-LG770 surfaces were still much rougher than they had been at the beginning of the experiment. A second cleaning did not further reduce roughness. For seven out of ten surfaces, rms-roughness levels increased.

Changes in the rms-microroughness values on NWW samples after aqueous cleaning were reflected in the PSD data. On the pitch-polished sample of NWW C-LHG8 (S1 of 7A), two aqueous cleanings uniformly lowered power density over all spatial frequencies; however, they did not return the surface to its initial condition, as can be seen in Fig. 100.40. After two aqueous cleanings, areal rms roughness and PSD levels were

returned to their initial conditions for the MRF-processed surfaces of NWW C-LHG8 (S1 of 8A and S2 of 8A) (shown in Fig. 100.41).

On samples of NWW CM-LG770, different spatial-frequency regions were affected differently by aqueous cleaning. PSD data for the rotationally MRF-processed surfaces of NWW CM-LG770 (S1 of 8C) are shown in Fig. 100.42. Structures at high- and middle-range spatial frequencies were significantly reduced. Aqueous cleaning did not reduce structures at low spatial frequencies. Power density actually *increased* at spatial frequencies between 3×10^{-6} 1/nm and 4×10^{-7} 1/nm, which explains why rms-microroughness values remained high.

Changes in *rms microroughness* for all WW parts stored at 75% RH are given in Table 100.II. After the first aqueous cleaning, 6 of 10 surfaces were brought to a level equal to or better than that measured at the beginning of the experiment. All six of these surfaces had been processed with MRF. Most of the MRF-processed surfaces continued to improve after a second cleaning. Results were mixed for the surfaces that had been pitch polished or pad polished.

Summary/Conclusions

No samples of LHG8 (cast/continuously melted) or LG770 (continuously melted) exhibited any change after 10 weeks of exposure at 21°C to humidity at 38% RH or less. Changes were seen on *some* of the samples stored in 75% RH at 21°C, and several conclusions can be made regarding the sensitivity to humidity and cleaning of well-polished (with rms microroughness below 2 nm) LHG8 and LG770 surfaces exposed to these conditions.

Among glass types:

1. Continuously melted LHG8 is more resistant to humidity-induced degradation than cast LHG8. Continuously melted LHG8 surfaces exhibit no degradation after 14 weeks of exposure, while cast LHG8 surfaces exhibit little to moderate degradation.
2. Continuously melted LG770 surfaces exhibit severe degradation after 14 weeks of exposure, indicating that continuously melted LG770 is much more sensitive to humidity than either type of LHG8.

Table 100.I: Areal rms microroughness of NWW samples after aqueous cleaning. Percent changes in roughness after each cleaning are noted.

	NWW rms (nm)	Initial (week 0)	Final (week 13)	After First Cleaning (week 14)	After Second Cleaning (week 19)
C-LHG8	S1 of 7A (pitch)	0.63±0.15	3.89±2.50	1.02±0.12 (-74%)	1.75±0.94 (+72%)
	S1 of 8A (rot MRF)	0.79±0.07	1.38±0.50	1.10±0.19 (-20%)	0.89±0.07 (-19%)
	S2 of 8A (rast MRF)	0.78±0.05	1.13±0.41	0.93±0.10 (-18%)	0.98±0.16 (+5%)
CM-LHG8	S1 of 7B (pitch)	0.72±0.04	0.70±0.01	0.70±0.01 (+0%)	0.78±0.01 (+11%)
	S1 of 8B (rot MRF)	0.86±0.08	0.87±0.12	0.84±0.16 (-3%)	0.80±0.08 (-5%)
	S2 of 8B (rast MRF)	0.89±0.03	0.82±0.05	0.80±0.02 (-2%)	0.92±0.14 (+15%)
CM-LG770	S1 of 7C (pitch)	0.70±0.01	13.84±9.72	5.93±1.16 (-58%)	7.59±3.08 (+28%)
	S2 of 7C (pad)	2.05±0.34	8.41±4.31	9.61±3.06 (+14%)	12.51±5.97 (+30%)
	S1 of 8C (rot MRF)	0.91±0.08	12.21±6.43	9.87±3.24 (-19%)	16.68±13.21 (+69%)
	S2 of 8C (rast MRF)	1.46±0.11	24.26±21.95	13.51±5.00 (-44%)	10.01±2.30 (-26%)

Table 100.II: Areal rms microroughness of WW samples after aqueous cleaning. Percent changes in roughness after each cleaning are noted.

	WW rms (nm)	Initial (week 0)	Final (week 13)	After First Cleaning (week 14)	After Second Cleaning (week 19)
C-LHG8	S1 of 15A (pitch)	0.71±0.07	0.74±0.10	0.76±0.06 (+3%)	0.74±0.03 (-3%)
	S1 of 16A (rot MRF)	0.84±0.15	0.90±0.25	0.73±0.04 (-19%)	0.72±0.05 (-1%)
	S2 of 16A (rast MRF)	0.84±0.07	1.02±0.32	0.82±0.08 (-20%)	0.76±0.07 (-7%)
CM-LHG8	S1 of 15B (pitch)	0.72±0.03	0.77±0.06	0.86±0.02 (+12%)	0.93±0.02 (+8%)
	S1 of 16B (rot MRF)	0.89±0.05	1.05±0.12	0.81±0.04 (-23%)	0.79±0.09 (-2%)
	S2 of 16B (rast MRF)	0.98±0.07	0.88±0.06	0.86±0.06 (-2%)	0.86±0.02 (+0%)
CM-LG770	S1 of 15C (pitch)	0.72±0.03	0.76±0.07	0.98±0.08 (+29%)	1.18±0.18 (+22%)
	S2 of 15C (pad)	1.56±0.11	1.34±0.09	1.72±0.20 (+28%)	1.66±0.05 (-3%)
	S1 of 16C (rot MRF)	0.94±0.07	1.74±1.93	0.91±0.07 (-48%)	0.89±0.11 (-2%)
	S2 of 16C (rast MRF)	1.38±0.19	1.38±0.08	1.38±0.15 (+0%)	1.38±0.19 (+0%)

3. Aqueous cleaning can improve surfaces of cast LHG8 and continuously melted LG770 after *severe degradation* by humidity, but it cannot return them to their original conditions. (Aqueous cleaning of degraded continuously melted LG770 surfaces can significantly reduce structures at high- and middle-range spatial frequencies, but it is not effective at removing large structures at low spatial frequencies.)

For all glass types:

4. There is no clear correlation between initial finished surface quality (among surfaces with better-than-2-nm-rms microroughness) and quantifiable magnitude of degradation due to humidity; however, different surface structures develop on surfaces finished with different processes.
5. Gentle weekly drag wiping with methanol prevents humidity-induced degradation.
6. A single aqueous cleaning is sufficient to remove debris from polishing remaining on glass surfaces after gentle drag wiping and storage for 14 weeks.

7. One or two aqueous cleanings can cause increased haze from microscopic scratches on surfaces finished with pitch or pads.
8. MRF processing ensures that at least two aqueous cleanings can be performed to remove debris, without risk of increasing surface haze from microscopic scratches. We attribute this result to the low levels of subsurface damage remaining on surfaces after MRF processing.

ACKNOWLEDGMENT

The authors thank H. Romanofsky of the Center for Optics Manufacturing at the University of Rochester for MRF processing of the samples. We thank A. Maltsev of LLE for pitch polishing and G. Kowski and G. Mitchell of LLE for sample cleaning, inspection, and microscopy. The idea for this work was prompted by an internal poster paper prepared by P. Ehrmann and J. Campbell of LLNL and made available to J. Kelly of LLE in January 2004. The authors acknowledge the Laboratory for Laser Energetics at the University of Rochester for continuing support. One of the authors (JD) is an LLE Horton Fellow. This research was also supported by the U.S. Department of Energy (DOE) Office of Inertial Confinement Fusion under cooperative agreement DE-FC52-92SF19460, the University of Rochester, and the New York State Energy Research and Development Authority. The support of the DOE does not constitute an endorsement by the DOE of the views expressed in this article.

REFERENCES

1. T. I. Suratwala *et al.*, in *Optical Engineering at the Lawrence Livermore National Laboratory II: The National Ignition Facility*, edited by M. A. Lane and C. R. Wuest (SPIE, Bellingham, WA, 2004), Vol. 5341, pp. 102–113.
2. Laboratory for Laser Energetics LLE Review **96**, 207, NTIS document No. DOE/SF/19460-509 (2003). Copies may be obtained from the National Technical Information Service, Springfield, VA 22161.
3. D. C. Brown, S. D. Jacobs, J. A. Abate, O. Lewis, and J. Rinefierd, in *Laser Induced Damage in Optical Materials: 1977*, edited by A. J. Glass and A. H. Guenther, Natl. Bur. Stand. (U.S.), Spec. Publ. 509 (U.S. Government Printing Office, Washington, DC, 1977), pp. 416–422.
4. W. Seka, J. Soures, O. Lewis, J. Bunkenburg, S. Jacobs, G. Mourou, J. Zimmermann, and D. Brown, *Appl. Opt.* **19**, 409 (1980).
5. J. H. Campbell *et al.*, *J. Non-Cryst. Solids* **263–264**, 342 (2000).
6. T. I. Suratwala *et al.*, “Polishing Slurry Induced Haze on Phosphate Laser Glasses,” to be submitted to the *Journal of Non-Crystalline Solids*.
7. “Staining and Dimming in Polishing Process,” Technical Report No. HGW-0-6904E, Hoya Glass Works, Ltd. (1970).
8. “Receive, Clean, Inspect, and Package Laser Amplifier Slabs,” NIF Operations Procedure No. NIF50100570A, Lawrence Livermore National Laboratory, Livermore, CA (2002).
9. D. Golini, S. Jacobs, W. Kordonski, and P. Dumas, in *Advanced Materials for Optics and Precision Structures*, edited by M. A. Ealey, R. A. Paquin, and T. B. Parsonage, Critical Reviews of Optical Science and Technology (SPIE, Bellingham, WA, 1997), Vol. CR67, pp. 251–274.
10. J. E. DeGroot, H. J. Romanofsky, I. A. Kozhina, J. M. Schoen, and S. D. Jacobs, in *Manufacturing and Testing V*, edited by H. P. Stahl (SPIE, Bellingham, WA, 2004), Vol. 5180, pp. 123–134.
11. VWR Humidity/Temperature Pen with Memory, VWR Catalog No. 35519-049, VWR Scientific, St. Paul, MN 55121.
12. Horizontal laminar flow hood, surpasses Class 100 conditions, Dexon Manufacturing, Inc., Rush City, MN 55069.
13. Zygo NewView™ 100 Settings—Filter: Off; Remove: Cylinder; Remove Spikes: Off; Min Mod: 5%; Scan Length: 20- μ m bipolar; FDA Res: High; Min Area Size: 7.
14. J. E. DeGroot, S. N. Shafir, J. C. Lambropoulos, and S. D. Jacobs, presented at The 88th OSA Annual Meeting, Rochester, NY, 10–14 October 2004.
15. Specification taken from LLNL/NIF Drawing No. AAA96-105113, Lawrence Livermore National Laboratory, Livermore, CA.
16. E. L. Church, in *Precision Surface Metrology*, edited by J. C. Wyant (SPIE, Bellingham, WA, 1983), Vol. 429, pp. 105–112.
17. T. Izumitani *et al.*, in *The Science of Ceramic Machining and Surface Finishing II*, edited by B. J. Hockey and R. W. Rice, Natl. Bur. Stand. (U.S.), Spec. Publ. 562 (U.S. Government Printing Office, Washington, DC, 1979), pp. 417–425.
18. J. A. Menapace *et al.*, in *Laser-Induced Damage in Optical Materials: 2001*, edited by G. J. Exarhos *et al.* (SPIE, Bellingham, WA, 2002), Vol. 4679, pp. 56–68.

Nanoscale Vibrational Analysis of Single-Walled Carbon Nanotubes

Introduction

Since their discovery in the early 1990s by Iijima,¹ carbon nanotubes have become the focus of intense interest by a vast number of scientists and engineers. The main reason behind such wide-ranging attention lies in their unique electrical,² mechanical,³ thermal,³ and optical properties.⁴ Furthermore, from their size and structure, carbon nanotubes provide a unique system for investigating one-dimensional quantum behavior.⁵

Although many detailed studies have focused on the electronic and mechanical properties of bundles and individual single-walled carbon nanotubes (SWNT's), there has been, to date, no extensive spectral analysis of the properties of SWNT's via their vibrational spectrum on the single-tube level with a spatial resolution of the order of 15 nm. Spectral analysis of individual SWNT's has been carried out in the past,⁶ but the techniques used were limited by the inability of conventional confocal microscopy to image and localize nanoscale features with subwavelength resolution.^{7–9} Consequently, localized features such as defects or dopants have not been resolved so far. In the work reported here, high-resolution microscopy was performed on individual SWNT's to avoid averaging of the Raman signal. Our unique ability to surpass this limit (i.e., sub-diffraction-limited imaging) lies at the heart of our near-field Raman technique.¹⁰

Raman spectroscopy is a powerful tool for studying the chemical composition of matter since the energy range of electronic transitions lies within the visible spectrum of electromagnetic radiation. This study focuses on the four main first-order features of SWNT Raman scattering: the radial breathing mode (RBM) (~ 100 to 300 cm^{-1}), the Raman active *D* band ($\sim 1300\text{ cm}^{-1}$), *G* band ($\sim 1594\text{ cm}^{-1}$), and *G'* band ($\sim 2600\text{ cm}^{-1}$).^{11–14}

The Raman spectrum can be thought of as a unique chemical fingerprint from which to extract a wealth of information on the electronic structure of SWNT's. For example, the nanotube diameter, chirality, and structure (*n,m*) [(*n,m*) defines the atomic coordinates for the one-dimensional (1-D) unit cell of

the nanotube] are associated with the frequency of the RBM; metallic and semiconducting nanotubes can be distinguished based on the shape of the *G* band (and RBM frequency); and the *D*-band intensity indicates the presence of defects and other disorder-induced effects.

By introducing a sharp gold tip (tip-enhanced Raman spectroscopy^{10,15–17}) in the focus of a tightly focused laser beam, the Raman excitation area can be localized to $\sim 15 \times 15\text{ nm}^2$. The high spatial frequencies associated with this electromagnetic field confinement allow us to record (near-field) Raman images of SWNT's with a spatial resolution of the order of 10 to 20 nm. Precise spectroscopic information can be extracted as the tip is positioned along a SWNT of interest. In this way unique vibrational maps can be built that show the spatial variation of several Raman active modes along many different SWNT's. We believe that the ability to map spectral changes along SWNT's, with nanoscale precision, will lead to a greater understanding of the fundamental properties of such materials on the single-tube level.

Experimental Section

Our near-field Raman setup¹⁰ is based on an inverted optical microscope with the addition of an *x,y* stage for raster-scanning samples. Light from a He-Ne laser (633 nm, 50 to 200 μW) is reflected by means of a dichroic beam splitter and then focused onto the surface of the sample using a high-numerical-aperture objective (N.A. = 1.4).

Having obtained a tight focal spot at the sample surface, a sharp, gold tip is then positioned into the focal region. Care is taken to align the tip with one of the two longitudinal field components in the focal plane.¹⁸ The gold tip is held at a constant height of 1 nm by means of a shear-force detection feedback mechanism¹⁹ with an rms noise of $\sim 0.5\text{ \AA}$ in the *z* direction. Using the *x,y* stage to raster scan the sample, Raman-scattered light is collected with the same objective and is recorded using either a single-photon-counting avalanche photodiode (APD) or a spectrograph with a charge-coupled device (CCD) cooled to -124°C .

SWNT's were grown by the arc-discharge method³ and purchased commercially. They were then dispersed in a solution of dichloroethane, sonicated in an ultrasonic bath, and spin cast at 3000 rpm onto a glass cover slip. Our metal tips were produced by electrochemically etching thin, gold wire in a solution of hydrochloric acid (HCl) for ~30 s.

Results

The primary motivation of this study is to probe, with nanoscale resolution, the main vibrational modes of spatially isolated, individual SWNT's; to relate spectral variations to the tube structure (RBM); and to localize defects (*D* band) along the tube axis.

Figure 100.48(a) shows a diffraction-limited, confocal Raman image recorded by raster scanning a sample with a single SWNT through the focused laser. The contrast in the image results from integrating the Raman spectrum for each image pixel over a narrow spectral range centered at $\nu = 2600 \text{ cm}^{-1}$ (*G'* band). Figure 100.48(b) shows the corresponding near-field Raman image taken over the exact same sample area. This image results from placing a sharp metal tip (25-nm diameter) into the laser focus. The spatial resolution is ~14 nm [full width at half maximum (FWHM)] as shown by the inset of Fig. 100.48(b).

Figure 100.48(c) shows the corresponding Raman-scattering spectrum for a certain nanotube position with and without the tip present. The increase in Raman-scattering strength demonstrates clearly the effect of surface-enhanced Raman scattering (SERS). The SERS enhancement factor depends on the ratio of the near-field and confocal interaction volumes. Typical enhancement factors are in the range of 10^2 to 10^4 (Ref. 10).

In the next step, a sample area was located with single nanotubes that show detectable signals for all four Raman active bands. Figures 100.49(a)–100.49(d) show a series of near-field spectral images of two individual SWNT's corresponding to the *G*, *G'*, *D*, and RBM Raman bands.

From these images one can clearly observe the spatial variation in Raman-scattered light for all four Raman bands. Both the *G* and *G'* bands [Figs. 100.49(a) and 100.49(b)] show a near-uniform-intensity profile along the nanotube in the center of the image, as one might expect for a defect-free SWNT. This observation is further strengthened by the weak intensity of the disorder-induced *D* band [Fig. 100.49(c)]. The most striking spectral feature is the localized scattering associated with the RBM. Figure 100.49(d) illustrates that only one nanotube, namely the SWNT in the center of the image, is

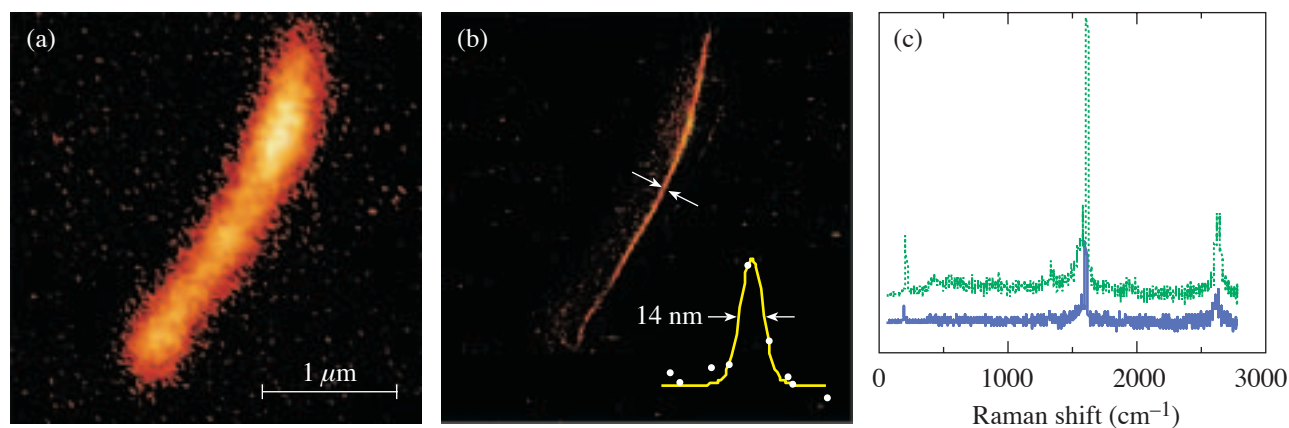


Figure 100.48

[(a) and (b)] Raman-scattering images of a single SWNT deposited on a glass coverslip. The contrast in the images reflects the local intensity of the Raman *G'* band: 2600 cm^{-1} . (a) A confocal Raman image and (b) the corresponding near-field Raman image. The integration time was 10 ms per image pixel. The inset in (b) shows a Gaussian fit to the line section shown (FWHM of 14 nm). The FWHM taken from (a) was ~275 nm. (c) Raman-scattering spectrum for a single SWNT with (upper) and without (lower) a metal tip present. The graphs are offset for clarity.

resonantly excited with our light source. The detected RBM frequency was measured to be $\sim 205\text{ cm}^{-1}$, indicating that we observe a (14,1) nanotube. Using the relation $\nu_{\text{RBM}} = A/d_t + B$, (where $A = 223.5\text{ nm/cm}$ and $B = 12.5\text{ cm}^{-1}$),¹⁴ we calculate the tube diameter to be $1.16 \pm 0.2\text{ nm}$. Atomic force microscopy (AFM) measurements confirm that it is indeed a single nanotube, its diameter being measured topographically to be $\sim 1.3\text{ nm} \pm 0.3\text{ nm}$.

To understand the origin of these local variations, we first discuss the resonance conditions associated with the different Raman bands. The RBM resonance window is different compared to the resonance windows for the G , G' , and D Raman modes.⁷ The RBM is more likely to change in the presence of

nanotube defects, such as localized changes in the structure of the nanotube lattice [changes in (n,m)], kinks, and intertube junctions in addition to interactions with the glass substrate on which the SWNT's are dispersed. Any of these variations will affect the van Hove transition energy E_{ii} and detune the RBM out of resonance. For the G , G' , and D Raman active bands respectively, any small change in E_{ii} is unlikely to manifest itself in similarly dramatic spectral variations.

The dispersive G , G' , and D bands are discussed in terms of a double resonance effect that relaxes the resonance condition.¹² On the other hand, the RBM originates from a single resonance process, resulting in a slightly narrower resonance window.¹³ Since the resonance windows for the Raman active G and G' bands are broader in nature, dramatic spectral changes are not as expected, as can be seen in Figs. 100.49(a) and 100.49(b). However, as will be reported in a later publication, we have observed significant spectral variations, on the single-tube level, in the G and G' Raman bands for SWNT's that have been doped with elemental boron.²⁰

Figure 100.49(c) reveals the presence of a small amount of scattered light associated with the Raman D band centered at 1267 cm^{-1} . In light of the weak signal associated with this band, we relate such scattering to disorder-induced effects within the tube lattice itself or the coupling to the supporting substrate. In a related study on boron-doped tubes, we have observed significant increases of D -band scattering, localized with 20-nm resolution, along several different SWNT's.²⁰

In light of our work, it should be noted that recent experiments on SWNT's suspended from Si pillars have shown Raman signals that are more intense when compared to SWNT's in contact with a silicon surface;²¹ however, no localized spectral analysis has been reported so far for suspended SWNT's. The ability to perform such localized analysis of suspended SWNT's should provide a better understanding of the effects of nanotube–surface interactions on the variations of the vibrational modes of SWNT's.

Our observation and explanation of the RBM localization are consistent with the results that we acquired for many different tube structures (assigned from RBM frequency). Figures 100.50(a)–100.50(e) show further evidence for localized Raman scattering associated with the following Raman active modes: namely, (a) the G band, (b) D band, (c) RBM, (d) intermediate-frequency modes (IFM),¹³ and (e) M band.²² Figure 100.50(f) shows a three-dimensional AFM profile of the nanotube studied.

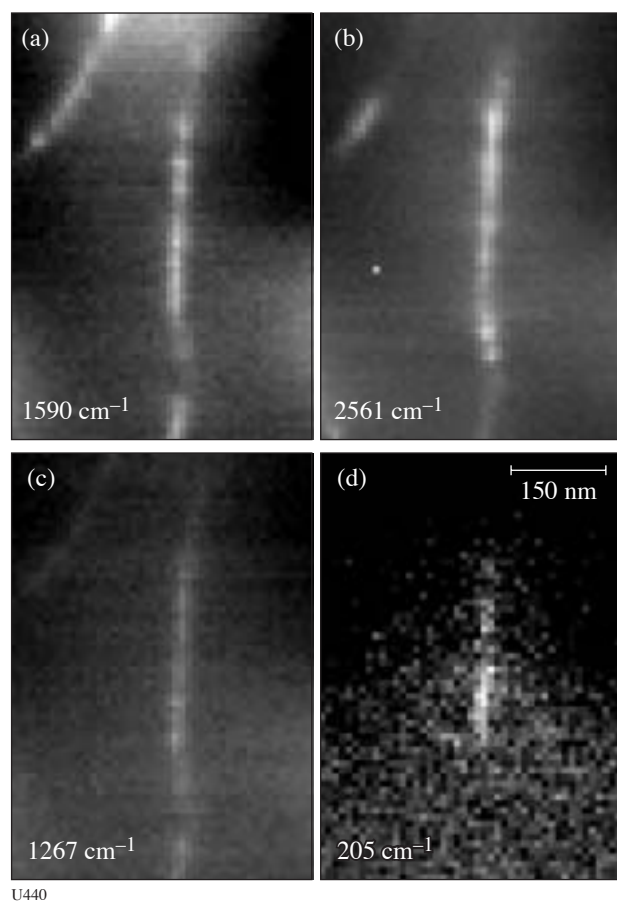


Figure 100.49
Near-field spectral images, upon laser excitation at 633 nm, for the Raman active (a) G band, (b) G' band, (c) D band, and (d) RBM. The images were produced from the Raman-scattered light detected with a cooled CCD. (Integration time: 210 ms per image pixel.) The most-striking feature is the localization of the RBM associated with the vertically aligned SWNT.

Once again localized spectral variations of the RBM are observed. The RBM signal decreases dramatically in the presence of ~ 3 -nm-high catalyst particles located at the tube's end. This observation is consistent with the idea that changes in the tube structure can lead to a loss of resonance Raman-scattering properties of SWNT's. From Fig. 100.50(b) considerable *D*-band scattering is also observed at the beginning of the tube, where a small kink is present, and near the end with the small catalyst particles. The vibrational modes shown in Figs. 100.50(d) and 100.50(e) are recorded along a single

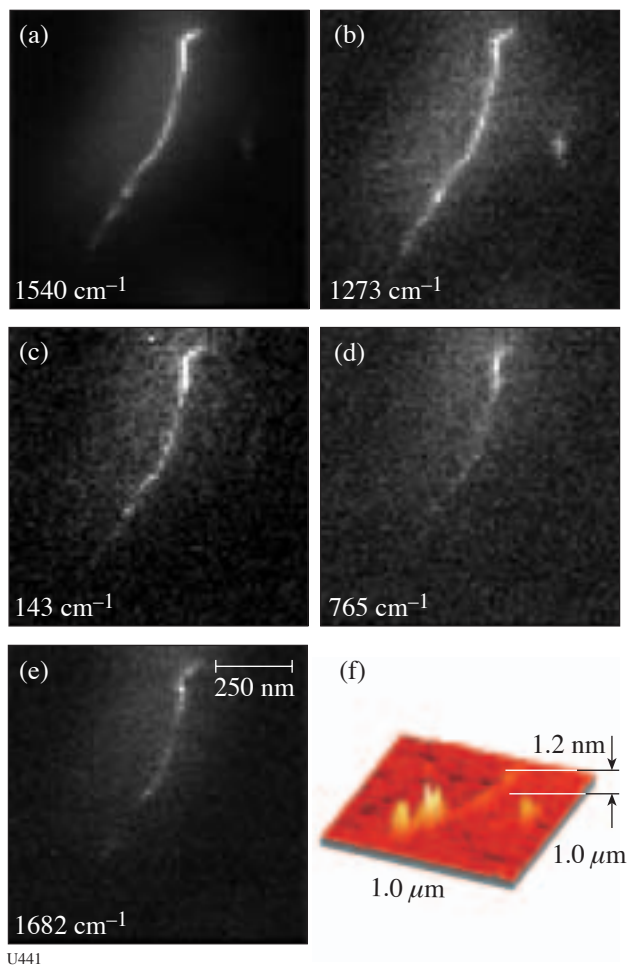


Figure 100.50

[(a)–(e)] Near-field spectral images for different Raman bands. (f) A 3-D topographical profile of the nanotube studied. Two bands previously unseen in our SWNT studies are (d) an intermediate-frequency mode (IFM)^{13,23} and (e) the Raman active *M* mode.²² Again the presence of a spatially varying RBM along the nanotube length is observed. The RBM, as well as the IFM and *M* bands, decrease in strength near the attached ~ 3 -nm particle(s), which is presumably a residual Ni/Y catalyst particle left over from the growth process.

nanotube for the first time. The two bands are designated as an intermediate frequency mode (IFM) and *M* band, respectively, and are known from the literature.^{13,22} The *M* band is the sum of the RBM and the *G* band, although it should be noted that the *M* band also appears in the Raman spectrum of graphite. Our calculations show that subtracting the frequency of the *G* band from the *M* band gives 142 cm^{-1} . This is consistent with the measured value of the RBM frequency: 143 cm^{-1} . From this measured RBM frequency we assign a nanotube structure of (23,1); i.e., $(n,m) = (23,1)$. To the best of our knowledge, no previous attempt has been made to understand why both the IFM and *M* modes are localized similar to the observed spatial variations of the RBM. We conclude that both the IFM and *M* band are dependent on the tube structure (n,m) in the same manner as the RBM. This claim is strengthened by the fact that these bands are not always detectable for either SWNT bundles or individual SWNT's. Future work should provide more-detailed insight into the spatial variation of these two bands and any possible dependence on the tube diameter, i.e., (n,m) .

For all near-field Raman images, a topographic image (not shown in Figs. 100.48 and 100.49), acquired simultaneously, provides a valuable crosscheck for the (n,m) assignments based on the RBM frequency. All SWNT's studied had their diameters calculated from the spectral position of their (diameter-dependent) RBM frequencies. The calculated value was then compared with the corresponding AFM measurements to confirm that they were, indeed, individual SWNT's and not small bundles. In addition, the same gold tip was used to acquire all of the images shown.

Conclusion

In conclusion, using near-field Raman imaging and spectroscopy, several vibrational modes have been mapped along spatially isolated, individual SWNT's resting on a glass substrate with 20-nm resolution. Our results demonstrate that high-resolution microscopy is necessary to avoid averaging of the Raman spectrum along individual SWNT's. As such, our results reveal the highly localized nature of the light scattering associated with the RBM frequency from several different SWNT's. Such spectral features are ascribed to the sensitive nature of the RBM resonance condition. Variations in the RBM scattering are attributed to the surrounding environment (nanotube–substrate interactions) and its effect on the nanotube structure (n,m) and hence transition energy E_{ij} . Furthermore, little variation in intensity has been observed for both the *G* and *G'* Raman bands. Such small variations result from the different resonance conditions for these bands in comparison with the resonance window of the RBM for SWNT's. Finally,

detectable Raman scattering associated with disorder-induced effects has been observed; however, for many perfectly aligned SWNT's, little or no *D*-band intensity has been detected.

ACKNOWLEDGMENT

The authors wish to thank Dr. A. Bouhelier and Dr. A. Jorio for stimulating discussions and T. Osedac for tip fabrication. This research has been supported financially by the Air Force Office for Scientific Research (AFOSR) through the Multidisciplinary University Research Initiative (MURI) under Grant No. F-49620-03-1-0379.

REFERENCES

1. S. Iijima, *Nature* **354**, 56 (1991).
2. M. T. Woodside and P. L. McEuen, *Science* **296**, 1098 (2002).
3. M. S. Dresselhaus, G. Dresselhaus, and P. Avouris, *Carbon Nanotubes: Synthesis, Structure, Properties, and Applications*, Topics in Applied Physics, Vol. 80 (Springer, Berlin, 2001).
4. A. Hartschuh *et al.*, *Science* **301**, 1354 (2003).
5. L. C. Venema *et al.*, *Science* **283**, 52 (1999).
6. A. Mews *et al.*, *Adv. Mater.* **12**, 1210 (2000).
7. M. Souza *et al.*, *Phys. Rev. B* **69**, 241403(R) (2004).
8. K. McGuire *et al.*, "Synthesis and Raman Characterization of Boron-Doped Single-Walled Carbon Nanotubes," submitted to *Physical Review B*.
9. S. B. Cronin *et al.*, *Phys. Rev. Lett.* **93**, 167401 (2004).
10. A. Hartschuh *et al.*, *Phys. Rev. Lett.* **90**, 095503 (2003).
11. A. Jorio *et al.*, *Phys. Rev. Lett.* **86**, 1118 (2001).
12. S. Reich, C. Thomsen, and J. Maultzsch, *Carbon Nanotubes: Basic Concepts and Physical Properties* (Wiley-VCH, Cambridge, England, 2004).
13. A. M. Rao *et al.*, *Science* **275**, 187 (1997).
14. S. W. Bacilo *et al.*, *Science* **298**, 2361 (2002).
15. J. Wessel, *J. Opt. Soc. Am. B* **2**, 1538 (1985).
16. N. Hayazawa *et al.*, *Chem. Phys. Lett.* **335**, 369 (2001).
17. R. M. Stöckle *et al.*, *Chem. Phys. Lett.* **318**, 131 (2000).
18. L. Novotny, E. J. Sánchez, and X. S. Xie, *Ultramicroscopy* **71**, 21 (1998).
19. K. Karrai and R. D. Grober, *Appl. Phys. Lett.* **66**, 18424 (1995).
20. N. Anderson *et al.*, in preparation.
21. Y. Kobayashi *et al.*, *Chem. Phys. Lett.* **386**, 153 (2004).
22. V. W. Brar *et al.*, *Phys. Rev. B* **66**, 155418 (2002).
23. In a recent article C. Fantini *et al.* discuss the origin of IFM's for many different laser wavelengths. See *Phys. Rev. Lett.* **93**, 087401 (2004) for further details.

Polymer Cholesteric Liquid Crystal Flake Reorientation in an Alternating-Current Electric Field

Introduction

The motion and orientation of nonspherical particles suspended in a host fluid and subjected to an alternating-current (ac) electric field have been well studied theoretically. Because the dielectric properties of the two phases of the suspension differ, charge will start to accumulate at the particle–fluid interface due to Maxwell–Wagner polarization. This charge accumulation induces a dipole moment, which is acted on by the electric field, causing the particle to reorient. Basic electromagnetic theory predicts that a particle in an electric field will orient in the direction corresponding to the lowest energy so as to minimize the potential energy of the system. Typically this requires a dielectric nonspherical particle to align its longest axis parallel to the external field.¹ Because the minimum energy orientation of the particle depends on the shape, the dielectric properties of the host fluid and particle, and the frequency of the ac field, it is possible that a particle will have varying stable orientations at different frequencies. Schwartz *et al.*² described the orientation of particles in an ac electric field and considered the conditions for particles with anisotropic dielectric properties or with additional membranes or layers, which is of particular use in the biological sciences. Okagawa *et al.*³ derived similar equations for a uniform dielectric particle but included the effect of shear flow on the particle motion. Jones did further work in the field of particle electromechanics, including phenomena such as electrophoresis and dielectrophoresis,⁴ and a comprehensive review of electromechanical behavior of particles was written by Gimsa.⁵ In addition to conducting experiments with biological particles,⁶ Miller and Jones investigated highly dielectric particles, such as titanium dioxide.⁷ Bostwick and Labes also performed similar experiments using platelets of crystalline nafoxidine hydrochloride.⁸ In this article we report on the orientation of highly dielectric polymer cholesteric liquid crystal (PCLC) particles (flakes), suspended in a low-viscosity host fluid. Though much of the theory on particle electromechanics is well supported by experimental work in the biological sciences, relatively little work has been done to

study the behavior of highly dielectric particles like PCLC flakes, which have no inherent charge, a low dielectric constant, and a negligible dielectric anisotropy.

PCLC Flakes

PCLC flakes were developed in the 1990s as an alternative to both low-molar-mass cholesteric liquid crystals (LMMLC's) and PCLC thin films. Typical LMMLC molecules can be switched with an electric field, which provides control over their optical properties, but LMMLC's tend to be temperature sensitive and require confining substrates to retain liquid crystalline order. Due to a relatively high glass transition point, PCLC films are not temperature sensitive and can stand alone without substrates. Despite this environmental stability and the usefulness for passive applications, freestanding polymer LC films cannot be manipulated in electric fields. PCLC flakes have the potential to combine two important properties of PCLC films and LMMLC's: environmental stability and electro-optic switching.⁹

PCLC flakes are formed by fracturing thin PCLC films into randomly shaped particles of the order of tens to hundreds of microns.¹⁰ More recently, techniques for processing uniformly shaped flakes with replication methods such as soft lithography have been developed.¹¹

An important and unique characteristic of PCLC flakes is that they display selective reflection, a Bragg-like effect resulting from the “helical” molecular structure of PCLC's aligned in the Grandjean texture. Selective reflection causes light of a specific wavelength and (circular) polarization to be reflected from the flake surface. Thus, a large visual effect is created if flakes are viewed off-axis or if they are tipped with respect to normally incident light, whereby the wavelength of selective reflection shifts toward shorter wavelengths and is also diminished. This optical effect provided the motivation for controlling the position, and thus the color and reflectivity, of a PCLC flake using an electric field.¹²

Theory

The response time for flake motion is determined by solving the equation of motion for an ellipsoid, which includes the electrostatic torque exerted on a polarized ellipsoid whose rotation is opposed by a hydrodynamic (viscous) torque from the surrounding host fluid. The mass moment of inertia is neglected because viscosity, and not the flake's inertia, dominates the system. The inertial contribution is several orders of magnitude smaller than contributions from the electrostatic and hydrodynamic torques, i.e., the system is critically damped.

The electrostatic torque $\vec{\Gamma}_E$ is defined as the cross product of the induced dipole moment \vec{p} and the applied electric field \vec{E}_o :

$$\vec{\Gamma}_E = \vec{p} \times \vec{E}_o. \quad (1)$$

Here we assume that the particle material has no permanent dipole moment and that the applied electric field is uniform over the flake dimensions. The electric field inside the particle E^+ , to which the particle responds, varies with the rotation of the ellipsoid and induces an effective polarization along each ellipsoidal axis i :

$$P_i = (\epsilon_p - \epsilon_h) E_i^+, \quad (2)$$

where

$$E_i^+ = \frac{\epsilon_h E_{oi}}{\epsilon_h + A_i(\epsilon_{ii} - \epsilon_h)}, \quad (3)$$

ϵ_p and ϵ_h are the dielectric permittivity of the particle and host fluid, respectively, and E_{oi} is the applied electric field component along the particle axis i . Calculations for an electrically isotropic particle can be performed by considering $\epsilon_{11} = \epsilon_{22} = \epsilon_{33} = \epsilon_p$. The ellipsoid is described by axes lengths a_i , a_j , and a_k , and a depolarization factor A_i must be defined along each axis (where i, j , and k are indices ordered according to the right-handed coordinate system):

$$A_i = \frac{a_i a_j a_k}{2} \int_0^\infty \frac{ds}{(s + a_i^2) \sqrt{(s + a_i^2)(s + a_j^2)(s + a_k^2)}}. \quad (4)$$

The effective induced dipole moment along each particle axis p_i is

$$p_i = \frac{4\pi}{3} a_i a_j a_k P_i = \frac{4\pi}{3} a_i a_j a_k \epsilon_h K_i E_{oi}, \quad (5)$$

where we have defined the Clausius–Mosotti factor K_i along each ellipsoidal axis as

$$K_i = \frac{(\epsilon_p - \epsilon_h)}{[\epsilon_h + A_i(\epsilon_p - \epsilon_h)]}. \quad (6)$$

Since the dielectric particle and the surrounding medium are not ideal dielectrics, energy dissipation mechanisms such as conduction and dielectric relaxation require that a frequency-dependent complex dielectric constant ϵ^* be considered:

$$\epsilon^*(\omega) = \epsilon - i \frac{\sigma}{\omega}, \quad (7)$$

where ω is the electric field frequency and σ is the electric conductivity. The definitions for K_i^* and p_i^* remain unchanged except that ϵ_p and ϵ_h become complex and frequency dependent. Using Eqs. (1) and (5), we find the electrostatic torque Γ_{Ei} along the particle axis i to be

$$\Gamma_{Ei} = \frac{4\pi}{3} a_i a_j a_k \epsilon_h K_j^* K_k^* (A_k - A_j) E_{oj} E_{ok}. \quad (8)$$

It is important to note that the ϵ_h arising from the effective induced dipole moment [Eq. (5)] is not complex because it is not derived from Gauss's law.[†] The hydrodynamic torque Γ_{Hi} about particle axis i is defined as

$$\Gamma_{Hi} = -\frac{16\pi}{3} a_i a_j a_k \eta_o \frac{(a_j^2 + a_k^2)}{(a_j^2 A_j + a_k^2 A_k)} \Omega_i, \quad (9)$$

[†]See Jones⁴ (Appendix G) for a derivation of the induced effective moment of a dielectric ellipsoid, which includes the electrostatic potential external to the ellipsoid.

where η_o is the absolute viscosity of the host fluid and Ω_i is the angular velocity about axis i . The hydrodynamic and electrostatic torques about a specific axis are equated to give the equation of motion for a rotating flake. The angular velocity Ω_i relative to its corresponding axis i is found to be

$$\Omega_i = \frac{\varepsilon_h \varepsilon_o K_j^* K_k^* (A_k - A_j) E_{oj} E_{ok}}{4\eta_o} \frac{(a_j^2 A_j + a_k^2 A_k)}{(a_j^2 + a_k^2)}. \quad (10)$$

We first examine the two-dimensional implication of this result. The two-dimensional coordinate system and reference frame for the flake are defined in Fig.100.51, where θ is the instantaneous angle between the flake's surface normal and the applied electric field.

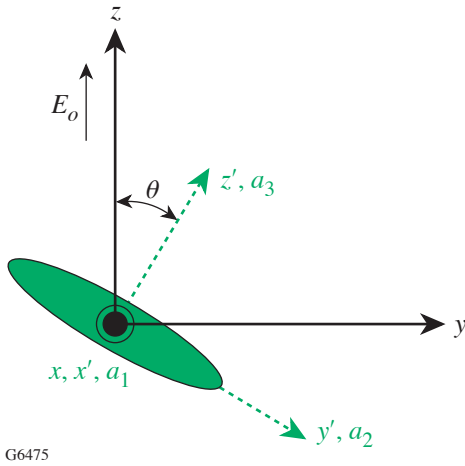


Figure 100.51
The flake reference frame (primed axes) rotates with respect to the laboratory (cell) reference frame (unprimed axes).

If we consider the case where the electric field E_o is applied along the z axis and the flake rotates about axis a_1 (x'), the angular velocity about the flake axis is found to be

$$\frac{d\theta}{dt} = \Omega_1 = \frac{\varepsilon_h \operatorname{Re}\{K_3^* K_2^*\} (A_3 - A_2) E_o^2}{4\eta_o} \frac{(a_2^2 A_2 + a_3^2 A_3)}{(a_2^2 + a_3^2)} \sin\theta \cos\theta. \quad (11)$$

We retain the real component of the equation because only the time-averaged term is significant in a heavily damped system where the particle moves slowly compared to the applied electric field. This equation is easily simplified and solved in the form

$$\frac{d\theta}{dt} = \frac{C}{2} \sin 2\theta, \quad \text{where}$$

$$C = \frac{\varepsilon_h \operatorname{Re}\{K_3^* K_2^*\} (A_3 - A_2) E_o^2}{4\eta_o} \frac{(a_2^2 A_2 + a_3^2 A_3)}{(a_2^2 + a_3^2)}. \quad (12)$$

Equation (12) can be integrated to obtain an equation for the angle θ at any given time:

$$\tan \theta = \tan \theta_o e^{t/\tau_c}, \quad (13)$$

where θ_o is the initial angle (position) of the flake and $\tau_c = 1/C$ is the time constant for flake relaxation. We can see that for all $\tau_c > 0$, as $t \rightarrow \infty$ the angle $\theta \rightarrow \pi/2$ is a stable configuration. It is now possible to determine the response time of the flake, or the time needed for θ to approach any final orientation, including $\theta \approx 90^\circ$. The reorientation time from the initial angle θ_o to the current angle θ is given by

$$t = \tau_c \ln \left(\frac{\tan \theta}{\tan \theta_o} \right) = \frac{4\eta_o}{\varepsilon_h \operatorname{Re}\{K_e^* K_2^*\} (A_3 - A_2) E_o^2} \frac{(a_2^2 + a_3^2)}{(a_2^2 A_2 + a_3^2 A_3)} \ln \left(\frac{\tan \theta}{\tan \theta_o} \right). \quad (14)$$

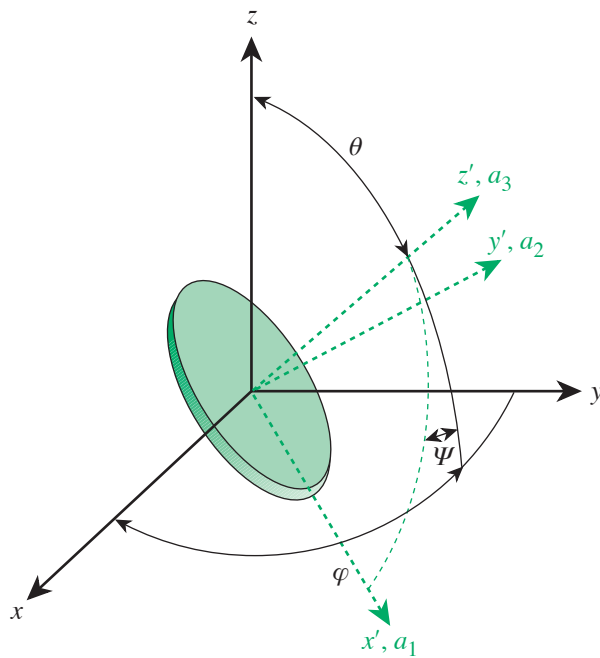
Equation (14) clearly shows that the flake reorientation time should have an inverse quadratic dependence on the applied electric field and a linear dependence on the fluid viscosity. There must be a slight perturbation in the flake position ($\theta_o > 0^\circ$) in order for flake motion to commence.

A three-dimensional model that accounts for the coupling between the components of angular velocity about each axis was developed by Okagawa³ (see Fig. 100.52). Based on Okagawa's work, the time rate of change of each angle can be found in terms of the components of angular velocity of the

flake defined by Eq. (10), where

$$\begin{aligned} \frac{d\theta}{dt} &= \Omega_1 \cos\psi + \Omega_2 \sin\psi, \\ \frac{d\varphi}{dt} &= (\Omega_2 \cos\psi - \Omega_1 \sin\psi) \cos\theta, \\ \frac{d\psi}{dt} &= \Omega_3 - (\Omega_2 \cos\psi - \Omega_1 \sin\psi) \cot\theta. \end{aligned} \quad (15)$$

Allowing $\psi = 0$ eliminates the angle describing the spin of the flake and simplifies the equations. We solved these equations numerically, and the results validated the two-dimensional analytic solution.



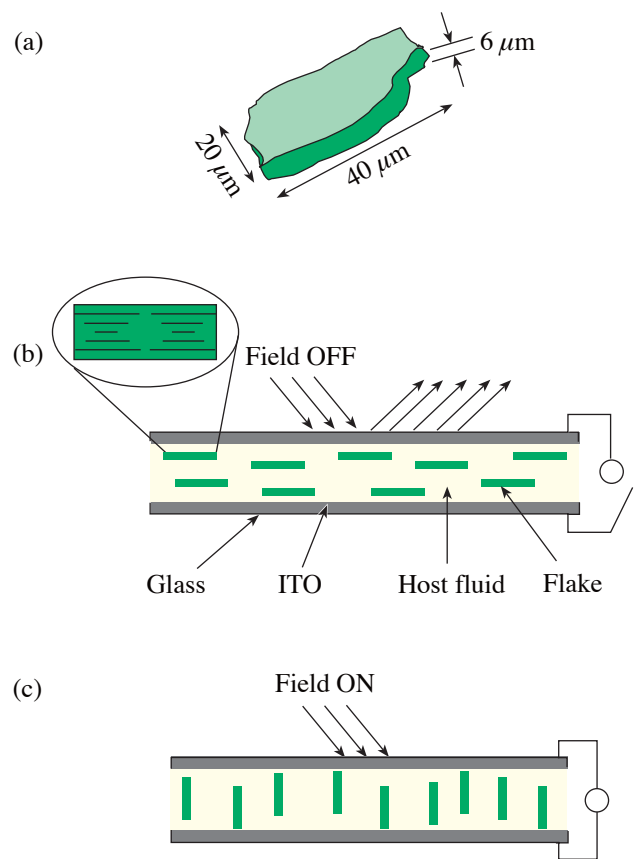
G6499

Figure 100.52 Coordinate systems of the (unprimed) laboratory reference frame and the (primed) ellipsoid reference frame. The z' identifies the direction normal to the surface of an oblate particle.

Experimental Procedure

Commercial polycyclosiloxane flakes,¹³ typically $6 \mu\text{m}$ thick, with an arbitrary shape and a selective reflection peak at $\lambda_o = 520 \text{ nm}$ (green), were sieved and dried to obtain batches with sizes between 20 and $40 \mu\text{m}$ [Fig. 100.53(a)]. The PCLC flakes were suspended in two host fluids: a silicone oil (Gelest,

DMS-T05) and propylene carbonate (PC) (Aldrich, 99.7% HPLC grade). Though both fluids are transparent, chemically compatible with the PCLC material, and of a comparable density, their dielectric properties varied greatly. The silicone oil had a low dielectric permittivity and was highly insulating ($\epsilon_h \sim 3 \epsilon_o$, $\sigma_h \sim 10^{-11} \text{ S/m}$), while the PC had a high dielectric permittivity and was significantly more conductive ($\epsilon_h \sim 69 \epsilon_o$, $\sigma_h \sim 10^{-6} \text{ S/m}$). Test cells were constructed using pairs of indium tin oxide (ITO)-coated glass substrates. A mixture of soda lime glass spheres dispersed in a UV-curing epoxy was applied in four corners of one substrate to set the cell gap. Assembled cells were then filled with the flake/host fluid suspension by capillary action and sealed with additional epoxy.



G5408

Figure 100.53 Dimensions of a typical irregularly shaped PCLC flake are depicted in (a). Flakes lie approximately parallel to cell substrates when no electric field is applied (b) and appear green due to selective reflection caused by the helical molecular structure of cholesteric liquid crystals, as depicted by the enlarged cross-sectional view of a flake. Flakes reorient with one long axis parallel to the applied field (c). They appear dark since light is no longer reflected off their flat surfaces.

Basic observations were made using a Leitz Orthoplan polarizing microscope. A Panasonic Digital 5100 camera with a timer was used to record flake motion with a time resolution of 100 ms. Data on subsecond flake motion were obtained by detecting the light reflected from the rotating flake surface using a Hamamatsu R905 photomultiplier tube (PMT) coupled to the microscope ocular by means of a fiber optic mounted in a precision fiber coupler. The PMT signal was displayed on one channel of an HP 54520A oscilloscope and directly compared with the field applied to the cell displayed on the second channel. Flake motion was easily detected under near-normal illumination through a 10 \times objective (N.A. = 0.2). Brightly reflecting flakes lying in the plane defined by the substrates [Fig. 100.53(b)] darkened substantially with only a few degrees of rotation [Fig. 100.53(c)] as they continue reorienting to align parallel with the electric field.

Experimental Results and Discussion

The motion of PCLC flakes in a sinusoidal ac electric field was investigated mainly in the propylene carbonate host system because no motion was observed in the silicone oil host system.* Reorienting PCLC flakes exhibited several characteristics: Flakes consistently rotated about the longest axis, so that the shorter major axis aligned parallel to the applied field direction. Furthermore, flakes with larger aspect ratios (length to width) reoriented more quickly than flakes of a comparable size, but with a smaller aspect ratio. Once the driving field was turned off, flakes returned to their initial position in the plane of the cell. This approximate 90 $^\circ$ relaxation required anywhere from several seconds to several minutes to be completed. There was also a gradual and approximately linear increase in response time over the lifetime of the PCLC flake test device during test periods of 2 days.

Both the electric-field frequency and magnitude affected flake reorientation times. Flake motion was seen within a specific frequency bandwidth (\sim 10 Hz to 1 kHz), above and below which flake reorientation did not occur (Fig. 100.54). Motion for a typical flake was detected in fields as low as 5 mV_{rms}/μm, but fields above 30 mV_{rms}/μm were required for flake reorientation to occur on a subsecond time scale. The inverse quadratic dependence on the electric field was observed clearly as the flake reorientation time was tested as a function of applied voltage (Fig. 100.55).

From Eq. (14), it is clear that the measured inverse quadratic dependence of the response time on the applied field supports the theoretical model predictions of the previous section. The dependence on the flake shape is more complicated, but a study

of seven specific PCLC flakes suspended in PC and observed in a 10.4-mV_{rms}/μm field at 50 Hz showed clearly that the reorientation time decreases as the aspect ratio increases. This shape-dependent behavior was also as predicted by the theoretical model (Fig. 100.56).

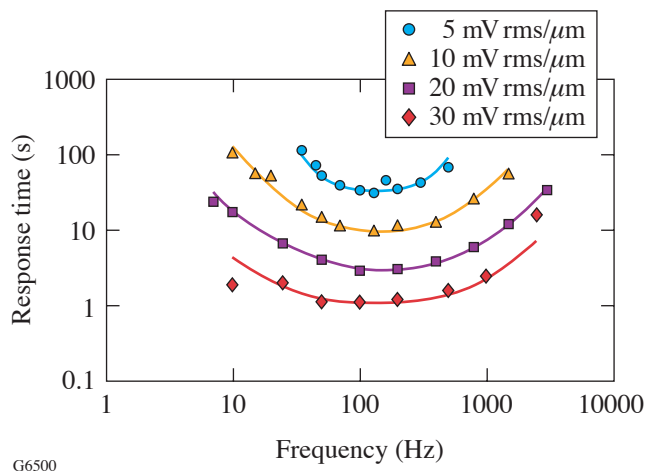


Figure 100.54

The characteristic time response of a representative PCLC flake as a function of frequency at specific electric-field values. Lines are drawn to guide the eye. Similar behavior was observed for dozens of individual flakes.

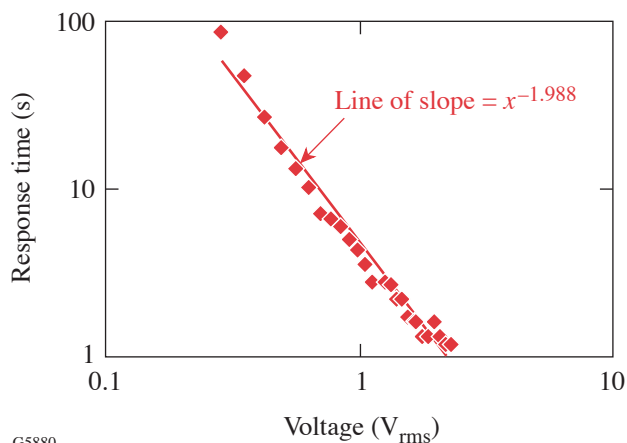


Figure 100.55

The average response time of several flakes exhibited an inverse quadratic dependence on the applied voltage. The standard deviation of 10% is of the order of the size of the data points. Data was collected at 50 Hz.

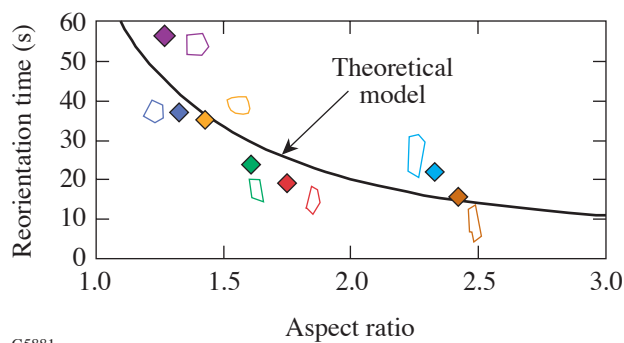


Figure 100.56

A correlation between response time and flake size and shape was observed. Flakes with the largest aspect (length to width) ratio reorient the fastest.

Though many of the observations above were supported by theory, two results were not supported by previous theoretical work. For flakes with axes $a_1 > a_2 > a_3$, we expected that the flakes would align with their longest axis a_1 , parallel to the electric field. Instead, we observed that the flakes consistently aligned with the shorter major axis a_2 , parallel to the applied electric field. Schwarz² used the Clausius–Mosotti factor K_i , which measures the energy of the ellipsoid when it is oriented with its i axis parallel to the field, to predict the stable orientation of the particle. He suggested that the axis with the smallest K_i would align parallel to the applied field. Using the following typical parameters we found that, for all frequencies, K_1 had the smallest value: $\epsilon_h \sim 69 \epsilon_o$; $\sigma_h \sim 10^{-6}$ S/m; $\epsilon_p \sim 2.89 \epsilon_o$; $\sigma_p < 10^{-11}$ S/m; $a_1 = 35 \mu\text{m}$; $a_2 = 15 \mu\text{m}$; and $a_3 = 5 \mu\text{m}$. This result indicated that the longest axis a_1 should align with the electric field, which is contrary to our observations.

Jones produced a chart for determining the preferred axis alignment based on a combination of signs of the torque terms for each axis. In practice, only the sign of the real component of the Clausius–Mosotti term ($K_j^* K_k^*$) was considered because it is proportional to the torque [Eq. (8)]. Considering only the Clausius–Mosotti terms excludes the difference in depolarization factors ($A_k - A_j$). This difference term can flip the sign of the torque if A_k is less than A_j . We used the Jones chart, initially considering just $\text{Re}\{K_j^* K_k^*\}$ and then including $(A_k - A_j)\text{Re}\{K_j^* K_k^*\}$, to predict which flake axis would align with the electric field. Neither method produced results that correspond with our observations.

To predict which particle axis would align parallel to the electric field, we found it necessary to consider not only the electric torque but also contributions of the viscous drag (hydrodynamic torque), which become more important as the

lengths of the two major axes become more similar. One way to include the effects of the viscous drag was to compare the magnitude of the angular velocity components about each axis. Assuming that the particle reorients about the axis with the largest angular velocity component, and for the material parameters given above, we found that a flake lying nearly parallel to the substrate will reorient about the longest axis a_1 , so that the shorter of the two major axes, a_2 , aligns parallel to the electric field, just as we had observed. This result will be true unless the flake's initial condition is already tilted largely about the shorter axis a_2 .

The second result not supported by theoretical work arose when we compared our model of flake reorientation times with electric-field frequency. Initially we used the real part of the Clausius–Mosotti factor in the electric torque term, and the resultant theoretical model showed a weak frequency dependence. The characteristic *S* shape of the theoretical curve (Fig. 100.57, insert) shifted toward higher (lower) frequencies when host fluids with a higher (lower) conductivity were modeled. However, the model predictions using the *S*-shaped curve agreed poorly with the experimental data. The data showed a minimum reorientation time at a specific frequency above and below which the reorientation times increased. The model based on the real component of the Clausius–Mosotti factor corresponded well only with the general order of magnitude of the flake reorientation time (Fig. 100.57).

Because the frequency dependence of the reorientation time data resembled the typical dispersion spectrum for the imaginary part of the dielectric constant, we also explored using the imaginary part of the Clausius–Mosotti factor in our model. Use of the imaginary component produced a theoretical curve with a *U* shape that agreed well with the shape of the experimental data. However, the predicted response times were more than an order of magnitude higher than those observed.

The imaginary component of the Clausius–Mosotti term is typically used only in equations describing electro-rotation, which is the continuous rotation of a particle in the presence of a rotating electric field.⁴ When there is a rotating electric field, it is necessary to consider the phase angle of K_i^* , which represents a (constant) phase lag between the applied electric field and the induced moment. Physically, the induced dipole lags behind the applied field by an angle related to the time necessary for the dipole moment to form as charge builds up at the particle–fluid interface. The angular velocity of the particle will vary from the angular velocity of the rotating electric field, and the particle will typically be rotating more slowly (due to

the viscous drag) than the surface charge on the particle that produced the induced dipole.

Since the conditions for PCLC flake reorientation include a linear electric field with which the induced dipole moment eventually aligns, we cannot assume a constant phase between these two vectors. However, the imaginary component also helps quantify the time required to induce the dipole moment, which might explain why using this term models the frequency-dependent behavior of the flake reorientation time so well.

The discrepancy between the predicted and observed reorientation times implies that either the viscosity of the host fluid is much lower or the *effective* electric field (to which the flake responds) is significantly larger than the applied electric field. The viscosity of propylene carbonate is well known, so it is possible that the effective electric field is larger. This possibility would imply that perhaps another electric-field-dependent term has not been considered in the expression for the electric torque.

Summary

We have observed that flakes suspended in a moderately conductive host fluid, such as propylene carbonate, reorient about their longest axis to align the shorter major axis parallel to the applied electric field. This observation was contrary to most theories on particle reorientation, which predict that the longest axis will align with the applied electric field. We compared the components of the angular velocity about each axis, which include important parameters such as particle shape and host fluid viscosity, hypothesizing that the flake will rotate about the axis with the largest angular-momentum component. This approach was found to support our observations. Other standard characteristics of PCLC flake motion, such as the inverse quadratic dependence on the electric field and the tendency for longer, asymmetric flakes to reorient faster, were theoretically predicted and agreed with our experimental observations.

The frequency dependence of the flake reorientation time was difficult to model because it is unclear whether the real or the imaginary component of the Clausius–Mosotti term should

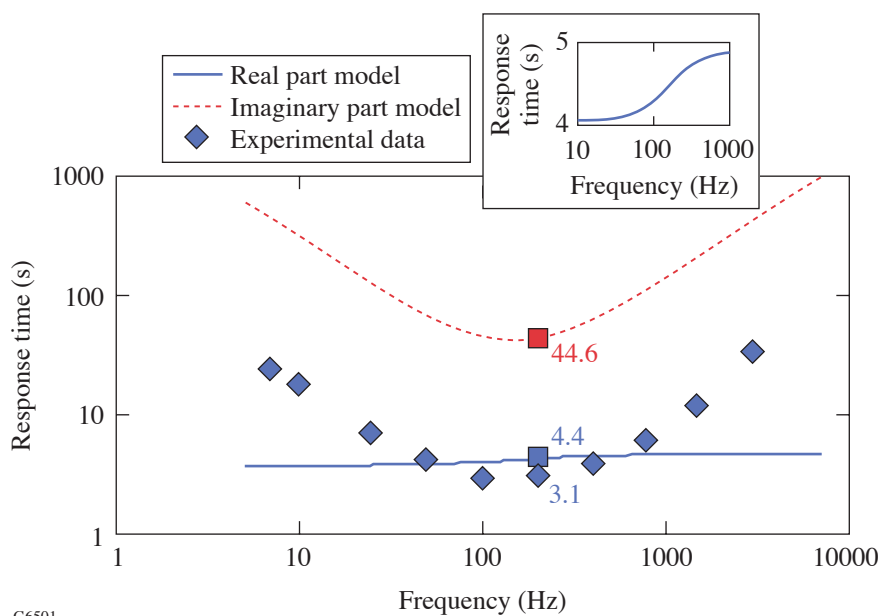


Figure 100.57

A comparison of experimental data and a theoretical model based on experimental parameters ($E_o = 20 \text{ mV}/\mu\text{m}$; $\eta_o = 2.9 \text{ cP}$; $\epsilon_h \sim 69 \epsilon_o$; $\epsilon_p \sim 2.89 \epsilon_o$; $\sigma_p < 10^{-12} \text{ S/cm}$) and estimated values ($\sigma_h \sim 10^{-6} \text{ S/m}$; $a_1 = 35 \mu\text{m}$; $a_2 = 15 \mu\text{m}$; $a_3 = 5 \mu\text{m}$). The open squares designate the theoretical values for comparison with the experimental data at 200 Hz. The insert shows the frequency dependence of the model that utilized the real component of the Clausius–Mosotti term on an expanded semi-log scale.

be used. Using the real component, which is a widely accepted approach, the model predicts reorientation times on the same order of magnitude as the observed reorientation times; however, the frequency dependence does not match the experimental data. This discrepancy is partially resolved by using the imaginary component in the model. The theoretical curve based on the imaginary component shows a minimum reorientation time at a specific electric-field frequency, which corresponds well with experimental data. This alternate method also predicts, however, reorientation times approximately an order of magnitude higher than what we observed. Future research will require investigating effects of electro-osmosis, double layers, and rotating electric fields. Similar frequency-dependent particle behavior has been observed when a rotating electric field causes a particle to rotate. The particle rotation results from a phase difference between the electric-field-induced polarization and the rotating field, thereby requiring theory to consider the imaginary component of the Clausius-Mosotti term.¹⁴

The ability to reorient, or switch, PCLC flakes provides a way to control their unique optical and polarizing properties with an electric field. Electro-optic devices based on switching PCLC flakes are useful in a broad class of applications in information displays, optics, and photonics. A PCLC flake device is of particular interest in the display industry (large-area signs, automobile dashboards, heads-up displays, and “electronic paper”) because it easily provides both color and polarization without the use of filters and polarizers, which reduce brightness and add to the production cost. Possible applications in optics and photonics include switchable and tunable optical retardation or modulation elements for polarized light at any desired wavelength or bandwidth. It is also possible to produce conformal PCLC flake coatings for use in either decorative applications or military applications such as camouflage, document security, anti-counterfeiting, and object tagging and identification. Thus reorienting PCLC flakes has an unlimited number of potential applications, many of which have yet to be conceived.

ACKNOWLEDGMENT

The authors would like to acknowledge the Laboratory for Laser Energetics at the University of Rochester for continuing support. This work was also supported by the U.S. Department of Energy Office of Inertial Confinement Fusion under Cooperative Agreement No. DE-FC52-92SF19460, the University of Rochester, and the New York State Energy Research and Development Authority. The support of DOE does not constitute an endorsement by DOE of the views expressed in this article.

REFERENCES

*Flake motion in the silicone oil was observed only when dc fields were applied, whereby typical flake motion was random and uncontrolled. The system relaxation time was very long due to the low conductivity of the silicone oil host, which prevented a stable dipole moment from being induced.

1. J. A. Stratton, *Electromagnetic Theory*, 1st ed., International Series in Physics (McGraw-Hill, New York, 1941).
2. G. Schwarz, M. Saito, and H. P. Schwan, *J. Chem. Phys.* **43**, 3562 (1965).
3. A. Okagawa, R. G. Cox, and S. G. Mason, *J. Colloid Interface Sci.* **47**, 536 (1974).
4. T. B. Jones, *Electromechanics of Particles* (Cambridge University Press, New York, 1995).
5. J. Gimsa, *Bioelectrochemistry* **54**, 23 (2001).
6. R. D. Miller and T. B. Jones, *Biophys. J.* **64**, 1588 (1993).
7. R. D. Miller, “Frequency-Dependent Orientation of Lossy Dielectric Ellipsoids in AC Electric Fields,” Ph.D. thesis, University of Rochester, 1989.
8. B. D. Bostwick and M. M. Labes, *Appl. Phys. Lett.* **45**, 358 (1984).
9. K. L. Marshall, T. Z. Kosc, S. D. Jacobs, S. M. Faris, and L. Li, U.S. Patent No. 6,665,042 B1 (16 December 2003).
10. E. M. Korenic, S. D. Jacobs, S. M. Faris, and L. Li, *Mol. Cryst. Liq. Cryst.* **317**, 197 (1998); S. M. Faris, U.S. Patent No. 5,364,557 (15 November 1994).
11. A. Trajkovska-Petkoska, R. Varshneya, T. Z. Kosc, K. L. Marshall, and S. D. Jacobs, “Enhanced Electro-Optic Behavior for Shaped Polymer Cholesteric Liquid Crystal (PCLC) Flakes Made by Soft Lithography,” to be published in *Advanced Functional Materials*.
12. T. Z. Kosc, K. L. Marshall, S. D. Jacobs, J. C. Lambropoulos, and S. M. Faris, *Appl. Opt.* **41**, 5362 (2002).
13. Wacker-Chemie, Consortium für Electrochemische Industrie GmbH, Zielstattstrasse 20, D-81379, München, Germany.
14. W. M. Arnold and U. Zimmermann, *J. Electrostat.* **21**, 151 (1988).

LLE's Summer High School Research Program

During the summer of 2004, 16 students from Rochester-area high schools participated in the Laboratory for Laser Energetics' Summer High School Research Program. The goal of this program is to excite a group of high school students about careers in the areas of science and technology by exposing them to research in a state-of-the-art environment. Too often, students are exposed to "research" only through classroom laboratories, which have prescribed procedures and predictable results. In LLE's summer program, the students experience many of the trials, tribulations, and rewards of scientific research. By participating in research in a real environment, the students often become more excited about careers in science and technology. In addition, LLE gains from the contributions of the many highly talented students who are attracted to the program.

The students spent most of their time working on their individual research projects with members of LLE's technical staff. The projects were related to current research activities at LLE and covered a broad range of areas of interest including laser optics modeling, analysis of OMEGA implosion experiments, hydrodynamics modeling, cryogenic target characterization, liquid crystal physics and chemistry, materials science, the development and control of laser fusion diagnostics, and OMEGA EP laser system design and engineering (see Table 100.III).

The students attended weekly seminars on technical topics associated with LLE's research. Topics this year included laser physics, fusion, holographic optics, fiber optics, femtosecond lasers and their applications, computer-controlled optics manufacturing, and global warming. The students also received

safety training, learned how to give scientific presentations, and were introduced to LLE's resources, especially the computational facilities.

The program culminated on 25 August with the "High School Student Summer Research Symposium," at which the students presented the results of their research to an audience including parents, teachers, and LLE staff. The students' written reports will be bound into a permanent record of their work that can be cited in scientific publications. These reports are available by contacting LLE.

One hundred and seventy-six high school students have now participated in the program since it began in 1989. This year's students were selected from approximately 50 applicants.

At the symposium, LLE presented its eighth William D. Ryan Inspirational Teacher Award to Mr. Claude Meyers, a former physics teacher at Greece Arcadia High School. This award is made to a teacher who motivated one of the participants in LLE's Summer High School Research Program to study in the areas of science, mathematics, or technology and includes a \$1000 cash prize. Teachers are nominated by alumni of the summer program. Mr. Meyers was nominated by David Bowen, a participant in the 2001 Summer Program. "Claude Meyers impressed me as someone who was easily capable of being a college professor, or even a serious, doctorate-carrying researcher," David writes in his nomination letter. According to David, Mr. Meyers was an outstanding physics teacher with a deep love and understanding of physics, who was able to impart his students with excitement and respect for the principles of physics.

Table 100.III: High School Students and Projects—Summer 2004.

Name	High School	Supervisor	Project Title
Daniel Balonek	Byron-Bergen HS	D. Jacobs-Perkins	Mechanical Characterization of Cryogenic Targets
Gregory Balonek	Byron-Bergen HS	S. Craxton	How Good Is the Bright-Ring Characterization of Cryogenic Target Uniformity?
Robert Balonek	Byron-Bergen HS	D. Lonobile	Design and Fabrication of a Handheld, Fiber Optic-Coupled, Coolant Water Flow Detector Test Fixture
Bruce Brewington	Fairport HS	S. Craxton	3-D Characterization of Deuterium-Ice-Layer Imperfections
Daniel Butler	Brighton HS	R. Boni	Automated Focusing of the ROSS Streak Tube Electron Optics
Jeremy Chang	Penfield HS	M. Guardalben	Grating Compressor Modeling
Joseph Dudek	Honeoye-Falls-Lima HS	C. Stoeckl	Hexapods and Multiple Coordinate Systems
Laurie Graham	Bloomfield HS	S. Regan	Experimental Investigation of Far Fields on OMEGA
Jivan Kurinec	Rush-Henrietta HS	M. Bonino/ D. Harding	Material Properties of Spider Silk at Cryogenic Temperatures
Jonathan Kyle	Gates-Chili HS	J. DePatie	Two-State Motor Controller
Ted Lambropoulos	Pittsford-Mendon HS	J. Marozas	Optimal Pinhole Loading via Beam Apodization for OMEGA EP
Yekaterina Merkulova	Penfield HS	J. Delettrez	Spatial Distribution of the Reflected Laser Light at the Experimental Chamber Wall
Arun Thakar	Pittsford-Mendon HS	R. Epstein	Numerically Calculated Spherical Rayleigh-Taylor Growth Rates
Glen Wagner	Fairport HS	T. Kosc/ K. Marshall	Computer Modeling of Polymer Cholesteric Liquid Crystal Flake Reorientation
Tina Wang	Webster-Schroeder HS	V. Smalyuk	Modeling of X-Ray Emission in Spherical Implosions on OMEGA
Ariel White	East Irondequoit-Eastridge	K. Marshall	Photopatterning of Liquid Crystal Alignment Cells

FY04 Laser Facility Report

The OMEGA Facility conducted a record number 1558 target shots in FY04—a 13% increase over FY03—by operating extended shifts during select weeks to accommodate user demand (see Table 100.IV). Improvements to the Spherical Cryogenic Target Handling System increased system reliability and target positioning stability. More-complex planar cryogenic target assemblies were fielded including planar cryogenic D₂ cells for radiographic measurements of shock timing and cryogenic hohlraums for energy coupling and symmetry studies. Highlights of these changes and other FY04 achievements include the following:

- A total of 35 spherical and 35 planar cryogenic shots were performed. Eight spherical cryogenic target shots were conducted within one week in FY04, demonstrating increased system reliability. The rigidity of the lower pylon structure was improved, and electrically energized docking clamps were installed to increase the stability of cryogenic target alignment. This resulted in an approximately 2× improvement in the target offset at shot time for a series of 20 spherical cryogenic target implosions during Q2 and Q3.
- An improved multichannel IR streak camera (IR3) was installed and integrated into the OMEGA front end, enhancing pulse-shape measurement and prediction capability. This camera measures the temporal input to each of the three OMEGA driver lines, and its data are used in a system performance model that predicts the OMEGA output temporal pulse shape. The combination of the new streak camera's improved CCD camera, much shorter fiber signal delivery system, and the improved channel distribution on its photocathode resulted in a lower noise floor, higher bandwidth, and reduced channel crosstalk. An entirely recoded software user interface made it easy for the operators to use the streak camera. This new camera's enhanced performance was in large measure responsible for successfully fielding 80-ps, picket, low-adiabat pulse shapes used for both the imprint growth measurements on foam targets¹ and the cryogenic target implosion campaigns.
- Improved amplifier-gain-measurement hardware and gain-equalization procedures were implemented on OMEGA. Precision gain matching of all the amplifiers within a stage is crucial to obtaining on-target power balance objectives. OMEGA's harmonic energy diagnostic (HED) system was extended to measure the output of the driver lines, enabling simultaneous on-shot measurement of an amplifier stage's input and output energies. This provided absolute stage-gain-measurement capability and allowed the stage gains to be set to a predetermined value rather than just minimizing gain variance. This improved long-term stage-gain stability (see Fig. 100.58) and dramatically reduced the number of amplifiers that were being flagged for unnecessary maintenance. The more-efficient use of maintenance resources has resulted in their concentration on the worst-performing amplifiers.
- New target designs were also fielded to begin validation of the polar-direct-drive ignition concept proposed for the NIF. These included 40-beam, directly driven "Saturn" ring targets and 40-beam, directly driven CH cells. These were the first LLE experiments to combine symmetric illumination with radiographic diagnostics (backlighting).
- A new UV spectrometer was installed to measure the spectrum of all 60 beams with 0.02 to 0.07 Å of spectral resolution. The spectral data obtained from this instrument provided insight into *B*-integral effects on OMEGA's beamlines. Online spectral-based FCC tuning capability is planned for FY05.
- OMEGA conducted the first cryogenic gas hohlraum experiments for LLNL.

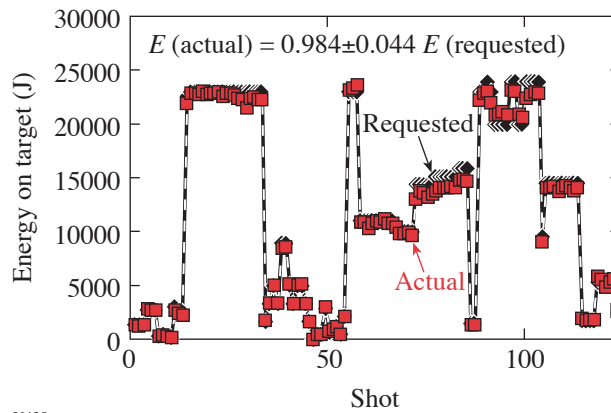
REFERENCES

1. "August 2004 Progress Report on the Laboratory for Laser Energetics, Inertial Confinement Fusion Program Activities," University of Rochester, Rochester, NY (2004).

Table 100.IV: The OMEGA target shot summary for FY04.

Laboratory	Planned Number of Target Shots	Actual Number of Target Shots
LLE	741	756
LLNL	405*	431
LANL	150*	168
SNL	20	31
NLUF	135	127
CEA	25	32
NRL	10	13
Total	1486	1558
LLE ISE		304
LLE SSP		127
LLE RTI		86
LLE DD		69
LLE LPI		60
LLE CRYO		35
LLE ASTRO		30
LLE DDI		24
LLE PB		21
LLE Total		756

* 20 shots in collaboration.



U438

Figure 100.58
Record of requested and actual on-target energy for OMEGA shots in October 2004.

National Laser Users' Facility and External Users' Programs

During FY04, 802 target shots were taken on OMEGA for external users' experiments, accounting for 51.5% of the total OMEGA shots produced this year. External users in FY04 included eight collaborative teams under the National Laser Users' Facility (NLUF) program as well as collaborations led by scientists from the Lawrence Livermore National Laboratory (LLNL), Los Alamos National Laboratory (LANL), Sandia National Laboratory (SNL), Naval Research Laboratory (NRL), and the Commissariat à l'Énergie Atomique (CEA) of France.

NLUF Program

FY04 was the second of a two-year period of performance for the nine NLUF projects approved for FY03–FY04 funding and OMEGA shot time. Eight of the nine NLUF campaigns received a total of 127 shots on OMEGA in FY04.

The Department of Energy (DOE) issued solicitations in FY04 for NLUF proposals for work to be carried out in FY05–FY06. DOE raised the available NLUF funding to \$1,000,000 for FY04 proposals to accommodate the high level of interest in using OMEGA to carry out experiments of relevance to the National Nuclear Security Agency (NNSA) Stockpile Stewardship Program (SSP). NLUF participants use these funds to carry out experiments on OMEGA (including graduate student stipends, travel, supplies, etc.). The participants do not pay any portion of the OMEGA operating costs since these costs are funded directly by the DOE–LLE Cooperative Agreement.

A total of 16 NLUF proposals were submitted to DOE for consideration for FY05–FY06 support and OMEGA shot allocation. An independent DOE Technical Evaluation Panel comprised of Dr. Tina Back (LLNL), Dr. Robert Turner (LLNL), Dr. Steven Batha (LANL), Dr. Ramon Leeper (SNL), and Prof. Ani Aprahamian (University of Notre Dame) reviewed the proposals on 15 June 2004 and recommended that up to 8 of the 16 proposals receive DOE funding and 7 of the 8 teams be approved for shot time on OMEGA in FY05–FY06. Table 100.V lists the successful proposals.

FY04 NLUF Experiments

Programs carried out in FY04 by eight groups of NLUF participants included the following OMEGA experiments:

Optical Mixing Controlled Simulated Scattering Instabilities (OMC SSI): Generating Electron Plasma Waves and Ion-Acoustic Waves to Suppress Backscattering Instabilities

Principal Investigator: B. B. Afeyan (Polymath Research, Inc.)

The goal of this experiment is to examine the suppression of backscattering instabilities by the externally controlled generation of ion-acoustic-wave (IAW) or electron-plasma-wave (EPW) turbulence. The experiments consist of using optical mixing techniques to generate resonant waves in flowing plasmas created by the explosion of target foils by the OMEGA laser.

During FY04, experiments were conducted in which two blue beams as well as a blue beam and a green beam were crossed. Nineteen target shots were taken for this experiment in September 2004 using three new high-intensity-interaction-beam phase plates [known as continuous phase plates (CPP's)] designed by Sham Dixit of LLNL. They provided a near- 10^{15} W/cm² interaction-beam intensity for 1 ns with 500 J of blue-beam energy. The same design was used for a green-beam CPP. In addition, a polarization rotator was fielded on the probe beams of the pump–probe experiments so as to discriminate against processes that do not involve the ponderomotive force generated by the beating of the pump and probe beams directly. The results of these experiments will be described in future publications. The principal conclusion of this six-year-long effort with crossing blue–blue and blue–green beams on OMEGA is that OMC SSI via IAW's is a significant potential tool for the suppression of stimulated Raman backscattering SRBS in high-intensity laser–plasma interaction.

Studies of Ion-Acoustic Waves (IAW's) Under Direct-Drive NIF Conditions

Principal Investigator: H. Baldis (University of California, Davis)

Stimulated Brillouin scattering (SBS) is of concern to laser fusion using the indirect-drive or direct-drive approach. Generally, it is believed that SBS is only a minor effect for direct-drive inertial confinement implosion experiments, particularly those currently conducted on OMEGA. However, scattered-light spectra collected in these implosion experiments show changes from the incident spectra that can arise only from non-linear effects such as SBS. To extrapolate the present results to future larger direct-drive laser fusion experiments, it is necessary to understand the details of the present observations.

To gain better insight into the underlying processes, a series of OMEGA shots was dedicated to measuring SBS in planar geometry with 11 low-intensity beams producing a plasma and one or two interaction beams at oblique incidence.

One of the interaction beams was beam 30 for which there is a full-aperture backscattering station on OMEGA (FABS30). Beam 30 was incident at ~42° to the target normal. The target normal was pointed between the two interaction beams (beams 15 and 30). Thus the specular reflection from beam 15 was also collected by FABS30. In addition, one expects SBS side-scattering to be enhanced in the specular direction due to possible self-seeding of SBS by the specular reflection at the turning point of beam 15. There could be an additional contribution to the light collected by FABS30 from a synergistic interaction between beams 30 and 15 if they are present simultaneously.

All of these conditions are also encountered in spherical implosion experiments. In spherical implosion experiments, however, many different angles of incidence are present simultaneously and may contribute differently depending on the time during the laser pulse. This makes it difficult to unravel the subtleties of the interaction processes, hence the choice of the planar geometry for this series of experiments.

Table 100.V: FY05–FY06 Proposals.

Principal Investigator	Affiliation	Proposal Title
J. Asay	Washington State University	Isentropic Compression Experiments for Measuring EOS on OMEGA
H. Baldis	University of California, Davis	Laser–Plasma Interactions in High-Energy-Density Plasmas
R.P. Drake	University of Michigan	Experimental Astrophysics on the OMEGA Laser
R. Falcone	University of California, Berkeley	NLUF Proposal: Plasmon Density of States in Dense Matter
R. Jeanloz	University of California, Berkeley	Recreating Planetary Core Conditions on OMEGA
P. Hartigan	Rice University	Astrophysical Jets and HED Laboratory Astrophysics
R. Mancini	University of Nevada, Reno	Three-Dimensional Study of the Spatial Structure of Direct-Drive Implosion Cores on OMEGA
R. Petrasso and C. K. Li	Massachusetts Institute of Technology	Implosion Dynamics and Symmetry from Proton Imaging, Spectrometry, and Temporal Measurements

A typical purely sidescattered signal is shown in Fig. 100.59 for a 1-ns square pulse interaction beam at $\sim 2 \times 10^{14}$ W/cm² in beam 15 (beam 30 was not fired). Also shown in Fig. 100.59 for comparison is the input laser spectrum. We note that the basic features of this time-resolved spectrum are the same as for spherical implosions. The initial rapid blue shift reflects the increasing plasma column traversed by the interaction beam as the plasma is formed. This is followed by a return toward zero overall spectral shift as the plasma column becomes stationary. The important difference between the incident and reflected spectra is in the shape of the spectrum late in time, which is narrower with a peak on the red part of the spectrum, compared to the incident spectrum shown as reference on the right side of Fig. 100.59.

Experimental Astrophysics on the OMEGA Laser

Principal Investigator: R. P. Drake (University of Michigan)

This NLUF project is led by the University of Michigan and involves collaborators from Lawrence Livermore National Laboratory; the Laboratory for Laser Energetics; the Universities of Arizona, Chicago, Princeton, and Stony Brook; as well as École Polytechnique and CEA from France. It uses OMEGA to study processes that are relevant to astrophysics, with a specific focus on the unstable nonlinear hydrodynamics that occurs when stars explode and on radiative shocks that occur during stellar explosions and in many other contexts. The experiments to study nonlinear hydrodynamics involved continuing examination of the role of initial conditions on the long-term nonlinear structure that develops after a blast wave encounters an interface. Data were obtained with a controlled variation of initial conditions and also to assess preheat levels. The experiments to study radiative shocks involved measurements of the change in shock velocity and structure with drive

conditions and work to apply an improved diagnostic (a backlit pinhole) to obtain higher-resolution data.

Figure 100.60 shows a radiographic image from the radiative shock experiments, obtained using an area backlighter at 13.5 ns after the drive beams are fired. The grid and a fiducial feature establishing an absolute location are evident in the lower part of Fig. 100.60. The wall of the tube can be seen near the upper edge. The shock front is curved, and there are indi-

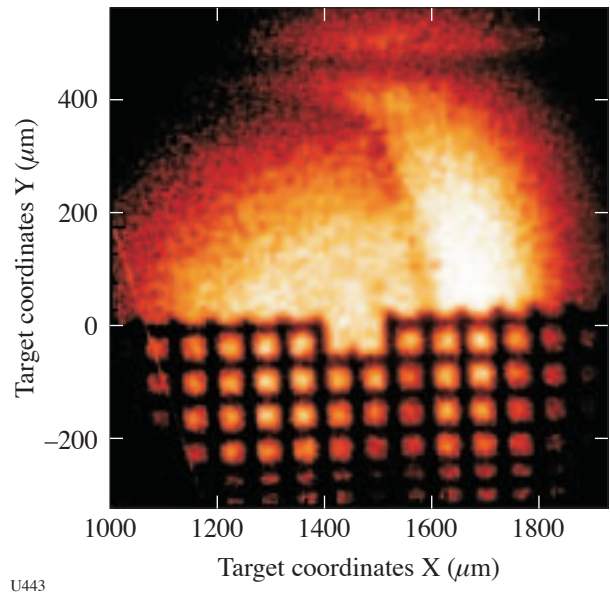
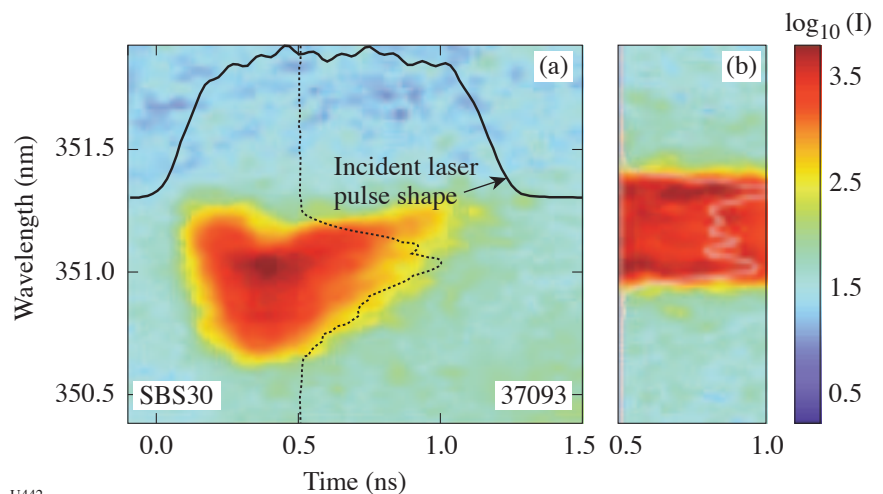


Figure 100.60

A radiographic image of collapsed radiative shock. This image is from an experiment with a polyimide drive disk attached to a polyimide tube of 912- μ m inner diameter, irradiated (with SSD) at 9.3×10^{14} W/cm² onto a 720- μ m laser spot. The illumination was by x rays from Ti produced by overlapping six laser beams.

Figure 100.59

Stimulated Brillouin side scattering (a) from a planar plasma for an interaction beam at oblique ($\sim 42^\circ$) incidence at $\sim 2 \times 10^{14}$ W/cm². The plasma was simultaneously formed by 11 low-intensity laser beams. The incident laser pulse shape is shown as the dark line above the spectrum. A short but representative time slice of the incident laser spectrum is shown in (b). The vertical lineout through the spectra is also shown for both incident and reflected spectra.



cations of a trailing layer of dense xenon along the wall of the tube. The velocity and position of the center of the shock are within 10% of the values obtained from relevant 1-D simulations. The region of highest opacity is narrow, being 45 μm thick in this case. The layer of xenon produced by a nonradiative shock would be 140 to 220 μm thick at this location (depending on the exact equation of state). Thus, it appears that the density has increased another factor of 3 to 4 in consequence of radiative losses, reaching a total of 34 times the initial xenon density.

Recreating Planetary Core Conditions on OMEGA

Principal Investigator: R. Jeanloz (University of California, Berkeley)

During the past 18 months this team collected data on high-pressure H_2 and He fluids, combining diamond-anvil cells and laser-produced shocks (Fig. 100.61) to measure the first off-Hugoniot equation-of-state (EOS) data for both hydrogen (Figs. 100.62–100.64) and helium (Fig. 100.65) and to measure the highest-pressure EOS data ever for fluid helium. The

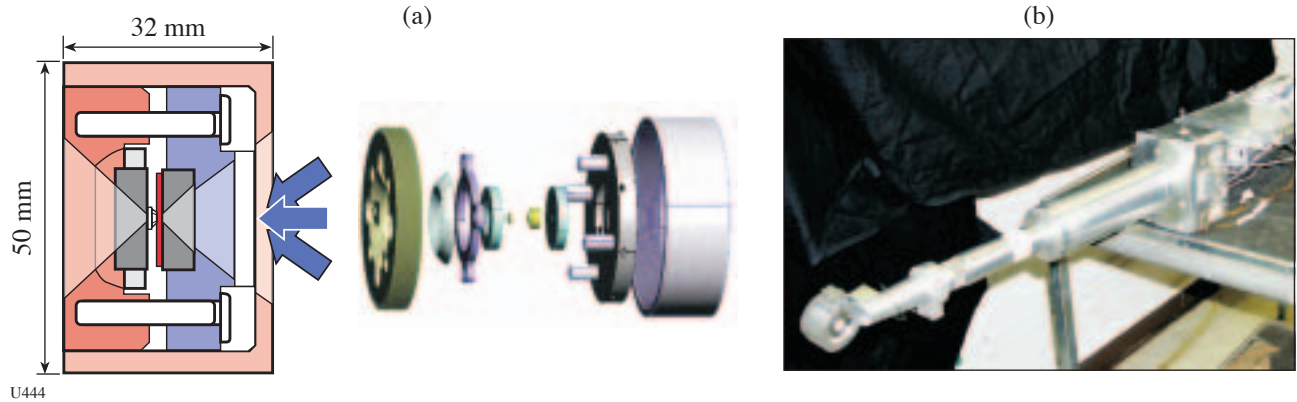
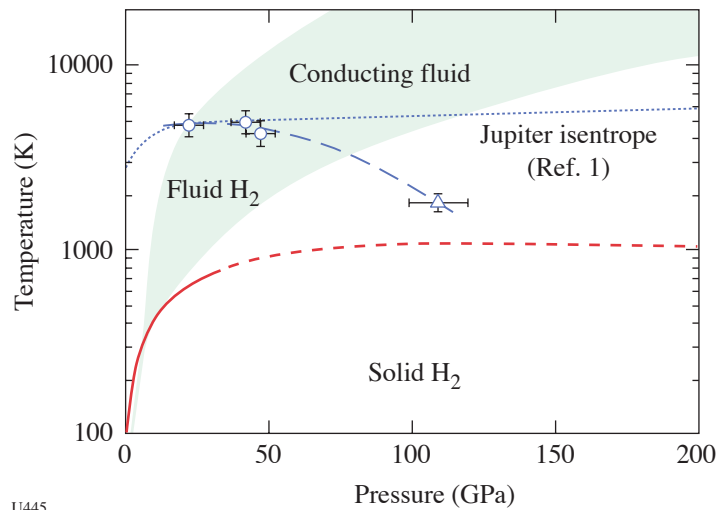


Figure 100.61
(a) Diamond-cell schematic and (b) photograph of target holder with diamond cell.



U445

Figure 100.62

Phase diagram of fluid hydrogen, with results from laser-shock measurements on precompressed samples (circles with error bars) and reverberating-shock experiments (triangle with error bar) constraining the onset of conducting behavior with increasing pressure and temperature (dashed curve). The solid line (dashed where extrapolated beyond the pressure range of experiments) represents the determination of the melting curve of hydrogen, and the green area is the envelope of Hugoniot curves spanning the range from cryogenic hydrogen to hydrogen initially at 5 GPa

transformation of high-pressure helium from an insulator to an electronic conductor was observed [as documented by optical properties (Fig. 100.66)], and it was discovered that there is a correlation between the transition from insulating to conducting fluid phases of hydrogen and the proposed maximum in the melt curve.

A summary of how the new equation-of-state, reflectance, and temperature data impact our fundamental understanding of hydrogen is shown in Fig. 100.62. The open symbols show where, in T-P space, hydrogen is becoming electrically conducting, $\sim 10^{19} e^-/cc$; the conductivity saturates at slightly high pressure-temperature conditions, suggesting carrier concen-

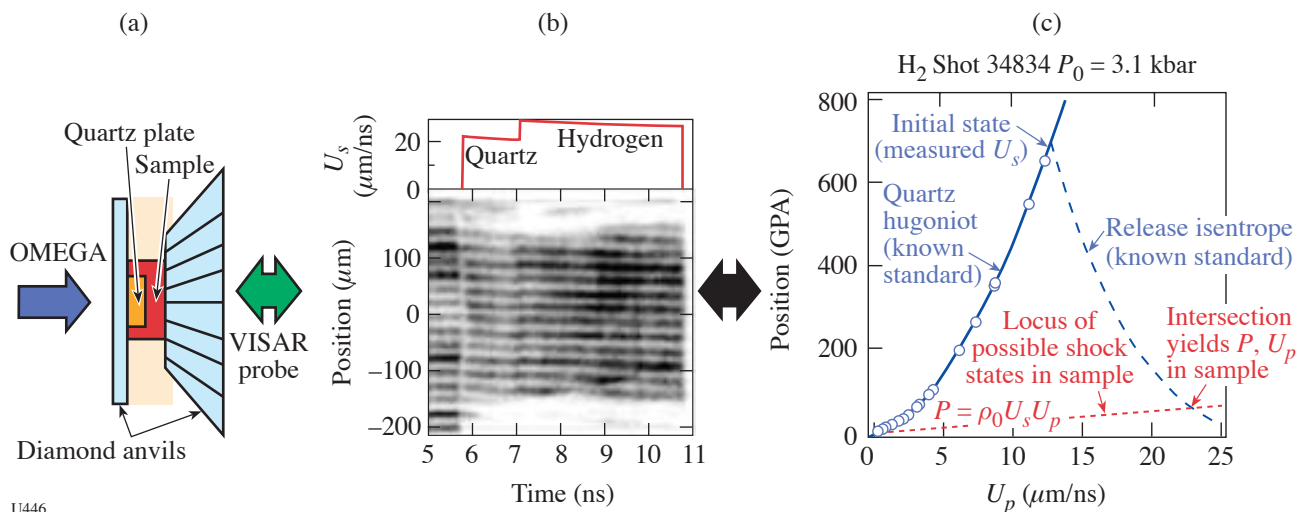


Figure 100.63

(a) Sketch of precompressed target, (b) sample VISAR record from precompressed H₂, and (c) example calculation for extracting pressure-density data. The beauty of this technique is that we observe the shock velocity in the quartz and the He or H₂ almost instantaneously, thus reducing much systematic and random uncertainties.

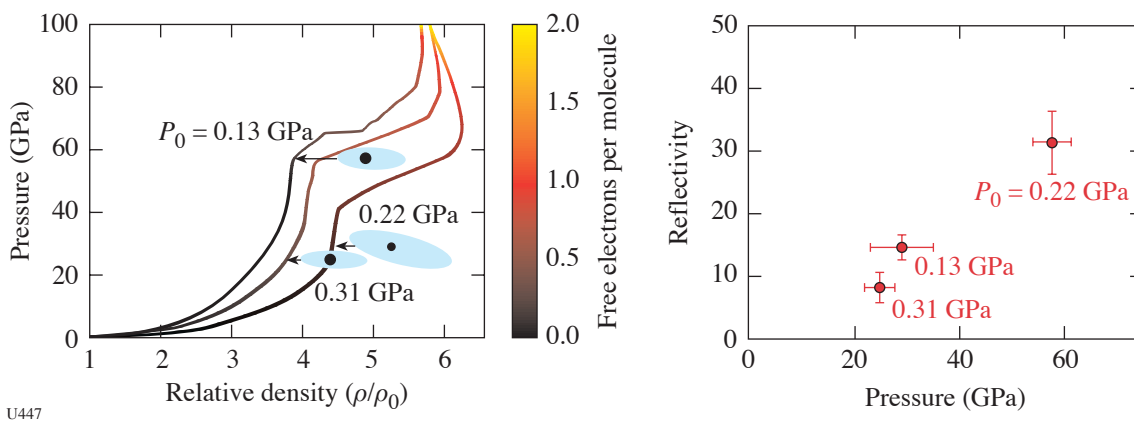
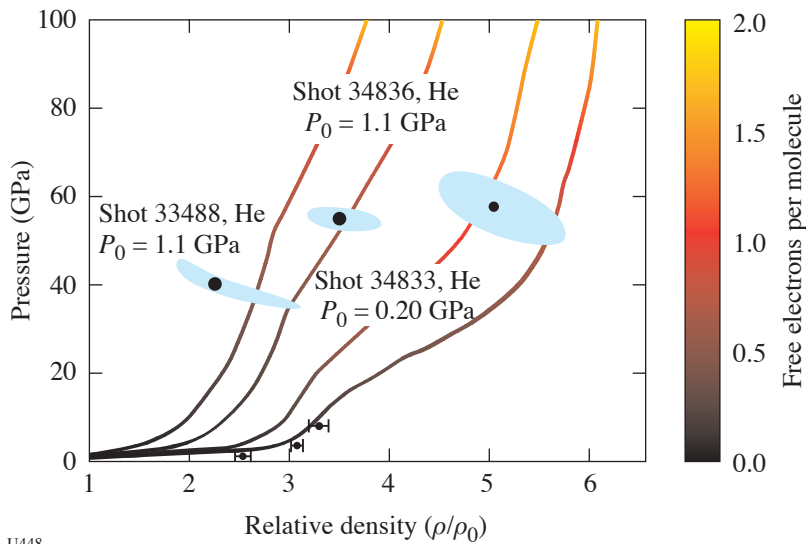


Figure 100.64

Measurements of shock density and optical reflectivity (532 nm) versus pressure for precompressed H₂.

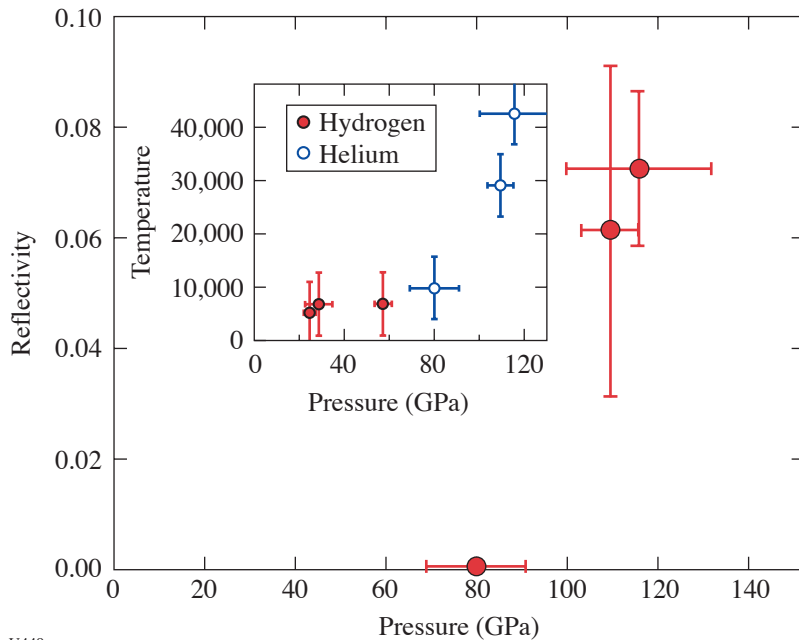
trations near $10^{23}e^-/cc$. The line connecting the open symbols is very close to the theoretically predicted plasma phase transition, which is interesting, since in materials (such as carbon) that have a first-order liquid-liquid transition there is a maximum in the melt curve, as appears to be the case for hydrogen.

Finally, note that this line also points to the single solid-state static experiment where conductivity is thought to be turning, or as evidenced by optical absorption above 310 GPa at 300 K. Each of these observations by itself is a notable result; all three represent a significant discovery.



U448

Figure 100.65
Pressure versus density shock-wave data for precompressed helium.



U449

Figure 100.66
Shock reflectance at 532 nm as a function of shock pressure for He, with the inset showing the measured temperatures versus shock pressure for both He and H₂ data summarized in Figs. 100.64 and 100.65.

Experimental and Modeling Studies of 2-D Core Gradients in OMEGA Implosions

Principal Investigator: R. C. Mancini (University of Nevada, Reno)

During FY04, time-resolved (gated, $\Delta t = 50$ ps) x-ray images of argon-doped implosion cores were recorded in OMEGA indirect-drive shots, based on line emission from He_{β} , Ly_{α} , and Ly_{β} line transitions in He- and H-like argon ions, respectively. Images were obtained simultaneously along two quasi-orthogonal directions [TIM2 and TIM3 line of sight (LOS)] with two Multi-Monochromatic Imager (MMI-3) instruments that record on framing cameras. Analysis of these image data permits the extraction of time-resolved information on the spatial distribution of temperature, density, and mixing in the implosion core. In turn, these results can be compared with a previous analysis done using time-integrated image data.

Figure 100.67 shows simultaneous He_{β} - and Ly_{β} -based x-ray-gated images of the implosion core recorded in OMEGA indirect-drive shot 36980 along the TIM2 LOS. These images are integrated over a time interval of 50 ps, close to the peak of x-ray emission. By implementing a generalized Abel inversion procedure, spatial distributions of line emissivity can be extracted from the data on several core slices perpendicular to the hohlraum axis and characterized by a coordinate along this axis. Analysis of these emissivity maps can be performed via a multi-objective search and reconstruction method driven by a genetic algorithm, and by an independent analytic method where temperature is extracted from emissivity ratio maps and density is subsequently determined from analysis of He_{β} and Ly_{β} emissivity maps. Figure 100.67 displays results for electron temperature and density radial distributions in a core slice through the hohlraum midplane. Additional information on spatial mixing profiles can also be obtained by looking at differences between relative intensity distributions in the data and those predicted by spectral modeling. These differences can be related to the amount of plastic mixed into the deuterium fuel and play an important role in the determination of the density profile. The temperature profile is relatively insensitive to this effect. Figure 100.67 displays this information in terms of γ , which is defined as the local ratio of plastic to fuel densities.

Work is in progress to include quantitative data from Ly_{α} images and to compare analysis results obtained along quasi-orthogonal LOS.

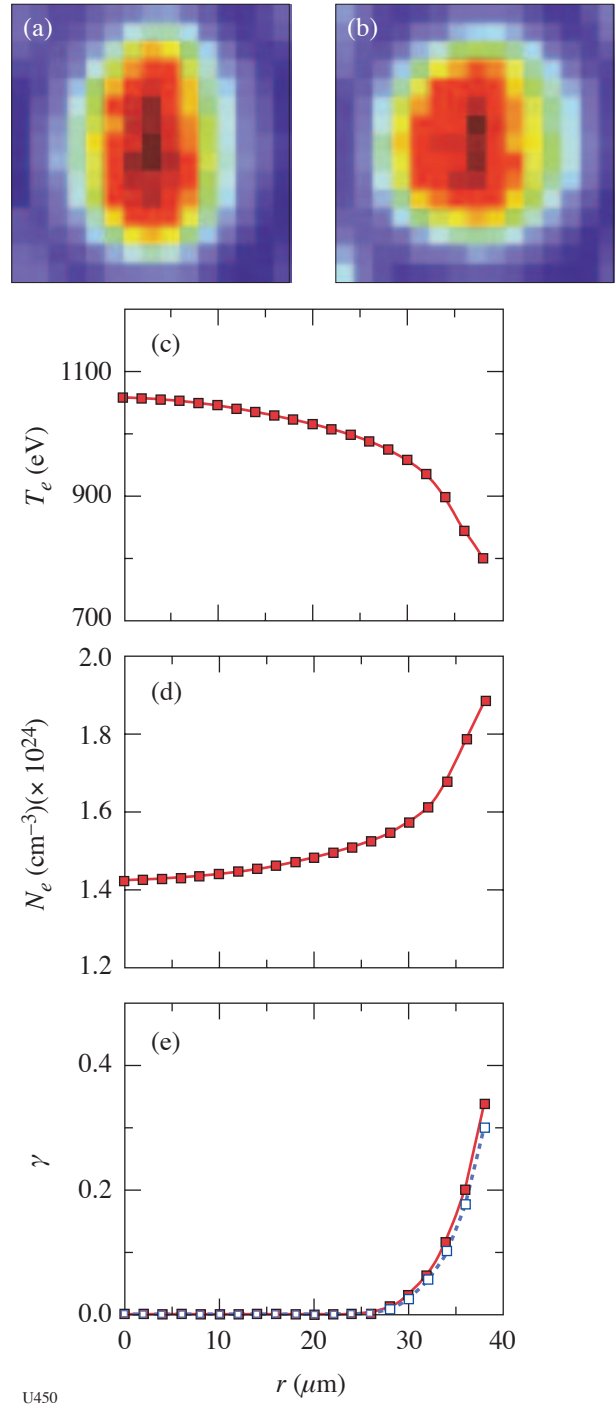
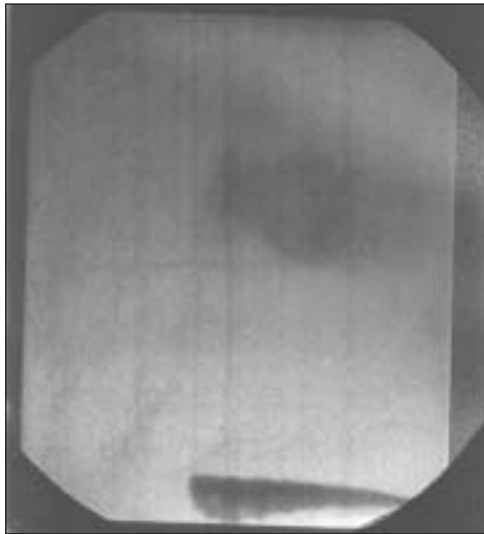


Figure 100.67 Simultaneous, time-resolved (gated, $\Delta t = 50$ ps) x-ray images based on argon He_{β} (a) and Ly_{β} (b) line emission from OMEGA indirect-drive shot 36980. The hohlraum axis is along the horizontal direction. Radial spatial distribution in the core's midplane (perpendicular to the hohlraum axis) of electron temperature (c) and density (d), and mixing of plastic into the fuel (e). Analysis assumes an isobaric core.

OMEGA Laser Studies of the Interaction of Supernova Blast Waves with Interstellar Clouds

Principal Investigator: C. F. McKee (University of California, Berkeley)

In the NLUF Astro experiment a planar shock is driven by the OMEGA laser inside a cylindrical shock tube. The shock passes by a sphere that is more dense than the surrounding material (by about a factor of 9). The sphere material is "crushed" and set in motion; it rolls up in a classical Kelvin–Helmholtz instability, then transitions to a fully 3-D flow through a Widnall instability. This experiment has been a pioneer in using backlit pinhole technology, and considerable efforts were made to make this technique work reliably (e.g., using tilted pinhole substrates, "destroyer beams," and target alignment using small corner reticles). By November 2003 the images could be obtained both reliably and with good signal-to-noise quality. Shots on 20 November were aimed at studying the shocked sphere material at late times (>60 ns after the start of the experiment), something that had never been done before. Experimental images (Fig. 100.68) showed sphere material being extensively shredded at these times, and by 80 ns the sphere material had reached the detectability limits



U451

Figure 100.68

Shocked sphere material 60 ns after the start of the experiment. Most of the sphere material makes up the bell-shaped object in the upper half of the image and has a volume more than 10 times larger than the original sphere (original sphere diameter 120 μm). Even with the high signal-to-noise ratio of the backlit pinhole technique, the sphere material is by this time quite diffuse; by 80 ns, it is no longer detectable. (The object in the lower half is a gold grid used as a spatial fiducial; one side of the image is approximately 1150 μm .)

for the very sensitive backlit pinhole technique, suggesting that the material is in a turbulent state by this time.

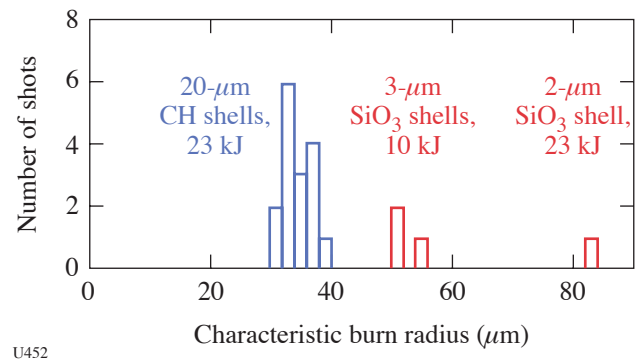
The NLUF Astro experiment was awarded 15 shots (one and a half shot-days) on OMEGA during FY2004. One half-day of shots was carried out successfully on 20 November, but a full day of shots planned for 15 April could not be taken since other targets were given higher priority at LLNL's target fabrication facility.

Time Evolution of Capsule ρR and Proton Emission Imaging of Core Structure

Principal Investigators: R. D. Petrasso and C. K. Li (Plasma Science and Fusion Center, MIT)

During FY04 penumbral proton imaging was used to study the spatial distributions of D-D and D- ^3He reactions in imploded D ^3He -filled capsules on OMEGA. The imaging was performed with multiple cameras in which the recorder consists of stacked sheets of CR-39 nuclear track detector separated by ranging filters that result in the efficient detection of 14.7-MeV D ^3He protons on one sheet and 3-MeV DD protons on another. The raw images were processed in two ways.

One approach was to assume that the emission distribution is spherical and to reconstruct a radial burn profile to study how the size of the burn region varies with capsule type and laser-illumination parameters. Figure 100.69 shows some data com-



U452

Figure 100.69

The sizes of the D ^3He burn regions in different types of implusions of D ^3He -filled capsules (all capsules have 18-atm gas fills, and all laser pulses utilized SG3 phase plates). The burn profiles are nearly Gaussian, and the size is characterized by the radius at which the emissivity is down from the central value by $1/e$. The thicker-CH-shell capsules implode with a higher convergence ratio than the thinner-SiO $_2$ -shell capsules, resulting in smaller burn radii. The data point at 82 μm was obtained from an implosion with 23 kJ of incident laser energy, while the other SiO $_2$ data points had approximately 10 kJ of incident laser energy.

paring capsules with thin glass shells to capsules with thick CH shells. The thin-glass capsules clearly have a larger burn region and indicate less radial convergence at burn time.

The other approach was to reconstruct two-dimensional (2-D) images of the surface brightness of the capsule. There are now three cameras on OMEGA that can be used to image capsules from three orthogonal directions simultaneously for symmetry studies. Data from each are then used to reconstruct a 2-D map of surface brightness, and the three separate images provide information about three-dimensional (3-D) burn asymmetries. To study the relationship between illumination asymmetry and burn asymmetry, an experiment was performed recently with laser drive containing intentional P2 asymmetry. Laser intensity was reduced at the two poles of a symmetry axis, with the result that the capsule imploded with a prolate ("sausage"-shaped) asymmetry. Figure 100.70 shows the resultant burn asymmetry, measured with three orthogonally oriented proton-emission imaging cameras; one camera viewed the end of the sausage while the other two viewed the sides. A substantial elongation of the emission region is seen, with a ratio of about 3:1 between the long and short axes. The direction of the elongation is coincident with the axis of the illumination asymmetry. In addition, the data suggest that the emission is peaked at the two ends of the region, resulting in a "dumbbell"-like shape.

FY04 LLNL OMEGA Experimental Program

Lawrence Livermore National Laboratory (LLNL) conducted 431 target shots on OMEGA in FY04. Approximately half of the shots were for the High-Energy-Density Science (HEDS) Program, and the other half were for inertial confinement fusion (ICF) experiments. The ICF experiments are summarized as follows:

A campaign was initiated to examine the effect on a capsule of direct hydrodynamic pressure from the laser-heated fill gas in gas-filled hohlraums. Initial results (Fig. 100.71) showed that the backlit foamball surrogate gave good results at fill pressures above and below those ultimately desired. (This series will continue in FY05.) The interaction of a hohlraum gas fill during the hydrodynamically unstable deceleration phase was also measured; no substantial instability growth was observed, even from deliberately pre-roughened hohlraum surfaces (Fig. 100.72).

In the area of x-ray drive, experiments were continued with hohlraums constructed of a mixture of materials ("cocktails"), in an effort to optimize x-ray conversion efficiency, albedo, and also laser-plasma coupling. Currently, it is believed that the consistently lower-than-expected improvement in radiation temperature for cocktail hohlraums is due to low-Z contaminants. Additional experiments were carried out to assess

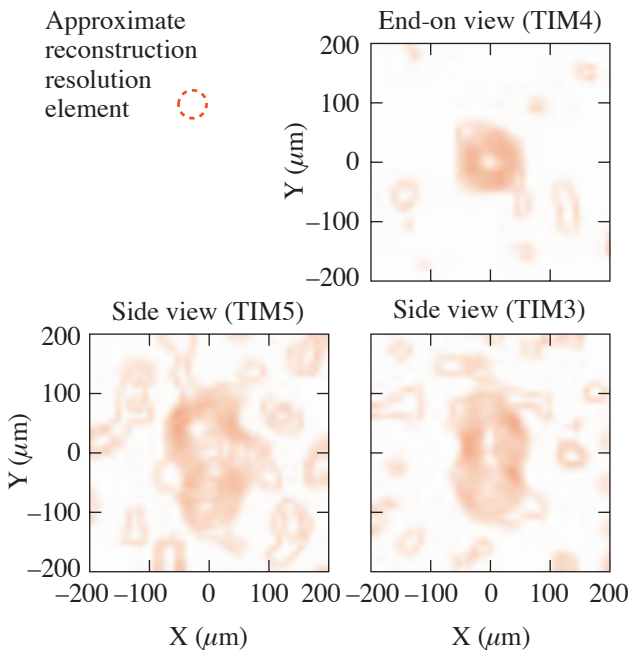
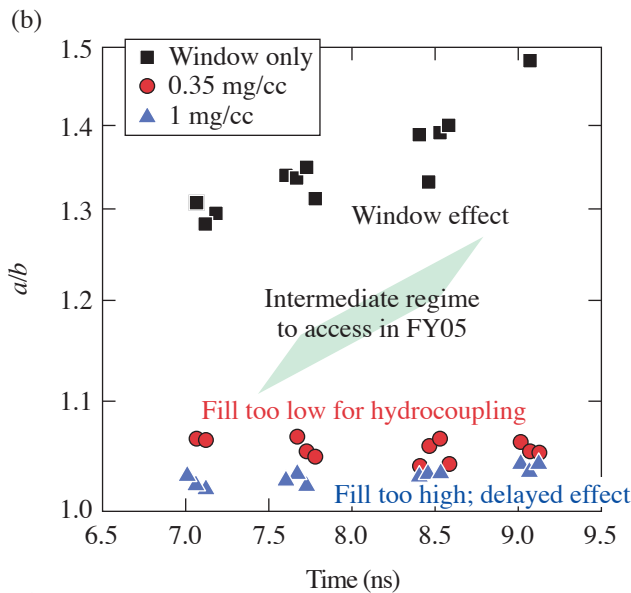
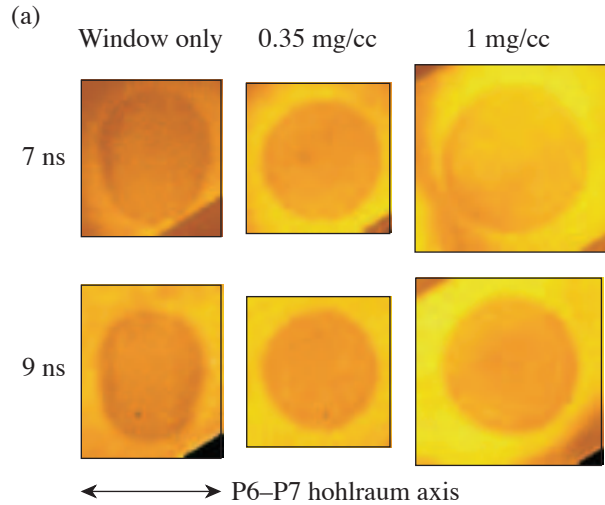


Figure 100.70
The first images of D^3He nuclear burn in an asymmetric implosion. These three contour plots show nearly orthogonal views of the fusion burn region in OMEGA implosions 35172 and 35173, recorded by three proton-emission cameras operating simultaneously (data from the two implosions are summed). The burn asymmetry had a prolate, or "sausage," shape, resulting from intentional asymmetry in the laser drive. The target capsules consisted of 20 atm of D^3He in 17- μm -thick CH shells, and the laser pulse delivered 17.5 kJ of on-target energy in a 1-ns square pulse. The laser intensity was lower than average in two directions 180° apart (on the TIM6-TIM4 axis), and the fusion burn is elongated in those directions. In the image reconstruction, bandwidth limitation for reducing noise resulted in an effective point-response function that is a Gaussian with $\sim 20\text{-}\mu\text{m}$ radius; the dashed circle thus indicates the approximate reconstruction resolution.

the performance of lined or foam-filled hohlraums as alternatives to the gas-filled National Ignition Facility (NIF) hohlraum point design. The early results are promising, showing radiation temperatures constant to within 5% between types of hohlraums and low levels of backscatter with smoothed beams at $5 \times 10^{14} \text{ W/cm}^2$.

Laser-plasma-interaction studies were done on large-scale-length plasmas created by preheating large gas-filled targets with the main laser (Fig. 100.73). Various experiments, some



U454

Figure 100.71

Backlit foam balls in CH (low-radiation)-gas-filled hohlraums are used to measure the gas-capsule hydrodynamic coupling. (a) Time-gated x-ray-backlit images of foam balls; (b) plot of foam-ball distortion versus time.

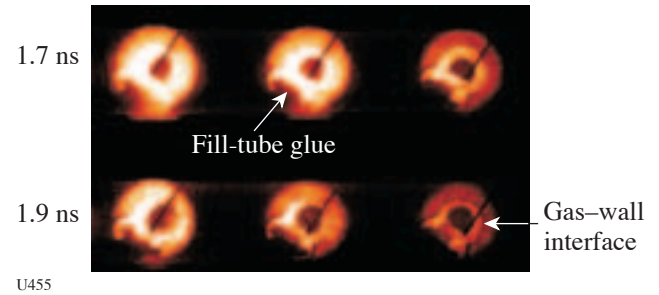
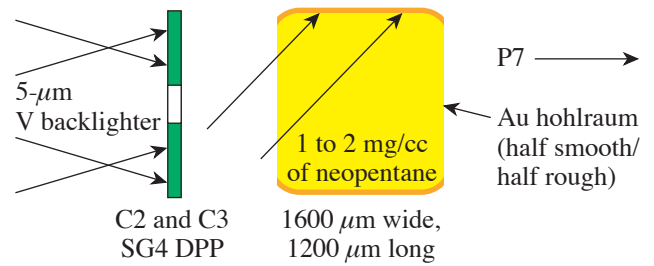


Figure 100.72

End-on view of an x-ray-backlit, gas-filled hohlraum shows wall motion and stagnation, with no signs of increased mix due to surface roughness.

using a 2ω or 4ω probe beam, were conducted to obtain data on stimulated Raman scattering (SRS), stimulated Brillouin scattering (SBS), and beam propagation (Fig. 100.74) as functions of beam-smoothing level. The results show reduced beam spray and backscatter by using increased smoothing on a 2ω probe beam. More crossing-beam power transfer experiments (a form of Brillouin scattering of special interest to the NIF) were performed as a function of polarization state (Fig. 100.75). Thomson scattering was used frequently to measure the electron temperature of these plasmas, while backscattered light (FABS) diagnostics monitored the amount of SBS or SRS. Still other experiments demonstrated the ability to measure the time-resolved spectrum of H- and He-like Ti (5-keV) x rays scattered by free electrons in a hot plasma; careful fits to the data yield temperature and density data (Fig. 100.76). Finally, a hohlraum experiment was conducted to quantify the amount of laser light that, at early times, is refracted from the hohlraum wall directly onto the implosion capsule.

Continued systematic improvements were made in using target-mounted pinholes to image implosion cores at moderately high ($>7\text{-keV}$) energies. Asymmetric core images were obtained at $87\times$ magnification, demonstrating a method for measuring higher-order (up to 6, possibly 8) mode structure in the hohlraum drive (Fig. 100.77).

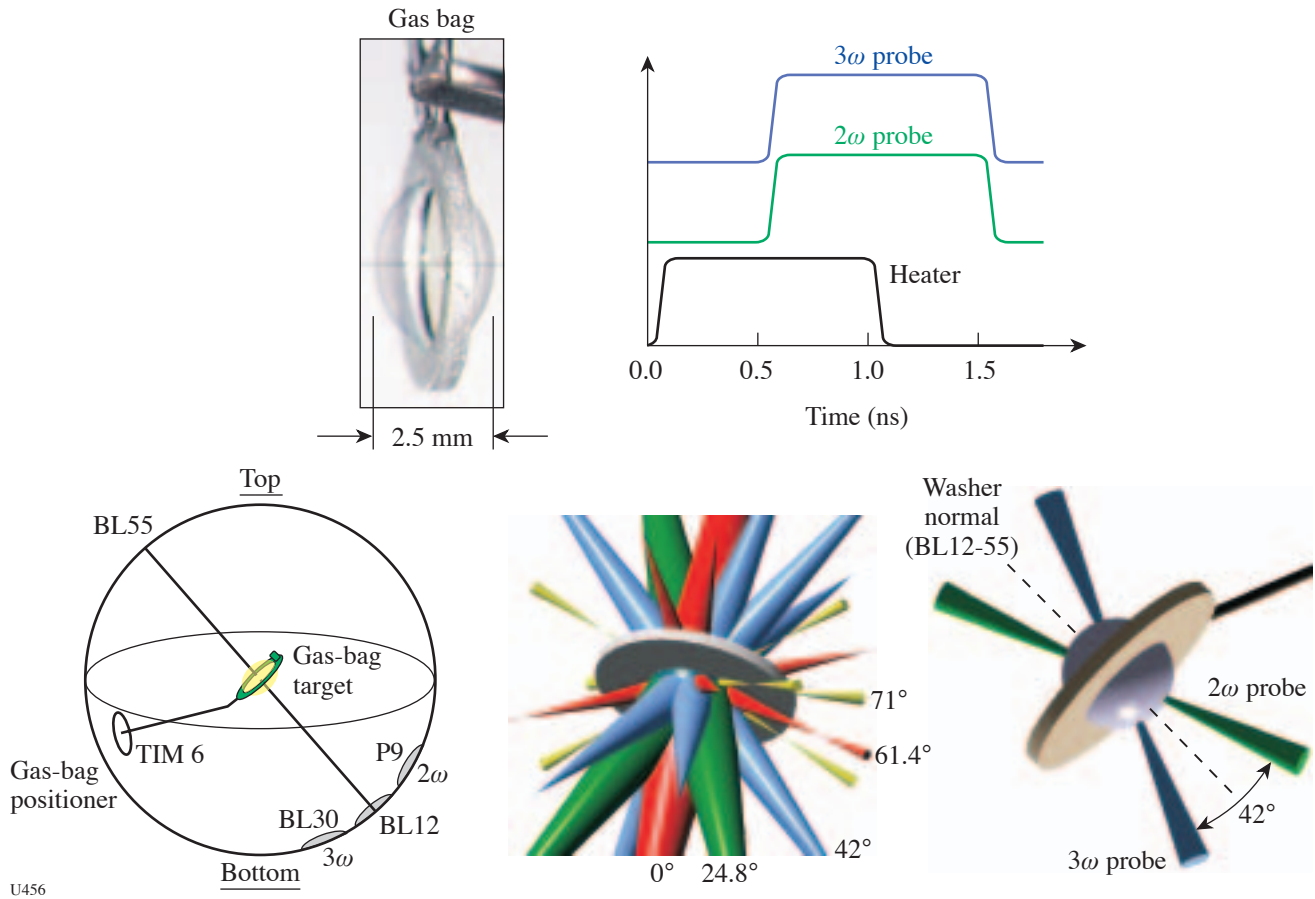


Figure 100.73
 The LLNL laser-plasma interaction studies in FY04 used gas-bag targets to form large, well-characterized plasmas. The diagrams illustrate the target configuration used in these experiments.

New data were obtained on integrated hohlraum implosions with deliberately roughened capsules (Fig. 100.77). These experiments were performed with convergence ratios (CR's) of 15 and provide a stringent test for modeling hydrodynamic instabilities. These same experiments demonstrated a small difference in drive asymmetry—which resulted in a degradation in neutron yield—if the presence or absence of polarization rotators was not accounted for in the laser pointing.

Ablator material studies, focusing on the Rayleigh–Taylor growth factors, continued in FY04 on polyimide and brominated plastic (Fig. 100.78). The results confirmed greater-than-expected RM growth for the thinner samples, but as-predicted RT growth rates (Fig. 100.79). A new more-NIF-

like, pulse-shaped, 2-D, symmetric, gas-filled halfraum experimental platform was designed for August 2004 shots. A first experiment was conducted to look at the effect of DT-fill tubes on an imploded capsule, using a deposited bump on the capsule as a surrogate for the fill tube.

Building on the work on hot hohlraums (see HEDS below), several implosion experiments were conducted using smaller-than-standard (3/4-size) hohlraums (Fig. 100.80). These represented the highest radiation-driven temperature implosions shot on laser facilities, reaching 275 to 285 eV, and producing symmetric cores. In some experiments DHe³ supplied by LLE was used as the fuel; DHe³ fusion proton yields and spectra were recorded and analyzed by MIT.

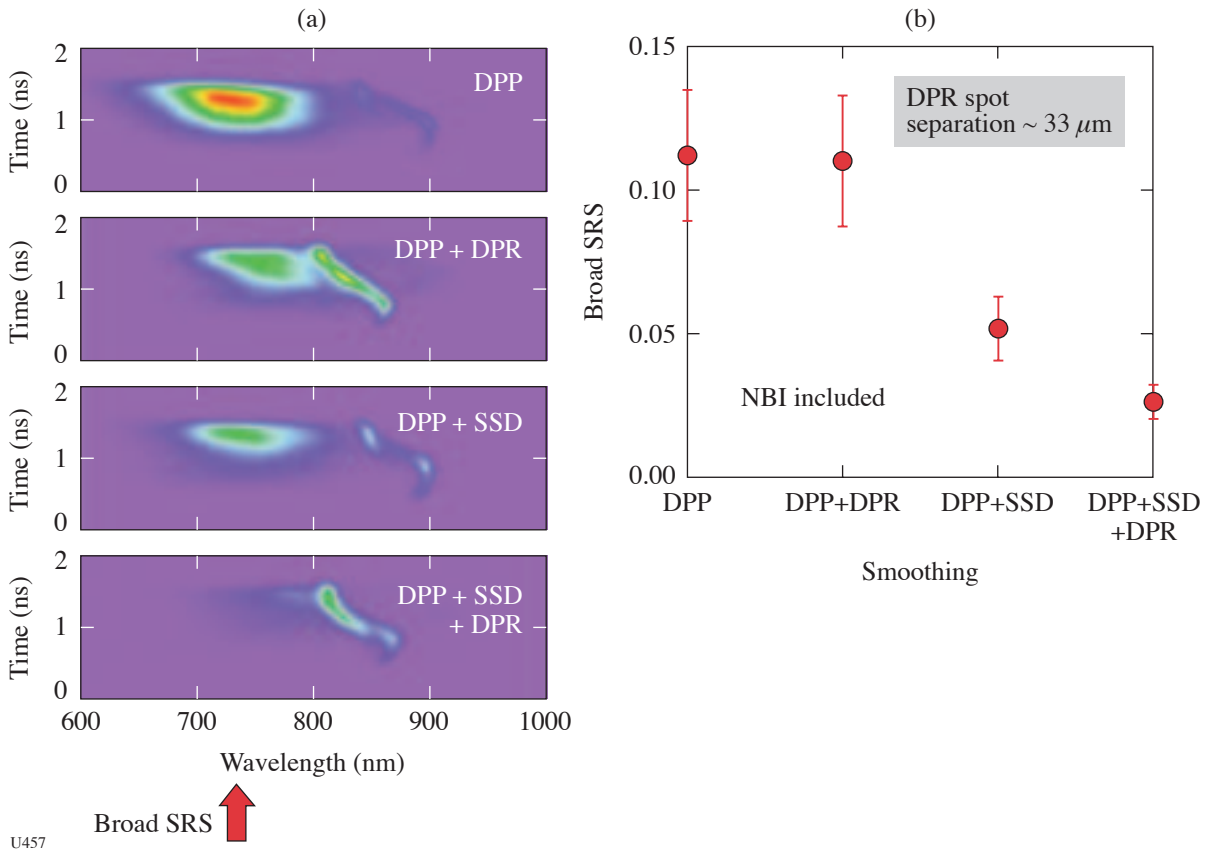


Figure 100.74

Laser-beam smoothing effectively reduces SRS in the low-density-plasma region. (a) Streaked SRS spectrum for four different laser irradiation beam-smoothing configurations. (b) Measured 2ω SRS scattered traction for the four different beam-smoothing configurations.

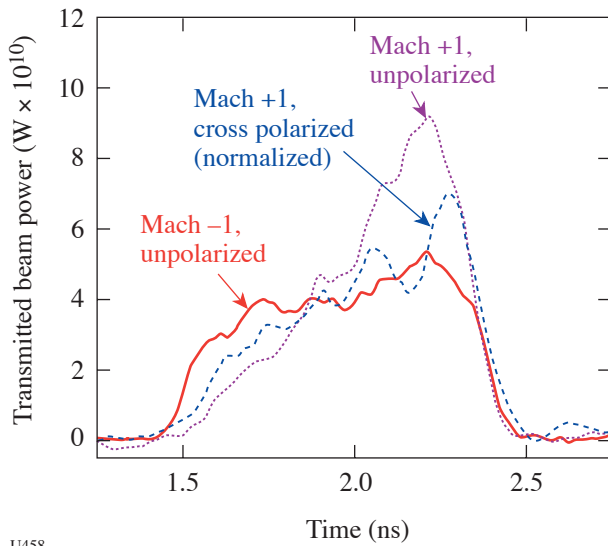


Figure 100.75

Crossed-beam experiments show energy transfer under the proper plasma flow conditions.

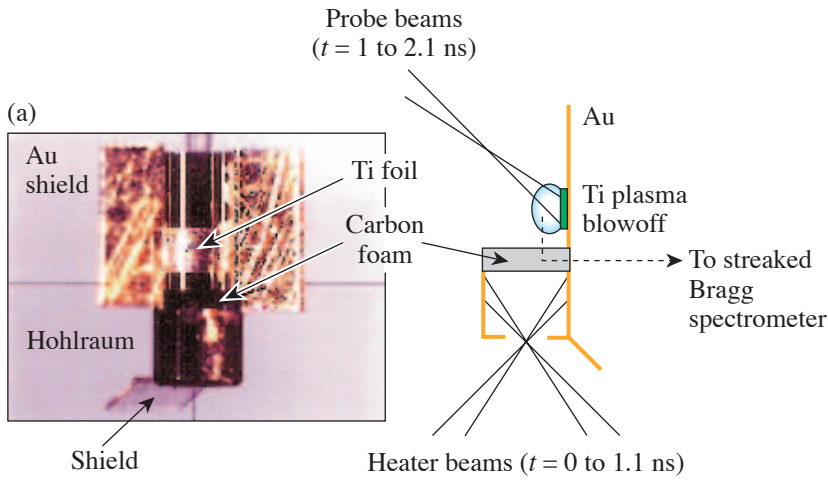
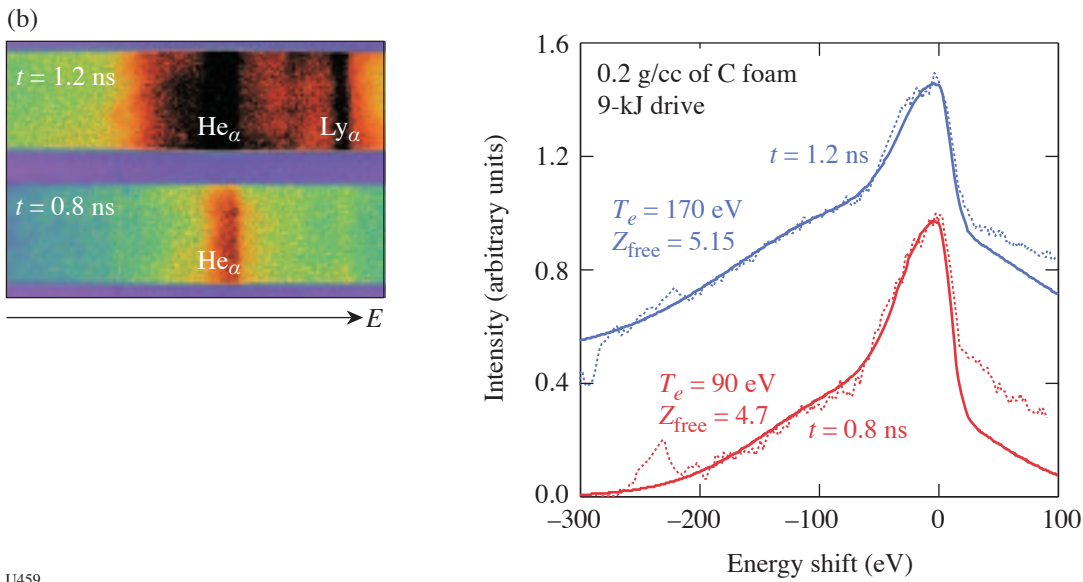


Figure 100.76 Compton-shifted scattered x rays are analyzed to obtain the electron temperature. (a) experimental configuration; (b) x-ray spectra from 0.2 g/cc-carbon foam at two different times during the irradiation.



U459

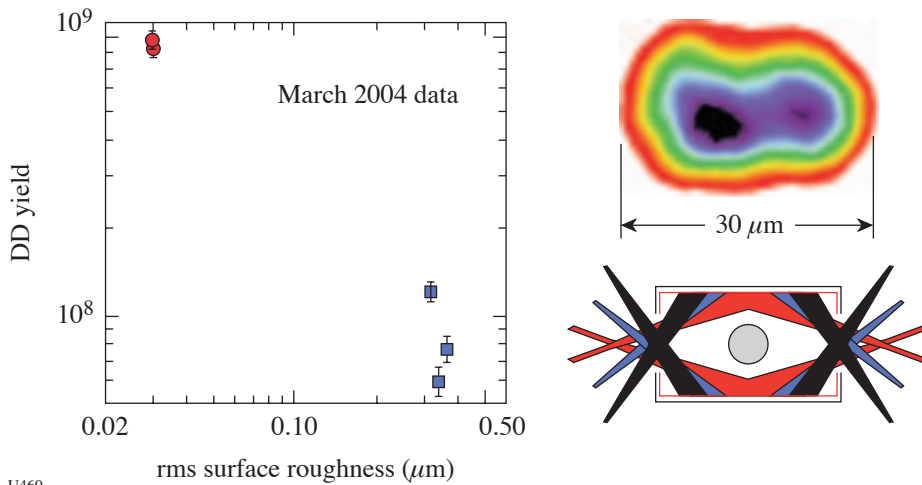
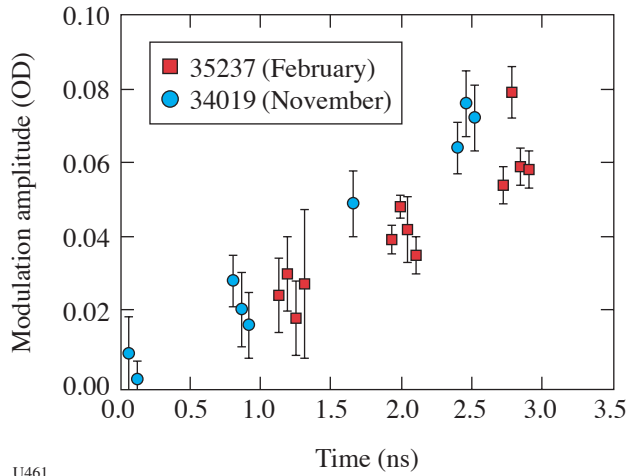


Figure 100.77 Neutron-yield degradation for implosions with a convergence ratio (CR) of 15 as a function of measured capsule-surface roughness. Also shown is a high-magnification x-ray image of an asymmetric imploded core, obtained at 8 keV.

U460



U461

Figure 100.78
FY04 OMEGA polyimide Rayleigh–Taylor experiments measured the growth rate of hydrodynamic instabilities.

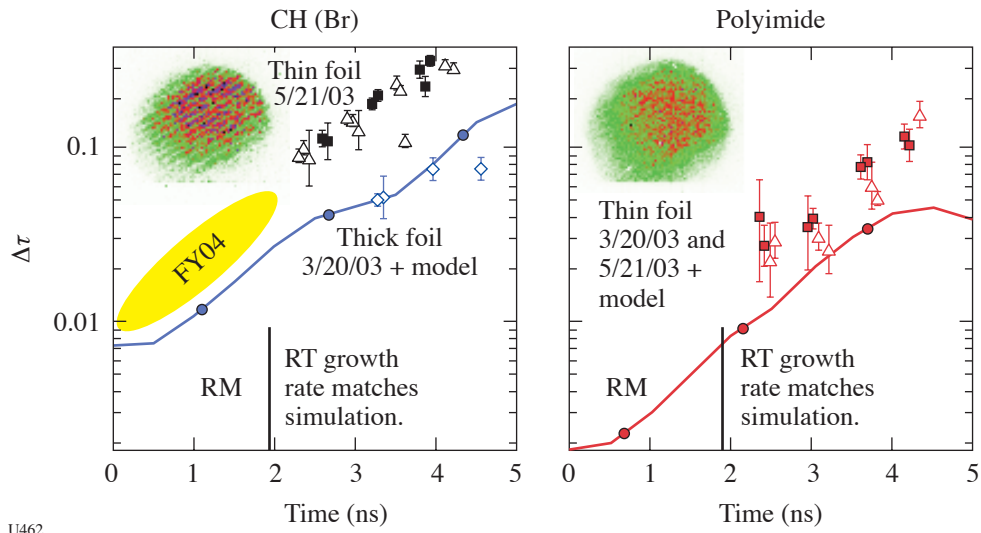
In collaboration with the University of Nevada, Reno (NLUF), multiple pinhole-imaged and spectrally dispersed data were obtained from indirectly driven, Ar-doped fuel implosions (Fig. 100.81).

Finally, several days of experiments were done in collaboration with LANL and LLE, using direct-drive, DT-filled targets, for the purpose of developing neutron diagnostics.

These relatively high-yield shots have indicated that significant background will be present for any diagnostics or electronics that are neutron sensitive.

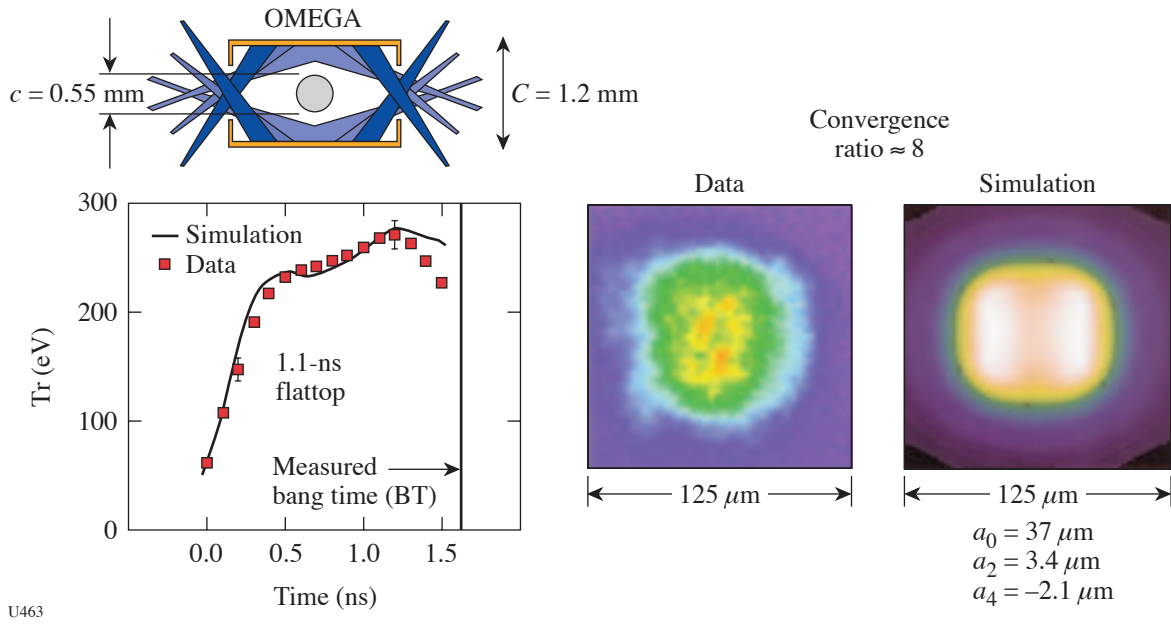
The other half of the LLNL shots were devoted to high-energy-density-science (HEDS)–relevant experiments. These are summarized as follows:

- Hot hohlraum experiments used hohlraums that were as small as possible to create as-high-as-possible radiation environments. Measurements were made on effective radiation temperature, high-energy (“suprathermal”) x rays, and laser–target coupling.
- Equation-of-state (EOS) experiments continued on OMEGA in FY04. These involved VISAR measurements of shock propagation times in various materials. Other experiments focused on creating and using an adiabatic (shockless) drive (Fig. 100.82) to smoothly ramp up the pressure for EOS measurements of solid (not melted) materials (Fig. 100.83). Finally, experiments done in collaboration with an NLUF investigator used gases that were precompressed in a diamond anvil cell to explore equations of state relevant to the giant planets.
- OMEGA shots were also used to explore various options for obtaining x-ray point backlighters. It is expected this knowledge will be used on future OMEGA and NIF shots.



U462

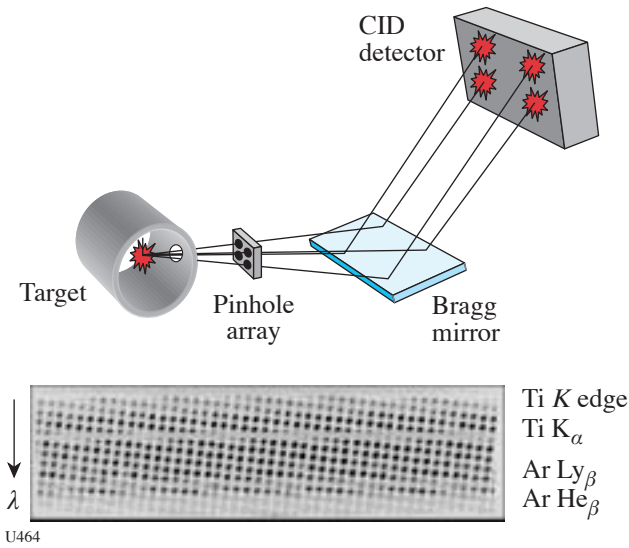
Figure 100.79
Plots of opacity versus time. The late-time data (~2 ns) show growth rates (slopes) consistent with the models, but a higher-than-expected growth during the early-time RM growth.



U463

Figure 100.80

Low-convergence-ratio implosions in small, high-temperature hohlraums were used to confirm basic drive symmetry.



U464

Figure 100.81

Geometry of spectrally dispersed imager used in NLUF experiments.

- A number of shots were devoted to studying alternative approaches to the standard indirect-drive concept of a simple hohlraum with a single-shell capsule. These included “dynamic hohlraums,” where a high-Z gas is directly driven and compressed and its resulting x rays are used to drive a second, concentric implosion capsule; and “double shells,” where the first driven shell collides with an inner shell, resulting in implosion velocity multiplication.
- The radiation flow campaign continued in FY04, focusing on x-ray propagation through low-density foams.
- A series of experiments were conducted to develop appropriate backlighter sources and detectors to measure the opacity of warm materials. The results of this campaign are expected to be used on experiments in FY05.
- LLNL continued a collaboration with LANL and AWE (United Kingdom) on the “Jets” experiments, looking at large-scale hydrodynamic features.
- Finally, shots onto gas-bag targets were conducted with various mid- to high-Z gases, in connection with developing x-ray sources (Fig. 100.84).

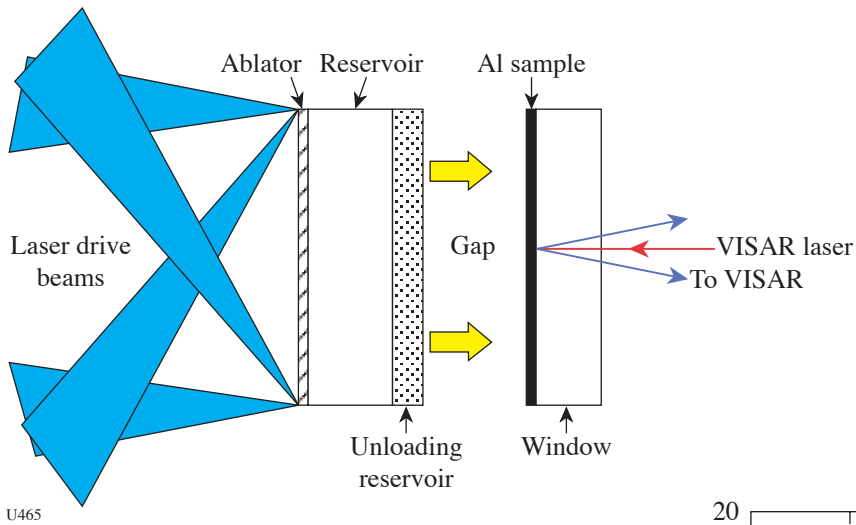
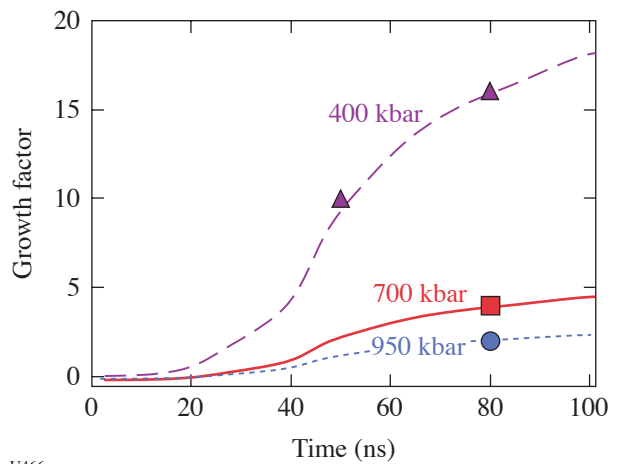


Figure 100.82
Experimental target setup used to produce smoothly increasing pressure drive for solid target physics.

U465

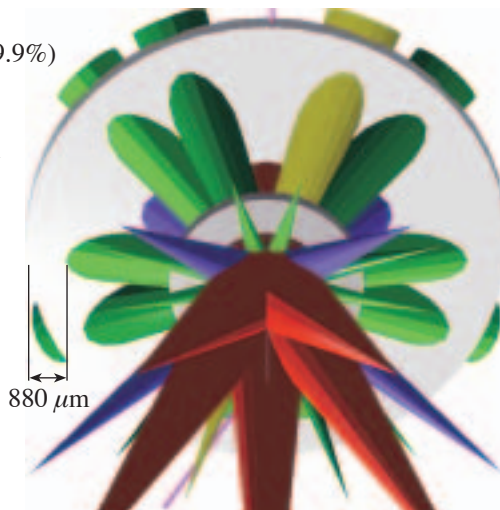
Figure 100.83
RT results for solid vanadium at three different pressures.



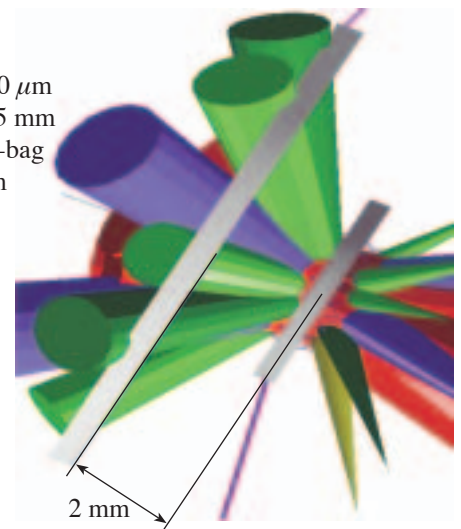
U466

Targets:

Gas bag
Ar (0.1%) + CH₄ (99.9%)
 $p = 0.5$ atm
Bag o.d.: 2.8 mm
Washer o.d.: 4.5 mm
Transmission: >30%



Stopper
CH foil
Thickness = 100 μ m
Diameter = 11.5 mm
Distance to gas-bag center = 2 mm



U467

Figure 100.84
Ar-doped gas-bag targets used to measure conversion efficiency to x rays.

FY04 LANL OMEGA Experimental Programs

Los Alamos National Laboratory (LANL) fielded a wide range of direct-drive-implosion experiments in both spherical and cylindrical geometries during FY04. The primary emphasis of these experiments was to measure mixing in convergent geometries to understand basic hydrodynamic behavior that will help validate our inertial confinement fusion (ICF) codes. Direct measurements of the stability of grainy Be were performed as part of the national effort to characterize ignition-capsule ablator materials. Collaborations with LLNL, LLE, and AWE are an important part of LANL's program on the OMEGA laser at LLE. The Astrophysical Jets experiment and the development of the Burn-History diagnostic were continued with these collaborating institutions. LANL also fielded its first experiments designed specifically as staging experiments for future execution on the NIF. LANL conducted a total of 168 target shots on OMEGA in FY04.

Time-Dependent Mix: The time-dependent evolution of mix was measured by imploding D_2 -filled, plastic ICF capsules. These capsules include a $0.1\text{-}\mu\text{m}$ -thick layer of titanium-doped plastic on the inside surface as a spectroscopic probe of the mix. Specifically, mixing of titanium into the D_2 fuel greatly enhances the intensity of the hydrogen-like Ti α line relative to the helium-like Ti α line because high temperatures consistent with the imploded fuel core (>2.5 keV) are required to populate the upper state of the hydrogen-like Ti α line. Therefore, the time evolution of the intensity ratio of the hydrogen-like Ti α line to the helium-like Ti α line is a strong indicator of the amount and timing of shell material mixing into the hot-core region of the fuel. The experimentally measured intensity ratio was up to 50% larger than that predicted by the simulations. This intensity ratio suggests that more mix is occurring in the center of the fuel region than that predicted by the mix model used in the simulation. We cannot, however, be certain of this because the simulations also predict lower temperatures than those measured by neutron time-of-flight data. The cause of the temperature discrepancy is still an open question that is being investigated.

In addition to spectral line information from the titanium, time-resolved spectroscopic measurements, data from x-ray time-gated-imaging diagnostics and neutron-yield diagnostics were also used as indicators of the level and timing of mix occurring within the imploding capsules. The gated x-ray images showed that even at the earliest time possible, near when the reflected shock first reaches the ablator and about 150 ps before peak burn, the images are not limb-brightened, but instead have a flat profile that later becomes centrally

peaked. This profile indicates substantial mix at a time when other experiments have suggested little and backs up the observations in the intensity ratio of the α lines. Unfortunately, only a few images were obtained at times of interest near the burn with the x-ray framing cameras. The images showed indications useful for unique timing in future experiments (such as the outward expansion of the shock after peak burn, faint interference by gamma rays at peak burn, and the sudden brightening when the reflected shock first reaches the pusher layer).

Time-gated images (Fig. 100.85) show the full time history of the implosion with an interstrip time of 700 ps. The first strip shows the initial capsule size, the second strip shows the capsule imploding, the third strip shows the effect of the neutron emission at the implosion time, and the fourth strip shows an outgoing shock after the implosion.

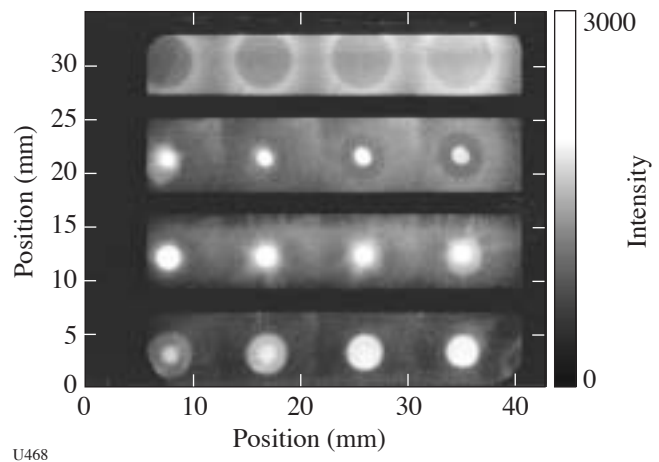


Figure 100.85

Time-gated x-ray images of a single capsule experiment showing both the implosion and explosion phases. Time runs from right to left and top to bottom.

Double-Shell Implosions: Imploding double-shell targets may provide an alternative, noncryogenic path to ignition on the NIF. Experiments are being pursued on OMEGA to understand the hydrodynamics of these implosions and the possibility of scaling to NIF designs. One line of inquiry this year measured the effect of foam structure on neutron yield. Carbon resorcinol foam [$C_6H_6O_2$], with cell sizes of a few nanometers, was used instead of the normal plastic foam with micron-size cells. Sixty beams with direct-drive symmetry imploded the capsules. As predicted, the smaller pores gave a measurably higher yield.

In other experiments, the zero-order hydrodynamic motion of the two shells was measured using a unique implosion scheme. Forty OMEGA beams were pointed at calculated offset distances from the center—not at the center of the capsule. The other 20 beams created two 6.7-keV backlighter sources to radiograph the shell locations. The use of a sulfur-doped CH marker layer allowed measurement of the implosion with good contrast. Four goals were attained: First, the implosion hydrodynamics were measured by backlit imaging. Radiography from two simultaneous directions was used to image and measure the hydrodynamics of capsules that were optically thin to the x rays from the backlighters at 6.7 keV. Second, neutron yield and x-ray emission were used to measure the output from the thicker capsules with two different foam compositions to assess the effect of foam cell sizes on the implosion. The carbon resorcinol foam was found to increase the yield, as in the 60-beam shots, but the early results indicate little observable effect on the hydrodynamic behavior. Third, investigations were carried out to find out whether a thin layer of plastic overcoat would help separate the effect of absorption at the seam of the outer capsule from the seam hydrodynamics. However, the target quality was not good enough to allow the observation of a measurable difference. Fourth, the radius versus time of the sulfur marker layer was measured for the implosion of Au-coated and uncoated targets to determine the difference in the implosion due to the gold *M*-band x rays that exist in some of the NIF-design ICF capsules. The results were in good agreement with one-dimensional simulations (Fig. 100.86) although little difference was observed between the coated and uncoated targets.

Burn-History Diagnostic Development: In collaboration with LLNL, LANL continued to develop diagnostics that record the temporal behavior of the fusion burn. Gamma rays are a by-product of the deuterium–tritium (D-T) reaction. Using our two Gas Cerenkov Detectors (GCD's) (Fig. 100.87), these gamma rays are converted to relativistic electrons that emit Cerenkov radiation, which is then recorded. The prototype instrument, GCD1, records the emission using a photomultiplier tube and fast oscilloscope. The newer instrument, GCD2, records the information with higher time resolution using a streak camera.

During high-neutron-yield DT and deuterium–deuterium (DD) experiments conducted by LLE, both the GCD's and the LLE Neutron Temporal Detector were successfully operated simultaneously for the first time. Much cleaner and stronger signals were obtained with the streaked GCD2 (Fig. 100.88). These higher-quality signals allowed a GCD2 sweep rate of

10× for the gamma-burn signal. Quality GCD1 results were also obtained for most implosions.

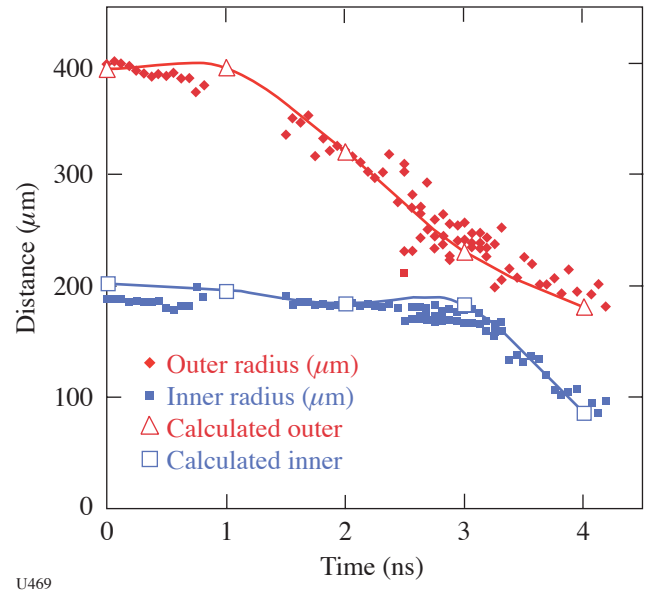


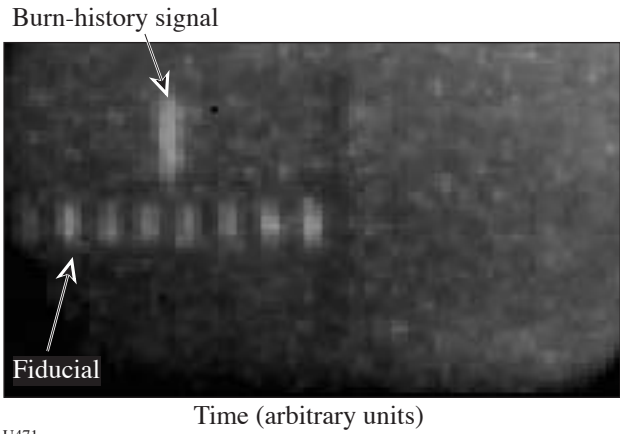
Figure 100.86

The temporal behavior of the outer and inner shells shows the momentum transfer between the two shells at about 3 ns. One-dimensional simulations are in good agreement with the measurements.



Figure 100.87

The GCD pressure cell and light-collecting optics are shown without the streak camera recording system.



U471

Figure 100.88
The time-resolved burn-history signal from a high-yield implosion demonstrated a 280-ps time resolution.

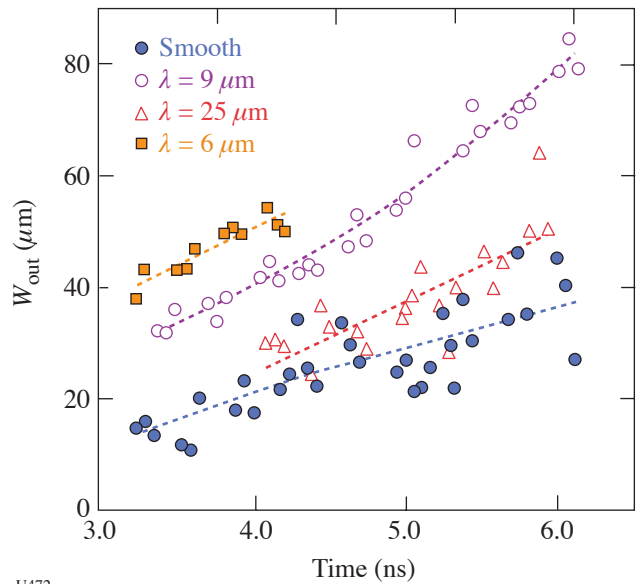
The feasibility of simultaneously recording a fusion gamma ray and fusion neutron signals using both the GCD1 and GCD2 was also successfully demonstrated; this simultaneous recording is an essential step in establishing the feasibility of a dual-mode capability in a single diagnostic. This recording was accomplished by placing either fused-silica glass or lead glass behind the normal converter foil and producing a gas Cerenkov signal and a glass Cerenkov signal on any given implosion. The neutron-burn signal was strong enough to allow a GCD2 sweep rate of 3x.

Beryllium Ablator Microstructure Stability (BAMS): An LANL goal is to deliver a specification for the microstructure of ignition-capsule ablators to the National ICF Program. The current focus is on beryllium-copper ablators, but other materials may be investigated as well.

LANL experiments make VISAR observations of ~1-Mbar shock waves in beryllium-copper samples, DANTE measurements of hohlraum temperature (verifying 6-ns-long composite pulses from OMEGA), x radiography of perturbations in samples, and characterization of the spectra from aluminum backlighters. In addition, LANL scientists also successfully recorded backlit (“side-lit”) x radiographs of beryllium-copper samples viewed from the side, allowing a determination of the trajectory of the samples’ motions. This permits one to make inferences about the radiation drive accelerating the samples, independent of the DANTE and VISAR data.

Another experimental series returned time-dependent data of the emission spectra of aluminum backlighters typical of those used in radiography of beryllium-copper samples. The relative contribution of line and continuum radiation was measured as a function of incident laser intensity to improve the contrast in our radiographs of intentionally perturbed samples and eventually in future radiographs of microstructure-perturbed samples.

Cylinder Implosion: Significant progress was made toward understanding the effect of convergence on shock-driven instability growth [Richtmyer-Meshkov (RM) instability] and initiated experiments that address variable acceleration (Rayleigh-Taylor) instability growth. Both types of instability can adversely affect ICF capsule implosions. High-quality data were also acquired on re-shock of already developing mix layers and defect-shell interactions. The primary effect of convergence on the single-mode RM instability is to postpone or suppress the growth of secondary instabilities resulting in an extended period of linear growth, well beyond that expected and observed in planar geometry.² The linear growth for several sinusoidal initial perturbations is shown in Fig. 100.89. Approximate linear growth is observed for amplitude-over-wavelength ratios as large as 4. The mechanism(s) responsible for the observed behavior has not been identified; however,



U472

Figure 100.89
The growth of the mix layer width W_{out} for sinusoidal perturbations with an initial amplitude of 2 μm varies with the wavelength of the perturbations.

the apparent postponement of saturation is a dramatic example of the effect of convergence. To date, comparisons with computational (*RAGE*)³ results have yielded qualitative agreement, but quantitative differences are still being addressed. The transition to turbulent mixing for short-wavelength ($\lambda \leq 2.5\text{-}\mu\text{m}$), multimode perturbations was also identified. Again, the apparent effect of convergence is to prolong linear growth for extended periods rather than the power-law-growth behavior observed in planar geometry. The short-wavelength results are being used to verify and validate the BHR model⁴ in *RAGE* and to provide guidance in implementing crenulative (convergence) effects in the BHR turbulence model.

Off-Hugoniot Stability: The initial proof-of-principal experiments for the Off-Hugoniot Stability project were conducted this year. The goals of the integrated experiments were

to evaluate whether radiography provides sufficient resolution of interface locations and to demonstrate that sufficient heating can be applied to generate hydrodynamic motion. The wedge experiments were designed to characterize the tin pre-heat source. Two experimental packages were employed: an integrated target [Figs. 100.90(a) and 100.90(b)] and a wedge target [Fig. 100.90(c)].

Both target types returned data that surpassed expectations. Five shots using integrated targets successfully captured the temporal expansion of the heated epoxy into the foam. Measurements were made at 2, 3, 4, 6, and 8 ns after the heating drive beams turned off. Figure 100.91(a) shows the epoxy layer at 3 ns with a final resolution between 15 and 20 μm , confirming that the experimental design provides sufficient measurement accuracy to meet the physics objectives of the campaign.

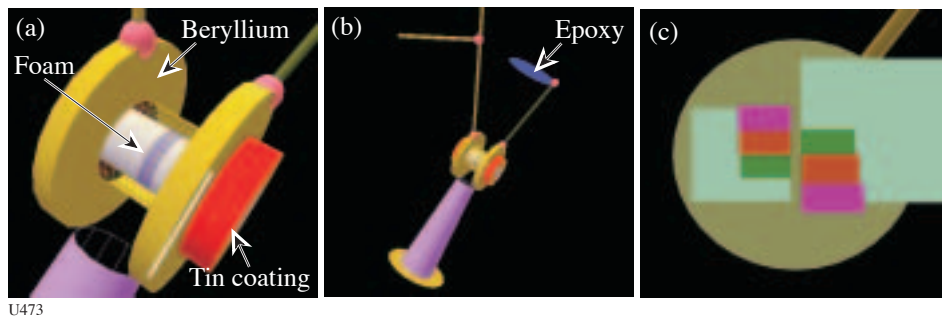


Figure 100.90
 (a) The integrated target consists of a beryllium assembly, stuffed with epoxy and foam layers. A thin coating of tin is directly driven by 33 beams to produce *L*-shell emission that heats the package. (b) The integrated target showing backlighter foil and view shield. (c) The wedge target measures the transmission of tin *L*-shell emission through wedges of epoxy and beryllium and facilitates an accurate measure of the *L*-shell-emitted flux.

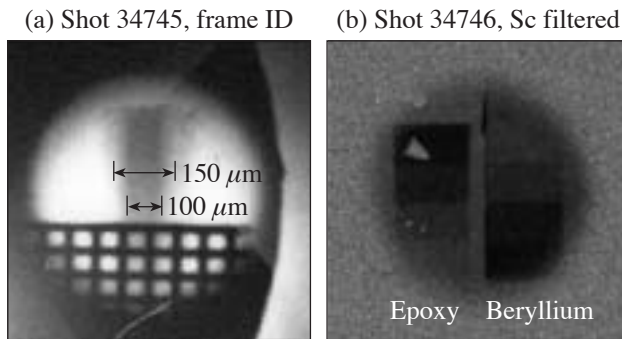


Figure 100.91
 (a) Radiograph of the epoxy layer 3 ns after the start of tin *L*-shell preheat. At this time, only 60% of the epoxy is still near full density. (b) The flat-field transmission of tin *L*-shell emission through the epoxy (left) and beryllium (right) wedges.

In addition to the success of the integrated experiments, the wedge targets along with extensive spectroscopic measurements were very effective at characterizing both the spectral nature and conversion efficiency of the tin *L*-shell emission. Figure 100.91(b) shows the tin *L*-shell transmission through characterized epoxy and beryllium wedges. These data suggest that about 2% to 5% of ultraviolet laser energy on target is converted to the tin *L* shell.

Astrophysical Jets: The jet project is a collaboration between LANL, AWE, and LLNL designed to verify and validate turbulence models for astrophysical simulations in our radiation-hydrodynamic codes. The jet target consists of a titanium foil mounted to a washer. A low-density, 0.12-g/cm³, resorcinol-formaldehyde (RF) foam is mounted to the rear side of the titanium washer. The laser beams strike the titanium foil and drive a titanium jet into the foam. The primary diagnostic is x radiography of the titanium jet in the foam.

High-quality radiographs using new noise-mitigation techniques were obtained. These measurements included placing a 4- μ m-thick CH coating on the drive side of the titanium foil. In addition, a large gold shield was mounted to the front of the target that prevented x rays from the coronal plasma created by irradiating the titanium foil from reaching the x-ray detector. The background problems of the past were reduced with a new "spot-backlighter" design of a small square (200 μ m) of vanadium, surrounded by CH. The low-atomic-number (low-*Z*) plasma that is created by the backlighter laser beams helps contain the vanadium blowoff and reduces the spatial extent of the high-energy background. The backlighter images the target orthogonally to the direction of jet propagation.

The temporal evolution of the jet was captured at three different times. The result from one of these times, 400 ns after the laser drive, is shown in Fig. 100.92(a). There is a great level of detail in the image. For example, refractive effects are observed at the bow shock edge [Fig. 100.92(b)] and also mixing between the titanium and the RF foam is apparent in Fig. 100.92(c).

Hohlraum Filling: Experiments on the NIF will use much more energy to heat a hohlraum of approximately the same size as an OMEGA hohlraum. An important constraint on the NIF experiments is how long the material will have to evolve before the hohlraum fills with gold from the wall of the hohlraum itself. A short series of experiments determined the amount of wall material influx in a hohlraum experiment

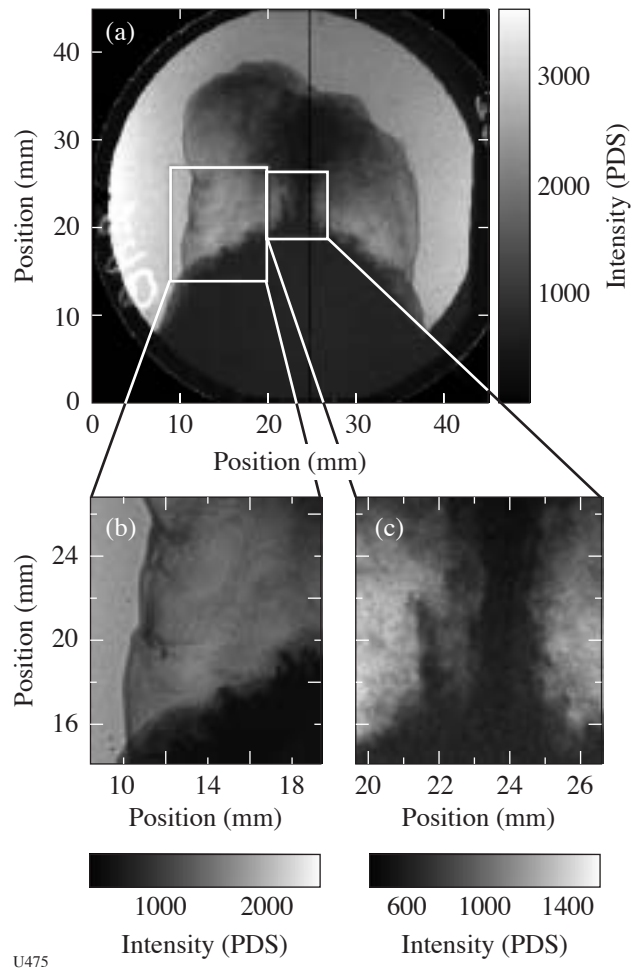
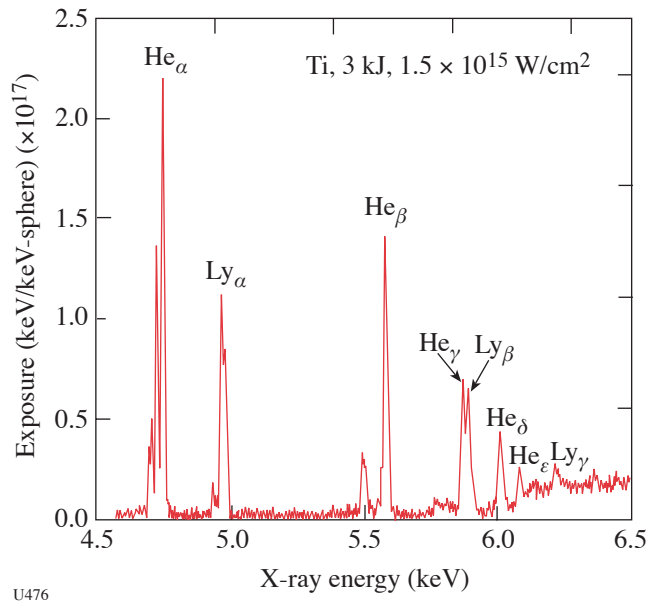


Figure 100.92
 (a) Radiograph of the jet at 400 ns, magnified by a factor of 12. The jet stem is well collimated. The base (or pedestal) of the jet shows signs of hydrodynamic-instability growth. (b) Detail of the image showing the edge of the bow shock. Refractive enhancement of the bow shock is seen. (c) Detail of the jet stem showing the mixing between the titanium and the RF foam due to the Kelvin-Helmholtz instability.

and the effect of mitigation techniques on the radiation temperature achieved.⁵

It was found that coating the inner surface of the hohlraum with a 0.5- μ m-thick layer of parylene would inhibit the amount of gold reaching the center of the hohlraum while decreasing the radiation temperature by only about 10 eV. Further experiments, however, showed that the number of hot electrons produced via laser-plasma interactions increased tremendously as measured by the level of hard x rays measured.

Backlighter Yield Measurements: The conversion efficiency of laser light into x-ray energy from titanium- and zinc-flat-disk targets was measured. These experiments were accomplished in half-day increments due to the simplicity of their configuration. Six drive beams illuminated the flat disks from one side using 1-ns square pulses. The number of beams and the focal-spot diameter were varied to produce orders-of-magnitude changes in the laser-irradiance conditions. Measurements were taken with framing cameras, streak cameras, and static pinhole cameras; however, the primary diagnostic was the Henway spectrometer [a time-integrated, x-ray-film-based survey spectrometer (Fig. 100.93)]. Every shot produced high-quality data that are currently being analyzed to determine the scaling of x-ray conversion efficiency as a function of laser irradiance. These results will be used to develop and refine area and point-backlighter configurations for OMEGA and future NIF experiments.



U476

Figure 100.93

Example of data taken with the Henway spectrometer of the emission from a flat titanium target. Signals will be integrated over the helium- α emission line to determine conversion efficiency into bright line emission for future backlighter configurations.

FY04 SNL OMEGA PROGRAMS

SNL carried out 31 target shots on the OMEGA laser in FY04 and also participated in several of the campaigns led by other laboratories. The SNL-led campaigns included the following:

Modification of a Laser Hohraum Spectrum via a Mid-Z Wall Liner: A typical laser hohlraum has a radiation spectrum that includes a significant component of non-Planckian, high-energy photons (such as Au *M*-band x rays) that originate in and near the hot, low-density coronal plasma in which the laser light is absorbed and converted into x rays. These hard x rays can have undesirable effects for an ICF application, such as causing preheat ahead of the shock front in the ablator of an indirect-drive capsule.⁶ One concept for tailoring the spectrum in a hohlraum is to employ a thin, mid-*Z* liner to supply plasma for the x-ray conversion, with an underlying high-*Z* wall for x-ray containment. In a recent series of laser hohlraum experiments performed on OMEGA, this concept was demonstrated by employing a thin (0.5- μm) Cu liner on the interior of an Au-walled hohlraum to significantly soften the radiation spectrum and yet retain the peak hohlraum temperature of a standard Au hohlraum. As shown in Fig. 100.94(c) and 100.94(d), this successful result was evident in the data from the DANTE array of *K*- and *L*-edge filtered x-ray photocathodes.⁷ A 280-nm Streaked Optical Pyrometer⁸ was used to confirm that the preheat ahead of the shock front in a CH ablator was significantly reduced when using the Cu-lined hohlraum, as compared to an ordinary hohlraum [Fig. 100.94(b)].

The Effectiveness of Mid-*Z* Dopants in Reducing Preheat in Indirect-Drive ICF Ablator Materials: In previous work,^{6,9} we experimentally verified that mid-*Z* dopants can be used to significantly reduce preheat and shock temperature in low-*Z*, indirect-drive ICF ablator materials. The previous experiments with Ge-doped CH ablaters were done with dopant concentrations of 2% (atomic) Ge. As shown in Fig. 100.95, FY04 experiments have demonstrated that a significantly lower dopant concentration (0.5% atomic Ge in CH) can also be effective for reducing shock temperatures and preheat levels in indirect-drive ablaters.

Long-Pulse Au Hohraum Wall Albedo Measurements: In previous work,¹⁰ measurements of absolute hohlraum wall albedos for ignition foot drive temperatures were made for pulse lengths of up to 1.5 ns. In FY04, we began work to extend the albedo measurements to longer pulse lengths and achieved albedo measurements for pulse lengths of ~ 3 ns. Two experimental arrangements were used in the long-pulse albedo experiments: a secondary hohlraum driven by x rays from a single primary hohlraum [Fig. 100.96(a)], and a secondary hohlraum driven by x rays from two primary hohlraums [Fig. 100.96(b)]. The secondary hohlraum temperature history is shown in Fig. 100.97(a), and the new extension of the Au

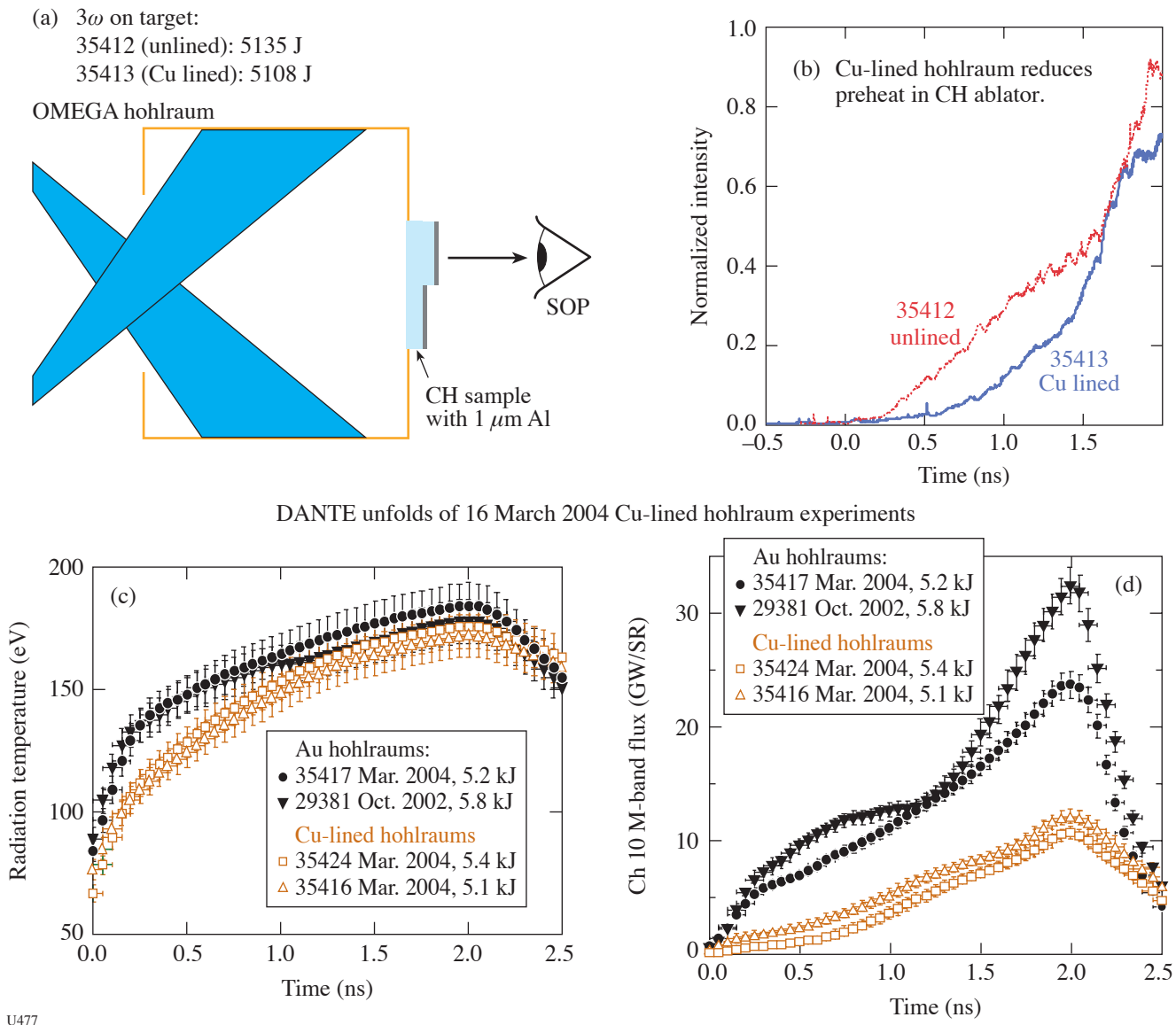
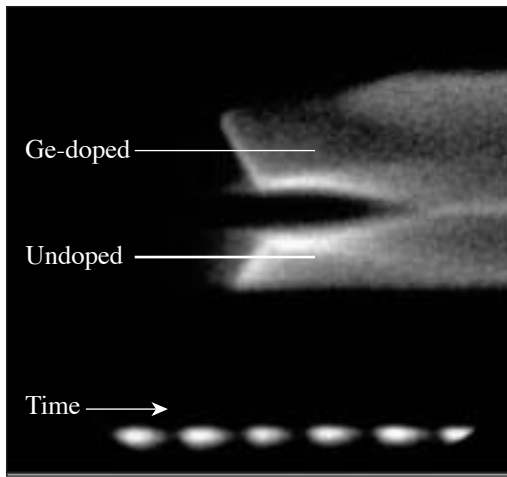
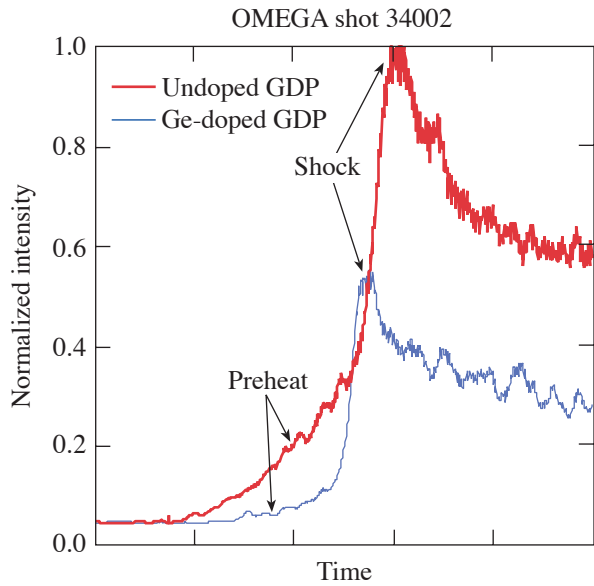


Figure 100.94
 Results from experiments to demonstrate the modification of a laser hohlraum spectrum by using a mid-Z wall liner (Cu).

hohlraum wall albedo measurement is shown in Fig. 100.97(b).

Tests of a VISAR Time-Resolved Hohlraum Temperature Measurement Technique: In FY04, we began tests on a new technique for time-resolved hohlraum temperature measurement. The basic idea is to use VISAR¹¹ to track the velocity of a radiatively driven shock front in a quartz sample attached to the wall of a hohlraum. The experimental arrangement for the initial tests at OMEGA is depicted in Fig. 100.98. These initial

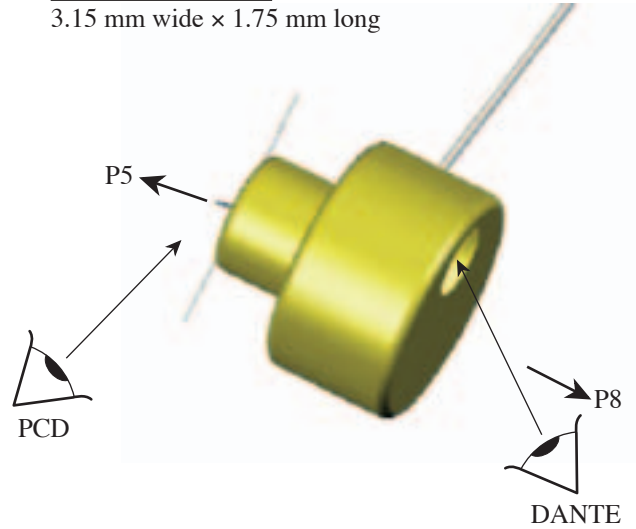
tests utilized both DANTE and an aluminum step witness plate to confirm the drive temperature and were performed for hohlraum temperatures in the range of 110 to 190 eV. As shown in Fig. 100.99, the VISAR-measured shock velocity can be used to track the hohlraum temperature history. For the hohlraum radiation temperature range of these experiments, the empirical conversion $T_r = 21.7 v_s^{0.57}$ has been used, where T_r is hohlraum temperature in eV and v_s is shock velocity in $\mu\text{m}/\text{ns}$. An important finding is that x-ray preheat presents a



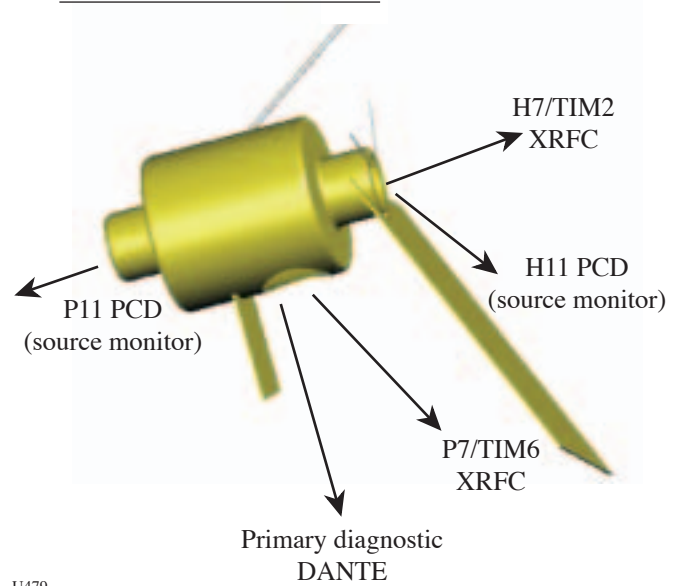
U478

Figure 100.95
Results from experiments to demonstrate the effectiveness of mid-Z dopants to reduce preheat.

(a) Secondary hohlraum
3.15 mm wide × 1.75 mm long



(b) Secondary with two primaries



U479

Figure 100.96
Schematic of long-pulse albedo experiments. (a) Secondary hohlraum driven with one primary hohlraum and (b) secondary hohlraum driven with two primary hohlraums.

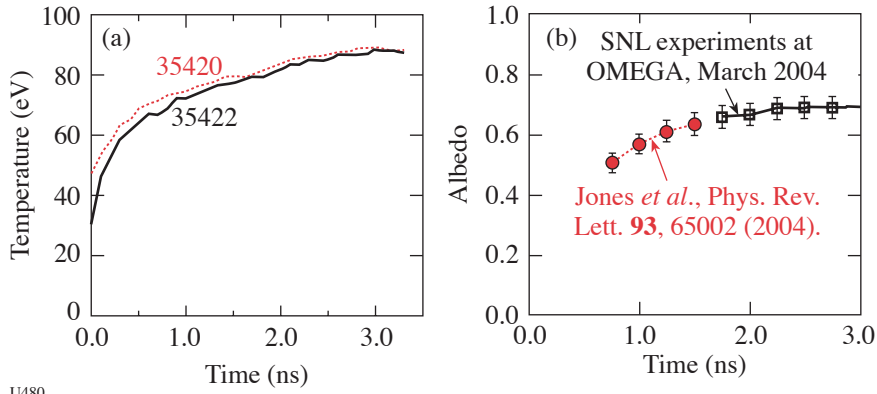
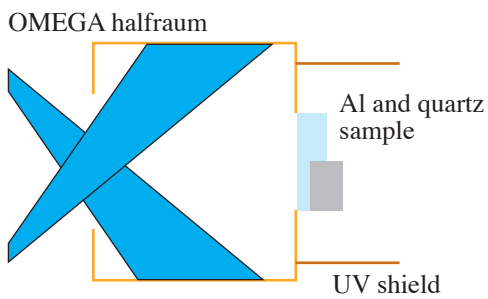


Figure 100.97
Temperature history of (a) secondary-hohlraum temperature and (b) albedo measurement.

U480



U481

Example VISAR data

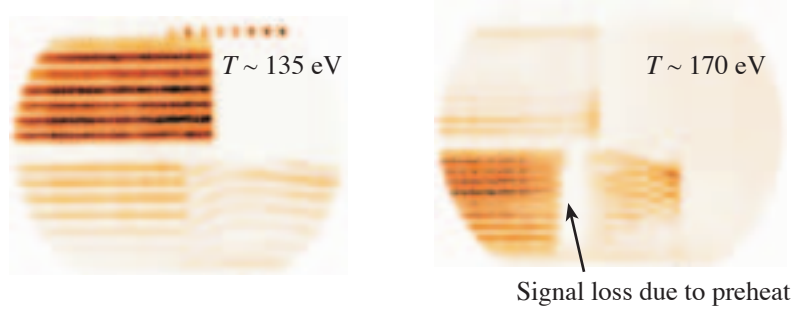
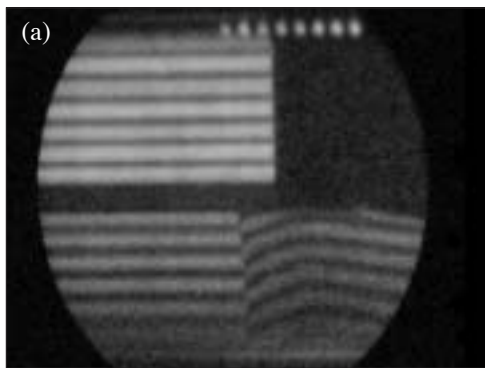


Figure 100.98
Experimental arrangement for SNL VISAR time-resolved hohlraum temperature measurement experiments.



U482

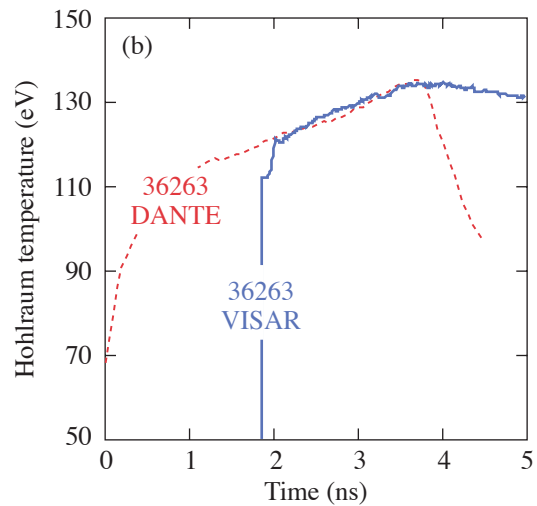


Figure 100.99
(a) VISAR velocity record and (b) resulting hohlraum temperature history from SNL experiment on OMEGA.

significant limitation to this technique for hohlraum temperatures above ~ 170 eV (as indicated in Fig. 100.98).

FY04 NRL Program Control of Laser Imprinting with High-Z Thin-Layer Targets

Principal Investigator: A. Mostovych

As part of a collaborative effort with NRL, a series of 13 OMEGA target shots were taken to investigate the control of laser imprinting.

The objectives of this experiment were to evaluate the impact of laser imprint under conditions similar to ICF-like reactor implosions and to test the effectiveness of controlling imprint from a high-power glass laser with the use of thin, high-Z-layer targets. In earlier work,¹² on the Nike KrF laser facility, it was demonstrated that thin, high-Z-layer targets are, in fact, very effective in mitigating imprint. It was not clear, however, if the differences between glass and KrF laser drivers, such as ASE, wavelength, or imprint details, are important and if the observed imprint mitigation had general validity irrespective of the laser driver.

In this work, the OMEGA laser was configured to drive a planar 30- μm CH target with multiple, full SSD beams. As is needed for high-gain target implosions, the target was accelerated on a low adiabat by compressing it with a single, low-intensity (10^{12} W/cm²), early beam foot (~ 2 ns) and subsequently accelerating it with three to five full-intensity beams ($\sim 5 \times 10^{13}$ W/cm²). The residual laser nonuniformities that imprint the target in the compression phase are amplified by RT growth in the acceleration phase and are measured in the experiment by x-ray radiography. An example of the measured RT amplified imprint is shown in Fig. 100.100. If the same target is now coated with a thin layer of high-Z material (250 Å of gold in this work), the foot pulse quickly ablates this layer and creates a region of strong laser absorption that moves with the ablating gold away from the target surface. At the point of absorption, the gold becomes a strong soft-x-ray radiator and drives target ablation farther from a standoff distance of several hundred microns. The separation of the absorption and ablation regions leads to a strong reduction in pressure non-uniformities on the target surface, thus mitigating the role of laser imprint. An example of this reduction is displayed in Fig. 100.101. Initial measurements of the Rayleigh–Taylor instability amplified imprint are displayed for targets with and without the thin gold layer. A clear reduction for the layered targets is observed. These results are in agreement with the initial Nike measurements but do not show as large of an effect.

This is expected because thinner gold layers had to be used to compensate for the shorter foot and thinner targets that could be deployed on the OMEGA facility. The initial results indicate that the control of imprint with high-Z-layer targets is a robust effect, not sensitive to the type of laser driver. It is expected that

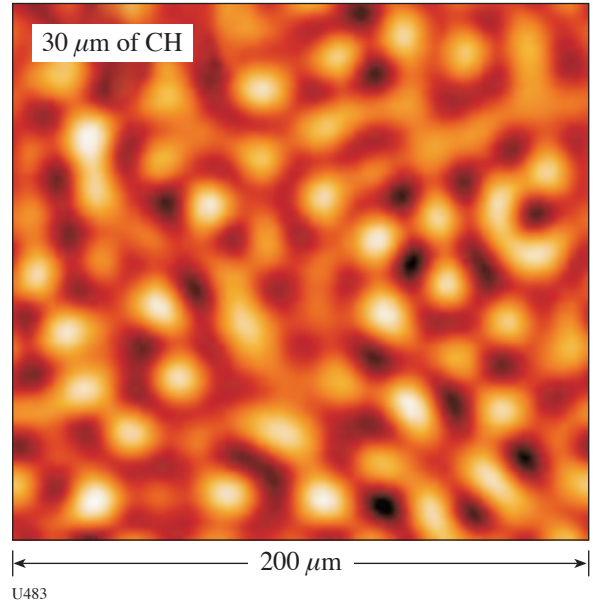


Figure 100.100 Typical mass nonuniformity of Rayleigh–Taylor amplified laser imprint at 3 ns into the main acceleration phase of a planar CH target.

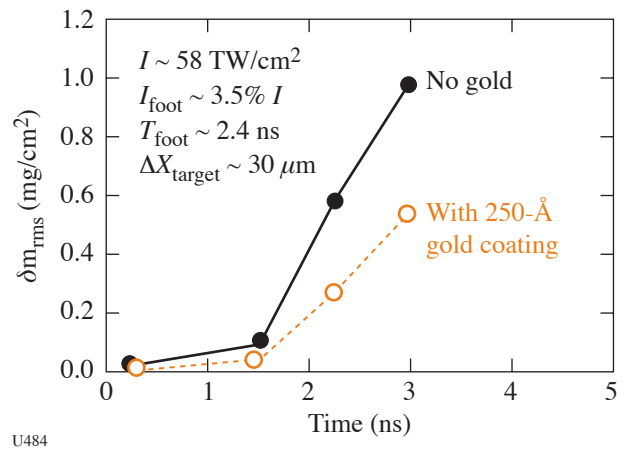


Figure 100.101 Comparison of amplified imprint with and without a thin gold coating on the ablation surface of the target. The thin, high-Z layer has a pronounced effect in reducing the level of imprint by almost 50%.

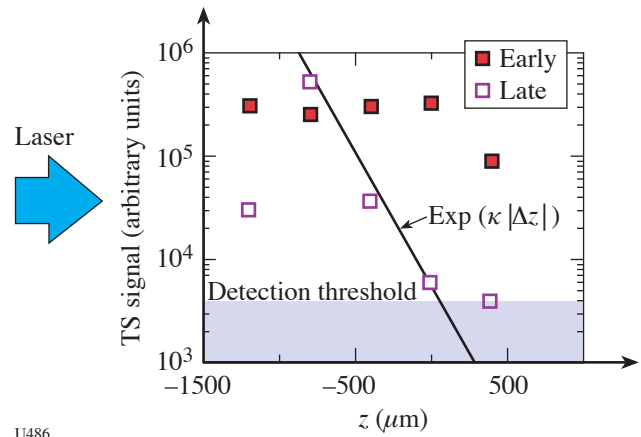
future near-term experiments will investigate the role of such high-Z layers in spherical implosions.

FY04 CEA Program

A total of 32 target shots led by CEA (Commissariat à l'Énergie Atomique, France) were carried out on OMEGA in FY04. The corresponding four experimental campaigns studied (a) laser-plasma interaction (LPI) in long-scale-length plasmas relevant to NIF/LMJ indirect-drive conditions; (b) irradiation symmetry and x-ray conversion efficiency in empty gold hohlraums; (c) production and optimization of multi-keV x-ray sources (performed on LLNL-owned shots); and (d) hydrodynamic instabilities in planar geometry. A summary of the LPI campaign is given in this section. The CEA diagnostics team also pursues a strong activity in the area of neutron detectors and neutron-induced effects on MJ-class laser detectors in collaboration with LLE teams. LLE direct-drive implosions provide a valuable neutron source for testing new concepts in this field.

The Thomson-scattering configuration for probing electron-plasma waves stimulated by the Raman backscattering instability (SRS) tested on OMEGA in FY03 was used in FY04 to study the SRS growth and saturation in gas-bag plasmas. As a first step, space-resolved measurements of SRS activity were

performed along the interaction-beam propagation axis (z). This is achieved by pointing the probe beam at different locations along the z axis (see Fig. 100.102). With a series of five shots, we have been able to assess the SRS growth along the z axis (see Fig. 100.103). These space-resolved measurements evidence a completely different spatial SRS growth depending on the time during the interaction pulse. At early time, when the heaters are on, the SRS activity is saturated with a constant level observed over more than 1 mm. Toward the end of the interaction pulse, the SRS activity peaks sharply near the input side of the interaction beam as expected from linear convective amplification theory.



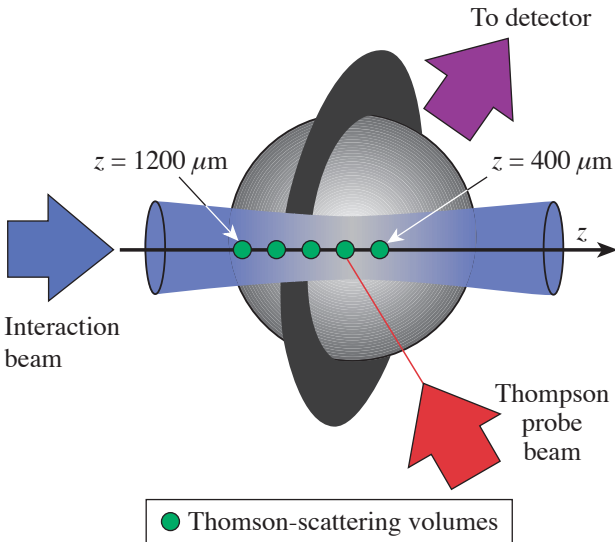
U486

Figure 100.103

Thomson-scattering signals as a function of z in the early ($t = 0.6$ to 1.1 ns, when the heaters are on) and late ($t = 1.2$ to 1.7 ns) time periods. The exponential fit of the late time measurements gives a spatial growth rate of $\kappa = 6 \times 10^{-3} \mu\text{m}^{-1}$.

REFERENCES

1. P. Loubeyre *et al.*, High Press. Res. **24**, 25 (2004).
2. J. R. Fincke *et al.*, Phys. Rev. Lett. **93**, 115003 (2004).
3. R. M. Baltrusaitis *et al.*, Phys. Fluids **8**, 2471 (1996).
4. D. Besnard, F. H. Harlow, and R. Rauenzahn, Los Alamos National Laboratory, Los Alamos, NM, Report LA-10911-MS (1987).
5. S. H. Batha and J. R. Fincke, "Quantified Reduction of Wall Material Influx During Hohlraum Experiments," to be published in the Review of Scientific Instruments.



U485

Figure 100.102

Schematic showing experimental configuration and the different probe-pointing locations of gas-bag targets.

6. R. E. Olson *et al.*, Phys. Rev. Lett. **91**, 235002 (2003).
7. H. N. Kornblum, R. L. Kauffman, and J. A. Smith, Rev. Sci. Instrum. **57**, 2179 (1986).
8. J. A. Oertel *et al.*, Rev. Sci. Instrum. **70**, 803 (1999).
9. R. E. Olson, R. J. Leeper, A. Nobile, J. A. Oertel, G. A. Chandler, K. Cochrane, S. C. Dropinski, S. Evans, S. W. Haan, J. L. Kaae, J. P. Knauer, K. Lash, L. P. Mix, A. Nikroo, G. A. Rochau, G. Rivera, C. Russell, D. Schroen, R. J. Sebring, D. L. Tanner, R. E. Turner, and R. J. Wallace, Phys. Plasmas **11**, 2778 (2003).
10. O. S. Jones *et al.*, Phys. Rev. Lett. **93**, 065002 (2004).
11. L. M. Barker and R. E. Hollenbach, J. Appl. Phys. **43**, 4669 (1972).
12. S. P. Obenschain *et al.*, Phys. Plasmas **9**, 2234 (2002).

Publications and Conference Presentations

Publications

- V. Bagnoud, I. A. Begishev, M. J. Guardalben, J. Keegan, J. Puth, L. J. Waxer, and J. D. Zuegel, "Optical Parametric Chirped-Pulse Amplifier as the Front End for the OMEGA EP Laser Chain," in *Inertial Fusion Sciences and Applications 2003*, edited by B. A. Hammel, D. D. Meyerhofer, J. Meyer-ter-Vehn, and H. Azechi (American Nuclear Society, La Grange Park, IL, 2004), pp. 670–673.
- T. R. Boehly, D. G. Hicks, P. M. Celliers, T. J. B. Collins, R. Earley, J. H. Eggert, D. Jacobs-Perkins, S. J. Moon, E. Vianello, D. D. Meyerhofer, and G. W. Collins, "Properties of Fluid Deuterium Under Double-Shock Compression to Several Mbar," *Phys. Plasmas* **11**, L49 (2004).
- T. J. B. Collins, S. Skupsky, V. N. Goncharov, R. Betti, P. W. McKenty, P. B. Radha, R. Epstein, A. Poludnenko, A. Frank, and S. Mitran, "High-Gain, Direct-Drive Foam Target Designs for the National Ignition Facility," in *Inertial Fusion Sciences and Applications 2003*, edited by B. A. Hammel, D. D. Meyerhofer, J. Meyer-ter-Vehn, and H. Azechi (American Nuclear Society, La Grange Park, IL, 2004), pp. 92–95.
- Q. Guo, X. Teng, and H. Yang, "Fabrication of Magnetic FePt Patterns from Langmuir–Blodgett Films of Platinum–Iron Oxide Core-Shell Nanoparticles," *Adv. Mater.* **16**, 1337 (2004).
- Q. Guo, X. Teng, and H. Yang, "Overpressure Contact Printing," *Nano Lett.* **4**, 1657 (2004).
- B. Hu and R. Betti, "Resistive Wall Mode in Collisionless Quasistationary Plasmas," *Phys. Rev. Lett.* **93**, 105002 (2004).
- T. J. Kessler, J. Bunkenburg, H. Huang, A. Kozlov, C. Kelly, and D. D. Meyerhofer, "The Coherent Addition of Gratings for Pulse Compression in High-Energy Laser Systems," in *Inertial Fusion Sciences and Applications 2003*, edited by B. A. Hammel, D. D. Meyerhofer, J. Meyer-ter-Vehn, and H. Azechi (American Nuclear Society, La Grange Park, IL, 2004), pp. 621–625.
- J. A. Koch, T. W. Barbee, Jr., S. Dalhed, S. Haan, N. Izumi, R. W. Lee, L. A. Welsch, R. C. Mancini, F. J. Marshall, T. C. Sangster, V. A. Smalyuk, J. M. Soures, and L. Klein, "Core Temperature and Density Profiles from Multispectral Imaging of ICF Plasmas," in *Inertial Fusion Sciences and Applications 2003*, edited by B. A. Hammel, D. D. Meyerhofer, J. Meyer-ter-Vehn, and H. Azechi (American Nuclear Society, La Grange Park, IL, 2004), pp. 857–861.
- J. Li, W. R. Donaldson, and T. Y. Hsiang, "Simulation of Submicrometer Metal–Semiconductor–Metal Ultraviolet Photodiodes on Gallium Nitride," *Solid-State Electron.* **48**, 2329 (2004).
- S. G. Lukishova, A. W. Schmid, C. M. Supranowitz, N. Lippa, A. J. McNamara, R. W. Boyd, and C. R. Stroud, Jr., "Dye-Doped Cholesteric-Liquid-Crystal Room-Temperature Single-Photon Source," *J. Mod. Opt.* **51**, 1535 (2004).
- R. L. McCrory (keynote speaker), "Progress in Inertial Confinement Fusion in the United States," in *Inertial Fusion Sciences and Applications 2003*, edited by B. A. Hammel, D. D. Meyerhofer, J. Meyer-ter-Vehn, and H. Azechi (American Nuclear Society, La Grange Park, IL, 2004), pp. 3–8.
- J. Myatt, A. V. Maximov, W. Seka, R. S. Craxton, and R. W. Short, "Modeling Stimulated Brillouin Scattering in the Underdense Corona of a Direct Drive Inertial Confinement Fusion Target," *Phys. Plasmas* **11**, 3394 (2004).
- J.-R. Park, W. R. Donaldson, R. Boni, and R. Sobolewski, "Characterization of Single and Double Fiber-Coupled Diffusing Spheres," *Appl. Opt.* **43**, 3967 (2004).

B. A. Remington, G. Bazan, J. Belak, E. Bringa, M. Caturla, J. D. Colvin, M. J. Edwards, S. G. Glendinning, D. S. Ivanov, B. Kad, D. H. Kalantar, M. Kumar, B. F. Lasinski, K. T. Lorenz, J. M. McNaney, D. D. Meyerhofer, M. A. Meyers, S. M. Pollaine, D. Rowley, M. Schneider, J. S. Stölken, J. S. Wark, S. V. Weber, W. G. Wolfer, B. Yaakobi, and L. V. Zhigilei, "Materials Science Under Extreme Conditions of Pressure and Strain Rate," *Metall. Trans. A, Phys. Metall. Mater. Sci.* **35A**, 2587 (2004).

S. Skupsky, R. Betti, T. J. B. Collins, V. N. Goncharov, J. A. Marozas, P. W. McKenty, P. B. Radha, T. R. Boehly, J. P. Knauer, F. J. Marshall, D. R. Harding, J. D. Kilkenny, D. D. Meyerhofer, T. C. Sangster, and R. L. McCrory, "Advanced Direct-Drive Target Designs for the NIF," in *Inertial Fusion Sciences and Applications 2003*, edited by B. A. Hammel, D. D. Meyerhofer, J. Meyer-ter-Vehn, and H. Azechi (American Nuclear Society, La Grange Park, IL, 2004), pp. 61–64.

Forthcoming Publications

V. Bagnoud, M. J. Guardalben, J. Puth, J. D. Zuegel, T. Mooney, and P. Dumas, "A High-Energy, High-Average-Power Laser Using Nd:YLF Laser Rods Corrected by Magnetorheological Finishing," to be published in *Applied Optics*.

A. C. A. Chen, S. Culligan, Y. Geng, S. H. Chen, K. P. Klubek, K. M. Vaeth, and C. W. Tang, "Glassy Nematic Conjugated Oligomers: Materials for Organic Light-Emitting Diodes," to be published in *Liquid Crystals VIII*.

S. H. Chen, "Multifunctional Glassy Liquid Crystals for Photonics," to be published in the *Journal of the Society for Information Displays*.

R. Epstein, "On the Bell–Plesset Effects: The Effects of Uniform Compression and Geometrical Convergence on the Classical Rayleigh–Taylor Instability," to be published in *Physics of Plasmas*.

S. Ghosh, R. Boni, and P. A. Jaanimagi, "Optical and X-Ray Streak Camera Gain Measurements," to be published in *Review of Scientific Instruments*.

V. Yu. Glebov, C. Stoeckl, T. C. Sangster, S. Roberts, and G. J. Schmid, "NIF Neutron Bang-Time Detector Prototype Test on OMEGA," to be published in *IEEE Transactions on Plasma Science*.

V. Yu. Glebov, C. Stoeckl, T. C. Sangster, S. Roberts, G. J. Schmid, R. A. Lerche, and M. J. Moran, "Prototypes of National Ignition Facility Neutron Time-of-Flight Detectors Tested on OMEGA," to be published in *Review of Scientific Instruments*.

V. N. Goncharov and G. Li, "Effect of Electric Fields on Electron Thermal Transport in Laser-Produced Plasmas," to be published in *Physics of Plasmas*.

O. V. Gotchev, P. A. Jaanimagi, J. P. Knauer, F. J. Marshall, and D. D. Meyerhofer, "KB-PJX—A Streaked Imager Based on a Versatile X-Ray Microscope Coupled to a High-Current Streak Tube," to be published in *Review of Scientific Instruments*.

D. R. Harding, F.-Y. Tsai, E. L. Alfonso, S. H. Chen, A. K. Knight, and T. N. Blanton, "Properties of Vapor-Deposited Polyimide Films," to be published in the *Journal of Adhesion Science and Technology* (invited).

J. P. Knauer and C. Gindele, "Temporal and Spectral Deconvolution of Data from Diamond, Photoconductive Devices," to be published in *Review of Scientific Instruments*.

J. A. Koch, T. W. Barbee, Jr., S. Dalhed, S. Haan, N. Izumi, R. W. Lee, L. A. Welser, R. C. Mancini, F. J. Marshall, D. D. Meyerhofer, T. C. Sangster, V. A. Smalyuk, J. M. Soures, L. Klein, and I. Golovkin, "Core Temperature and Density Gradients in ICF," to be published in the *Proceedings of the 14th APS Topical Conference on Atomic Processes in Plasmas*.

F. J. Marshall, J. A. Oertel, and P. J. Walsh, "A Framed, 16-Image Kirkpatrick–Baez Microscope for Laser–Plasma X-Ray Emission," to be published in *Review of Scientific Instruments*.

K. L. Marshall, E. Kimball, S. McNamara, T. Z. Kosci, A. Trajkovska-Petkoska, and S. D. Jacobs, "Electro-Optical Behavior of Polymer Cholesteric Liquid Crystal Flake/Fluid Suspensions in a Microencapsulation Matrix," to be published in *Liquid Crystals VIII*.

R. L. McCrory, "Recent Progress in Inertial Confinement Fusion in the United States," to be published in Nuclear Fusion.

A. V. Okishev and J. D. Zuegel, "Highly-Stable, All-Solid-State Nd:YLF Regenerative Amplifier," to be published in Applied Optics.

J.-R. Park, W. R. Donaldson, and R. Sobolewski, "Time-Resolved Imaging of a Spatially Modulated Laser Pulse," to be published in SPIE's Proceedings of LASE 2004.

S. P. Regan, J. A. Marozas, R. S. Craxton, J. H. Kelly, W. R. Donaldson, P. A. Jaanimagi, D. Jacobs-Perkins, R. L. Keck, T. J. Kessler, D. D. Meyerhofer, T. C. Sangster, W. Seka, V. A. Smalyuk, S. Skupsky, and J. D. Zuegel, "Performance of a 1-THz-Bandwidth, 2-D Smoothing by Spectral Dispersion and Polarization Smoothing of High-Power, Solid-State Laser Beams," to be published in the Journal of the Optical Society of America B.

R. Rey-de-Castro, D. Wang, X. Zheng, A. Verevkin, R. Sobolewski, M. Mikulics, R. Adam, P. Kordoš, and A. Mycielski, "Subpicosecond Faraday Effect in $Cd_{1-x}Mn_xTe$ and Its Application in Magneto-Optical Sampling," to be published in Applied Physics Letters.

R. W. Short and A. Simon, "Theory of Three-Wave Parametric Instabilities in Inhomogeneous Plasmas Revisited," to be published in Physics of Plasmas.

V. A. Smalyuk, V. N. Goncharov, T. R. Boehly, J. P. Knauer, D. D. Meyerhofer, and T. C. Sangster, "Self-Consistent Determination of Rayleigh–Taylor Growth Rates and Ablation-Front Density in Planar Targets Accelerated by Laser Light," to be published in Physics of Plasmas.

C. Stoeckl, W. Theobald, T. C. Sangster, M. H. Key, P. Patel, B. B. Zhang, R. Clarke, S. Karsch, and P. Norreys, "Operation of a Single-Photon-Counting X-Ray Charge-Coupled Device Camera Spectrometer in a Petawatt Environment," to be published in Review of Scientific Instruments.

A. Trajkovska-Petkoska, R. Varshneya, T. Z. Kosc, K. L. Marshall, and S. D. Jacobs, "Enhanced Electro-Optic Behavior for Shaped PCLC Flakes Made Soft by Lithography," to be published in Advanced Functional Materials.

L. Zheng, J. C. Lambropoulos, and A. W. Schmid, "UV-Laser-Induced Densification of Fused Silica: A Molecular Dynamics Study," to be published in the Journal of Non-Crystalline Solids.

Conference Presentations

The following presentations were made at SPIE's 49th Annual Meeting, Denver, CO, 2–6 August 2004:

S. D. Jacobs, "International Innovations in Optical Finishing."

K. L. Marshall, E. Kimball, S. McNamara, T. Z. Kosc, A. Trajkovska-Petkoska, and S. D. Jacobs, "Electro-Optical Behavior of Polymer Cholesteric Liquid Crystal Flake/Fluid Suspensions in a Microencapsulation Matrix."

The following presentations were made at the 7th International Conference on Tritium Science and Technology, Baden-Baden, Germany, 12–17 September 2004:

S. Costea, S. Pisana, N. P. Kherani, F. Gaspari, T. Kostas, W. T. Shmayda, and S. Zukotynski, "The Use of Tritium in the Study of Defects in Amorphous Silicon."

T. Kostas, N. P. Kherani, W. T. Shmayda, S. Costea, and S. Zukotynski, "Nuclear Batteries Using Tritium and Thin-Film Hydrogenated Amorphous Silicon."

W. T. Shmayda, "Metal Decontamination Using Low-Temperature Plasmas."

W. T. Shmayda and R. D. Gallagher, "Recovering Tritium from a Variety of Tritiated Waste Streams."

W. T. Shmayda, D. R. Harding, L. D. Lund, R. Janezic, and T. W. Duffy, "Handling Cryogenic DT Targets at the Laboratory for Laser Energetics."

W. T. Shmayda and N. P. Kherani, "Measuring Tritium Activity in Process Loops with Nude Baynard–Alpert Gauges."

P. A. Jaanimagi, R. Boni, D. Butler, S. Ghosh, W. R. Donaldson, and R. L. Keck, "The Streak Camera Development at LLE," 26th International Congress on High-Speed Photography and Photonics, Alexandria, VA, 20–24 September 2004.

The following presentations were made at the Boulder Damage Symposium XXXVI, Boulder, CO, 20–22 September 2004:

S. Papernov and A. W. Schmid, "High-Spatial Resolution Studies of UV-Laser Damage Morphology in SiO₂ Thin Films with Artificial Defects."

A. L. Rigatti, "Cleaning Process Versus Laser Damage Threshold of Coated Optical Components."

UNIVERSITY OF
ROCHESTER